1994AJ....108..766B

THE ASTRONOMICAL JOURNAL VOLUME 108, NUMBER 3 SEPTEMBER 1994

DEEP VLA IMAGING OF TWELVE EXTENDED 3CR QUASARS

ALAN H. BRIDLE

National Radio Astronomy Observatory,[1] Charlottesville, Virginia 22903
Electronic mail: abridle@nrao.edu

DAVID H. HOUGH

Trinity University, San Antonio, Texas and Jet Propulsion Laboratory, California Institute of Technology, Pasadena, California 78212
Electronic mail: dhough@physics.trinity.edu

COLIN J. LONSDALE

Haystack Observatory, Westford, Massachusetts 01886
Electronic mail: cjl@wells.haystack.edu

JACK O. BURNS

Department of Astronomy, New Mexico State University, Las Cruces, New Mexico 88003
Electronic mail: jburns@nmsu.edu

ROBERT A. LAING

Royal Greenwich Observatory, Cambridge, United Kingdom
Electronic mail: rl@mail.ast.cam.ac.uk

Received 1994 January 11; revised 1994 April 18

ABSTRACT

A representative sample of 12 extended quasars from the 3CR catalog has been imaged at 4.9 GHz using the VLA. These full synthesis observations typically achieve an rms noise of 20 μJy per beam, at a resolution (FWHM) of $0\farcs34$ to $0\farcs38$. Jets are detected on at least one side of every source. The jets are well collimated compared with those in less powerful sources, but spreading is detected in most of them. The opening angles of several jets are not constant, but show recollimation after an initial regime of rapid spreading. Many of the jets contain quasiperiodic strings of knots, of which the knot closest to the central feature is usually the brightest (until the jet nears its hot spot). The degrees of linear polarization at the jet knots range from $<5\%$ to $\sim50\%$, but show no common trend with distance along the jets. In knots that are elongated in directions close to that of the jet, the **E** vectors tend to be orthogonal to the jet axis. The exceptions—misaligned knots with misaligned polarizations—tend to be bright features near large bends in the jets. Many of the jets are initially straight to within a few degrees, but bend more in the outer part of the source. The prominence of the *inner, straighter* jet segments relative to the extended lobes correlates significantly with the prominence of the milliarcsecond-scale central features, but the prominence of the more bent jet segments does not. Candidates for counterjet emission are detected in seven sources, but there is no unambiguous, continuous counterjet in any of them. Estimates of the flux density ratios between the straighter jet segments and the counterjets based on these tentative detections range from 1.2:1 to >175:1. There is no evidence in this sample that counterjet detectability correlates with such putative inclination indicators as central feature prominence or projected linear size. There is also no evidence that the prominence of the counterjets anticorrelates with that of the jets as predicted by simple relativistic-beaming models for the jet/counterjet asymmetry. There is, however, strong evidence that large bends in the main jet favor counterjet detection, and there are no counterjet candidates opposite *long, uninterrupted* straight segments of the main jets. The detectability of the counterjets in these quasars may therefore be strongly influenced by interactions between the underlying beams and inhomogeneities in the surrounding material. We offer a new empirical definition of the term "hot spot" that is intended to improve the distinction between such features and "jet knots." Both the compactness of hot spots and their position in the lobe are affected by whether they are fed by a detectable jet. When the hot spots differ significantly in compactness, the more compact one is always on the jetted side. Jetted hot spots are also more likely to be recessed deeply from the outer edge of their lobes than are their counterjetted counterparts. The jetted hot spot is less prominent relative to other extended emission if the jet bends through a large angle, particularly if a large bend occurs abruptly. The counterjetted hot spot is also less well defined if the jet is more bent. The lobes of several sources show considerable inhomogeneity, including filamentation. There is little difference in the inhomogeneity of the jetted and counterjetted lobes if the hot spots are excluded. The lobes have a common

---

[1] The NRAO is operated by Associated Universities, Inc., under cooperative agreement with the National Science Foundation.

0004-6256/94/108(3)/766/55/$0.90

linear polarization pattern, with low polarization at the center and high polarization (often reaching 40% to 60%) near the edges. This pattern matches the expectations of models in which the magnetic field in the lobes is provided by passively expanding the field in the jets. The lobes in sources with promising counterjet candidates are often S-symmetric relative to the jet axis and their hot spots are more misaligned than in sources without such candidates. Counterjets may therefore be easier to detect if the jets change orientation during the lifetime of the source. We outline the implications of our results for various models of the prominence and asymmetries of central features, jets, counterjets, and hot spots. The correlations between the prominence and sidedness of the large-scale straight jet segments and of the small-scale central features favor models in which the kiloparsec-scale jets initially have bulk relativistic velocities. The slope of the prominence correlation is less than expected if the larger-scale jets have characteristic Lorentz factors as high as those in the milliarcsecond-scale features, however. This result is fragile within our small sample, but other aspects of our data also suggest that another phenomenon, closely coupled to jet bending, helps to determine the prominence of features far from the central region. Overall, our data favor "tired jet" models in which the *average* jet velocity decreases with increasing distance from the central object. This makes it harder for the simplest relativistic-jet models to account for the systematic differences in compactness and placement of jetted and counterjetted hot spots. The models may need refinement to include a range of Lorentz factors in the jets at any given distance from the quasar.

1. INTRODUCTION

Although many extended extragalactic radio sources with powers $>10^{25}$ W Hz^{-1} at 1.4 GHz have two-sided large-scale structures (the "classical double" morphology), the radio jets in these sources are overwhelmingly one-sided (e.g., Bridle 1984). It is important to understand why the jets apparently break the brightness symmetry of the lobes so strongly in the powerful extended sources.

There are at least three interpretations of the apparent one-sidedness of the jets in the powerful sources. These correspond to three (not necessarily mutually exclusive) views of the energy transport processes:

(1) *There is a beam on the dark side* that is intrinsically identical to the beam on the bright side, *but its synchrotron emission is directed away from us by bulk relativistic motion.* On this view, the "one-sidedness" of the jets in powerful sources implies that the beam velocities remain at least mildly relativistic to kiloparsec scales. This is a simple extrapolation to larger scales of the popular models for one-sidedness and superluminal motion in parsec-scale jets (e.g., Rees 1978; Blandford & Königl 1979; Scheuer & Readhead 1979).

(2) *There is an active beam on the dark side but its synchrotron emissivity is low*, i.e., the energy pipeline is more efficient on the dark side than on the bright side. On this view, the two beams may transport the same power, but the beam on the dark side may (for example) interact less with surrounding gas, or may contain fewer relativistic electrons or a different magnetic field strength and configuration, than the other. On this view, the brightness asymmetries of jets in powerful sources may be induced by asymmetries in the environments of the beams or in their content of relativistic particles and fields.

(3) *Much less is happening on the apparently unjetted side.* On this view, the brightness asymmetry of the synchrotron emission from the jets results from a real asymmetry in the rate of energy transport by the beams on the two sides of the central engine. The engine intrinsically supplies less power, or even no power, to the "dark side." The engine must therefore reverse its preference ("flip-flop") occasionally to form sources with two similar lobes (Rudnick 1982; Icke 1983; Rudnick & Edgar 1984). On this view, the opposing beams would be neither identical nor steady in time.

We select these three possibilities for discussion not because they are either fully comprehensive or exclusive, but because they provide three convenient model extremes with which to compare our data. Many arguments for or against each of these interpretations of one-sidedness in quasar jets are inconclusive because the counterjets are usually undetected and we cannot *quantify* the one-sidedness. We therefore tried (a) to find evidence of counterjet emission, (b) to quantify the jet detection rate and prominence statistics, and (c) to explore any systematic differences between the morphologies of lobes on the jetted and counterjetted sides, in a sample of extended 3CR quasars. We used the VLA at 4.9 GHz to make sensitive, high-resolution observations of a representative sample of twelve such sources.

Section 2 of this paper describes how we selected the sample, and Sec. 3 details our observing strategy, calibration and data reduction. Section 4 presents the new images and introduces terminology that we use to interpret and quantify their main features. Section 5 derives physical parameters for the sources and explores correlations among them. Section 6 discusses and summarizes our main empirical results.

The rest of the paper discusses how our results affect models of energy transport in quasar radio sources. Section 7 reviews their implications for the three classes of model outlined above. Section 8 summarizes our conclusions and suggests further work.

2. THE SAMPLE

We selected a sample of radio quasars by the strength and angular extent of their extended (lobe) radio emission. Our initial sample was the 19 strongest quasars with largest angular sizes >10″ in the revised 3CR catalog (Laing *et al.* 1983). We chose the angular size limit so that details of the source structures would be readily resolved by the ~0″.35

TABLE 1. Basic properties of the observed quasars.

IAU NAME	3C NAME	z^a	$m_V{}^a$	$S_5{}^b$ (mJy)	LAS^c (″)	LLS^d (h^{-1} kpc)	Refs to other radio data
0017+154	3C 9	2.012	18.21	490	14	57	1-5
0133+207	3C 47	0.425	18.1v	1390	79	262	3,4,6-11
0229+341	3C 68.1	1.238	19	780	53	228	2,8,12-14
0710+118	3C175	0.768	16.6v	690	52	212	3,12,14
0833+654	3C204	1.112	18.21	370	37	159	2-4,9,15-19
0850+140	3C208	1.11	17.4v	560	14	60	2,3,9,12,16,20,21
0903+169	3C215	0.411	18.3v	427	60	196	3,4,8,22,23
1100+772	3C249.1	0.311	15.7v	800	53	149	3,4,8,9,14-16,24-27
1137+660	3C263	0.646	16.3v	1130	51	198	3,4,8,14,17,26,28-31
1618+177	3C334	0.555	16.4v	626	58	215	3,8,12,14,15,22,26,29,32,33
1622+238	3C336	0.927	17.5v	830	28	118	3,4,8,34
1704+608	3C351	0.371	15.3v	1260	75	230	2,3,8,14,35,36
2120+168	3C432	1.805	17.96	407	15	63	3,12,13,34,37

Notes to TABLE 1

(a) Redshifts and visual magnitudes from Hewitt & Burbidge (1987); "v" connotes a known variable.
(b) Integrated 5 GHz flux density (mJy) in 1986/87 on Baars *et al.* (1977) scale; from our VLA data or Gregory & Condon (1991), whichever is larger.
(c) Largest angular size in arc seconds.
(d) Projected largest linear size in h^{-1} kpc (using a Friedmann cosmology with $H_0=100h$ km s^{-1} Mpc^{-1}, $q_0=0.5$).

References to TABLE 1

(1) Kronberg, P. P., in Bridle & Perley (1984)
(2) Laing (1981)
(3) Miley & Hartsuijker (1978)
(4) Pooley & Henbest (1974)
(5) Swarup *et al.* (1982)
(6) Fernini *et al.* (1991)
(7) Vermeulen *et al.* (1993)
(8) Swarup *et al.* (1984)
(9) Burns *et al.* (1984)
(10) Bentley *et al.* (1975)
(11) Burch (1979)
(12) Jenkins *et al.* (1977)
(13) Wardle, J. F. C., in Cawthorne *et al.* (1986)
(14) Leahy *et al.* (1989)
(15) Hine & Scheuer (1980)
(16) Laing, R. A., in Bridle & Perley (1984)
(17) Owen *et al.* (1978)
(18) Owen & Puschell (1984)
(19) Hough *et al.* (1993)
(20) Cawthorne *et al.* (1986)
(21) Menon (1976)
(22) Hintzen *et al.* (1983)
(23) Wardle, J. F. C., Potash, R. I. & Roberts, D. H., private communication
(24) Laing, R. A., private communication
(25) Lonsdale & Morison (1983)
(26) Wardle, J. F. C., private communication
(27) Hough (1986)
(28) Browne, I. W. A., private communication
(29) Schilizzi *et al.* (1982)
(30) Shone *et al.*, in Browne (1987)
(31) Zensus *et al.* (1987)
(32) Wardle & Potash (1982)
(33) Hough *et al.* (1992)
(34) Feigelson *et al.* (1984)
(35) Riley & Pooley (1975)
(36) Kronberg *et al.* (1980)
(37) Swarup *et al.* (1986)

(FWHM) synthesized beam of the VLA's A configuration at 4.9 GHz. We concentrated on quasars because jets are detected more readily in quasars than in radio galaxies (Bridle & Perley 1984). This maximized our chance to acquire useful information about the jets, or about systematic differences between jetted and counterjetted lobes, if no counterjets were found. If counterjets were detected, new constraints could be placed on the alternative models for the one-sided appearance of most quasar jets. Because this sample is composed of quasars, it may, however, be biased toward sources that are oriented toward the line of sight if the optical classification depends on orientation (e.g., Barthel 1989). Our concentration on sources of large angular size should partly compensate this possible bias toward end-on sources, but a parallel VLA study of extended radio galaxies whose radio powers are similar to these quasars has also been undertaken (Fernini *et al.* 1993).

To obtain both high sensitivity and dense coverage of the u,v plane, the observations were made as continuous syntheses. The sample size therefore had to be restricted to conform to the available observing time, so we selected a subsample of 12 sources from the initial 19 by considering how the sources fitted together into the scheduled 24 h observing periods. The final subsample was thereby chosen for mutual compatibility in right ascension and declination rather than by any intrinsic radio property. In particular, we did not select for or against prominence of the central features, any particular source morphology, or by whether a jet had previously been detected.

Table 1 lists basic properties of the 12 sources that we observed, and of 3C47, for which we obtained a deep VLA synthesis at 4.9 GHz from Fernini *et al.* (1991). This sample of 13 sources includes all 10 3CR quasars whose largest projected linear sizes exceed $100h^{-1}$ kpc ($H_0=100h$ km s^{-1} Mpc^{-1}, q_0=0.5) at radio wavelengths.

3. THE OBSERVATIONS AND REDUCTIONS

3.1 Strategy

The sources were observed for as long as possible in single observing sessions with the VLA's A and B configurations. The detailed hour angle coverages and integration

TABLE 2. VLA observing log.

Source Name	A Config Date	A integ time (min)	B Config Date	B integ time (min)	Calib Source	HA min (h)	HA max (h)
3C 9	5-May-86	450	19-Jul-86	61	3C 84	-4.1	4.1
3C 68.1	29-Mar-86	327	19-Jul-86	269	3C 84	-4.4	1.6
3C175	29-Mar-86	436	19-Jul-86	187	3C 84	-3.0	4.6
3C204	4-May-86	403	19-Jul-86	226	3C 84	-4.4	2.9
3C208	12-Jul-87	448	6-Dec-87	70	3C 84	-5.2	2.8
3C215	11-Jul-87	431	6-Dec-87	289	3C 84	-5.1	2.0
3C249.1	11-Jul-87	419	6-Dec-87	265	3C 84	-14.4	-7.1
3C263	11-Jul-87	390	6-Dec-87	238	3C345	1.5	7.8
3C334	5-May-86	442	19-Jul-86	183	3C345	-4.0	3.8
3C336	11-Jul-87	403	6-Dec-87	228	3C345	-3.7	4.0
3C351	29-Mar-86	478	19-Jul-86	260	3C345	-2.8	4.7
3C432	12-Jul-87	390	6-Dec-87	152	3C 84	-1.9	6.1

times were dictated by the need for mutual scheduling, generally restricting the observations to elevation angles above 20°. (The one exception was 3C432, which was observed down to an elevation of 10°; for this source, the low-elevation data were calibrated separately using a model derived from the high-elevation data). Table 2 gives the observing log. To maximize sensitivity, the observations were made with 50 MHz bandwidth in two frequency channels, centered on 4.835 and 4.885 GHz. The visibilities were averaged for 20 s. This averaging time is a compromise between a short integration to let self-calibration track tropospheric phase fluctuations and a long integration to restrict the sizes of the data sets. The antenna delay settings were checked before each observing run and were reset if any offsets significantly exceeded 0.8 ns.

3.2 *Calibration*

All sources contained enough flux density in compact structure (central features, hot spots, or both) to allow self-calibration. Our observing strategy therefore emphasized (a) determining baseline-based errors and (b) minimizing gaps in the hour-angle coverage. The primary amplitude and phase calibration was interpolated from observations made every 2 h of one of the strong sources 3C84 and 3C345, and no secondary calibrators near the target sources were observed. In poor weather, this two-hour phase calibration cycle sometimes led to ambiguities in the phase wrap on the longer baselines in the A configuration. These ambiguities were resolved by restricting the initial antenna phase calibration to baselines in the inner third of the u,v plane.

The assumed mean positions of the unresolved structure of 3C84 and 3C345 (Table 3) provide our primary position calibration. The uncertainties in the external phase calibration are such that errors in the positions of individual features on our images relative to these mean positions for 3C84 and 3C345 should be no worse than 0″.2.

The flux densities of 3C84 and 3C345 were referenced to that of 3C286 during each observing run, assuming that 3C286 has flux densities of 7.31 and 7.26 Jy at 4.835 and 4.885 GHz, respectively. The calibration of the amplitude scale of the images relative to these assumed values for 3C286 should always be accurate to $\leqslant 1\%$.

TABLE 3. Reference frame for radio position calibration.

Source	Position (B1950.0)		Used to Calibrate
	h m s	° ′ ″	
3C 84	03 16 29.569	41 19 51.94	3C9, 3C68.1, 3C175, 3C204 3C208, 3C215, 3C249.1, 3C432
3C345	16 41 17.608	39 54 10.82	3C263, 3C334, 3C336, 3C351

The polarization position angle scales were calibrated using observations of 3C286, assuming that its **E** vector position angle is 33°. The accuracy of these calibrations is $\leqslant 2°$. The on-axis instrumental polarization properties were determined from the observations of 3C84; the individual antenna polarization corrections are generally accurate to better than 0.1% and 3°.

The NRAO's AIPS software was used for all imaging and secondary (self) calibration. Preliminary images based on the primary (external) calibration were used to determine the positions of the brightest compact features in each source. These were usually the central features and/or the peaks of hot spots. The positions of these features were preserved throughout later self-calibration cycles using the Schwab (1980) algorithm. CLEAN component models were fed back to the self-calibration procedure to refine the phase calibration and to adjust the relative amplitude calibration of the antennas (without changing the mean amplitude scale). The B configuration data were aligned in phase with the A configuration data by referencing them in the outer u,v range to a well calibrated A configuration CLEAN component model. After this cross-calibration, the final high-resolution images were produced from the combined (A plus B configuration) data, sometimes with further iterations of self-calibration.

For some sources, this procedure converged but failed to produce images whose off-source fluctuations were within about 50% of those expected from the thermal noise. When this occurred, we applied further baseline-based amplitude and phase corrections derived from our observations of 3C84. These baseline-based corrections noticeably improved most images to which they were applied, but the principal limitations on dynamic range (unremovable sidelobe responses to the strongest compact features) remained in some images. The remaining imperfections in the deconvolved images therefore cannot be attributed either to antenna-based time-dependent calibration errors or to time-independent baseline-based calibration errors. Their origin is uncertain, but many deep high-resolution images of bright extended radio structures made using the VLA and the standard AIPS software encounter such limits. They may result from averaging the phase drifts of bright features (hot spots) far from the delay tracking center during self-calibration.

3.3 *Imaging*

The data were initially imaged over the whole VLA primary beam at low resolution to locate possible confusing sources or unexpected large scale structure. Most of the sources were then imaged at high resolution over at least four times the area of sky containing significant emission, so that the images could be deconvolved with an efficient FFT-based CLEAN algorithm (Clark 1980—the AIPS task APCLN). If low-resolution imaging showed significant confusion within the primary beam, the high-resolution images were constructed in several pieces using the more CPU-intensive Cotton–Schwab ungridded-subtraction CLEAN algorithm

TABLE 4. VLA image catalog.

	<---- A+B configuration			---->	<---- B configuration			---->
Source	FWHM (")	r.m.s. noise (μJy)	Peak to r.m.s. (I)	Figs.	FWHM (")	r.m.s. noise (μJy)	Peak to r.m.s. (I)	Figs.
3C 9	0.36	20	4300	1,2	1.30	52	3600	
3C 68.1	0.35	21	5900	5,6	1.10	41	7600	3,4
3C175	0.38	17	3800	8,9	1.30	38	3800	7
3C204	0.34	22	1900	10,11	1.10	61	1190	
3C208	0.37	25	5900	12,13	1.17	61	4600	
3C215	0.37	16	1050	16,17	1.20	27	600	14,15
3C249.1	0.35	21	3400	20,21	1.10	32	3000	18,19
3C263	0.36	25	13900	22,23	1.00	57	9500	
3C334	0.35	17	7650	25,26	1.15	36	3800	24
3C336	0.34	18.5	2700	27,28	1.25	38	5400	
3C351	0.37	22	7200	32,33	1.15	46	6900	30,31
3C432	0.37	19	3850	34,35	1.20	41	3100	

(Schwab 1984—the AIPS task MX). The reality of faint features was checked by also making Maximum Entropy Method (MEM) deconvolutions, using the method of Cornwell & Evans (1985—the AIPS tasks VM and VTESS). For some sources, the optimal processing proved to be CLEANing of the most intense compact structure followed by MEM deconvolution of the extended emission. Except where otherwise noted, however, we made all quantitative measurements from the CLEANed images. The deconvolved CLEAN component models were restored with circular Gaussian convolving beams and were superposed on the residuals from the CLEAN component subtraction. The widths of the restoring beams are the mean of the major and minor axes of the best Gaussian fit to the central peak of the "dirty" synthesized beam derived with uniform weighting of the u,v data. For most images, the corrections to the beam dimensions in this circularization step were $<5\%$; the worst cases are $\sim 10\%$.

For a few sources, some bright substructures that are important to interpreting the radio morphologies are poorly resolved by conventional image processing. For these we used the MEM deconvolution to extract morphological information on scales smaller than the conventional synthesized beamwidth (e.g., Cornwell & Evans 1985).

4. THE IMAGES

Table 4 summarizes the main parameters of the images presented below. In the accompanying figures, the total-intensity contour maps are of the images made in Stokes I. The vector displays show vectors whose lengths are proportional to the degree of linear polarization $p = \sqrt{Q^2+U^2}/I$ and whose position angles are those of the **E** vectors, superposed on selected contours from the Stokes I images. The polarized intensities P were adjusted for the Ricean bias (e.g., Vinokur 1965; Wardle & Kronberg 1974) using the approximate corrections in the AIPS task COMB (see Leahy & Fernini 1989). The resolution quoted for each image is the FWHM of the Gaussian restoring beam.

FITS tapes of the image data are available from Alan H. Bridle at the National Radio Astronomy Observatory.

4.1 Terminology

The terms "central feature," "jet," "lobe," and "hot spot" are used below in ways that require careful definition.

A "central feature" is an unresolved feature coinciding to within observational errors with the best available position for the optical quasar. Although such features are frequently referred to as "cores," we consider this term to be prejudicial for several reasons. It is poorly defined, resolution-dependent, and is a relic of a physical model in which these features were considered to coincide with the "central engines" of the sources, rather than with the opaque base of a jet.

A "jet" is a narrow feature that meets the criteria used by Bridle (1986), i.e., it is (a) at least four times as long as it is wide (after deconvolving the synthesized beam), (b) separable at high resolution from other extended structure (if any) either spatially or by brightness contrast, and (c) aligned with the nucleus of the parent object where it is closest to it. Many jets contain internal, local, brightness enhancements that we generically describe as "jet knots."

The "lobes" consist of all the other radio emission produced by the source. Many lobes in powerful radio sources have local brightness enhancements that are conventionally called, "hot spots," but there is no well accepted definition of this term (Perley 1989; Laing 1989). We use a new empirical definition of the term "hot spot" to distinguish a limited subset of such features from all other brightness enhancements in jets and lobes. We are attempting thereby to isolate a class of feature that marks major changes in the apparent direction and/or collimation of a jet, or its abrupt termination. Our prime, but not our only, concern is to distinguish hot spots from the jet knots that may be only minor disturbances within an ongoing, continuous jet.

Our empirical definition of a hot spot is therefore as follows. If no jet is detected, then the hot spot must: (a) be the brightest feature in the lobe, (b) have a surface brightness that is more than four times greater than that of the surrounding emission and (c) have a linear FWHM (after deconvolving the synthesized beam) that is $<5\%$ of the largest diameter of the source. If a jet is detected then we add a further condition: (d) the hot spot must be further from the nucleus than the end of the jet, which is defined by (d1) its disappearance, (d2) an abrupt change of direction (i.e., by at least 30° within a knot diameter), or (d3) decollimation by more than a factor of two (as measured by the widths of any ridge-like or knot-like features along the putative path of any continuing flow).

Condition (d) is intended to separate hot spots from jet knots. No emission "downstream" of a feature with these properties will be described as a jet, although it is likely that such emission could contain ongoing flows.

We are trying to distinguish between features in which different physical processes may dominate. Both jet knots and hot spots are likely to be regions of shock-driven compression and/or particle acceleration in a flow, so they may share many observable characteristics. Definitions that depend only on surface brightness and angular or linear size, independent of relationships with surrounding structure, often cannot separate jet knots and hot spots. Our added ingredient of continuity of jet properties through a feature may help to distinguish cases where shocks in a jet are highly oblique, so that the flow remains supersonic beyond them, from major disruptions at nearly perpendicular shocks. The former, if present in radio sources, would be classified as jet knots; the latter would be classified as hot spots.

Note that by our definition there can be only one hot spot per lobe. The features often described in the literature as "secondary hot spots" will here be regarded as fine structure in the lobes, but will not be referred to as hot spots.

We acknowledge that the results of applying the above criteria for jets, jet knots, and hot spots may depend on angular resolution, at least until all but a few features of a radio source are fully resolved. In particular, the criterion that a hot spot should have a FWHM$<$5% of the largest angular diameter may be insufficiently stringent. We believe, however, that these criteria form a useful basis for classifying features of quasar images at the relative resolution achieved in these observations.

4.2 3C9

Figure 1 shows the total intensity image at 0″.36 resolution from the combined A and B configuration data. This small (14″, $57h^{-1}$ kpc) source has the highest red shift in the sample [normally given as z=2.012 but see also Tytler & Fan (1992) for a revised estimate of 2.0178]. Kronberg *et al.* (1991) suggested that the source is gravitationally imaged by a galaxy about 10″ away, but this suggestion has yet to be confirmed by optical data (see also Yee *et al.* 1993).

The compact feature D coincides with the optical identification. The jet is exceptionally knotty and its terminus in the southeast lobe is ill defined. Feature K meets our criteria for the hot spot because of its brightness contrast and the abrupt change in direction of the ridge line in its vicinity. The jet therefore consists of features E through J. It is relatively straight in PA 150° until the bright feature F 2″.8 from the central feature. F is the most compact feature south of the central feature, as determined both by model-fitting to Fig. 1 and from an MEM deconvolution at 0″.12 resolution (not shown). Feature F marks a significant change in the character of the jet, which brightens just before it. The average position angle of the jet between F and I is also conspicuously different from that before F, but we do not resolve the structure well enough to be sure where this realignment starts.

There is weak emission between the compact central feature D and the brightest part of the northwest lobe, with local peaks at C and B. These features could be part of a counterjet leading into this lobe. A curved ridge extends northwest from B and crosses the lobe before reaching the hot spot A. Some or all of this curved ridge may also be part of a bent counterjet with a further peak near the first bend between B and A. The source has an overall S symmetry, but the jetted arm is about twice as long as the counterjetted arm in projection.

Figure 2 shows the polarization data also at 0″.36 resolution, superposed on contours from Fig. 1. The vector distribution is locally confused, especially in the inner 4″ ($16h^{-1}$ kpc) on the jetted side. Beyond 4″, the **E** vectors tend to be perpendicular to the local jet axis, and to the outer edges of the lobes. The strong discontinuity in the **E**-vector directions near feature F further suggests that this feature marks a point where either the jet or the surrounding medium, or both, change character substantially. The trend for the **E** vectors to be perpendicular to the jet axis and to the lobe edges further from the central feature casts doubt on the likelihood that the major deflections of the jet result from gravitational imaging, as such imaging would not preserve these relationships (Kronberg *et al.* 1991). The degree of polarization in the jet reaches $\sim$30% near knot G. The degree of polarization in the

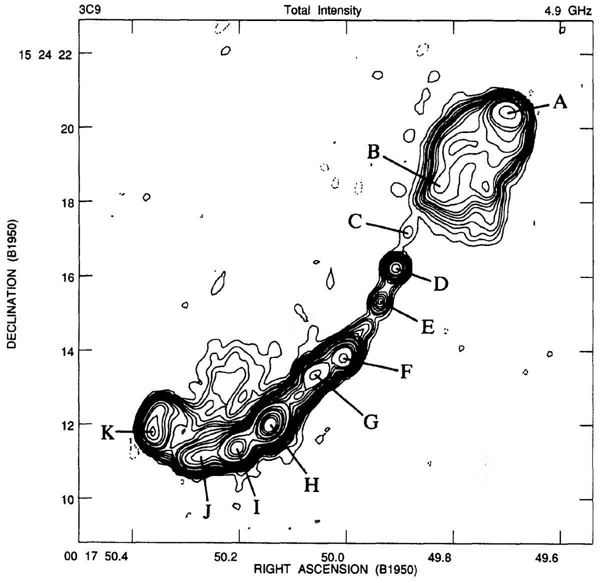

FIG. 1. Distribution of total intensity (Stokes I) over 3C 9 with 0″.36 (FWHM) resolution. D is the central feature and K is the jetted hot spot. C is the counterjet candidate, and parts of the ridge through B to the counterjetted hot spot A may be an extension of the counterjet. Contours are drawn at −1 (dotted), 1, 2, 3, 4, 6, 8, 10, 12, 16, 20, 30, 40, 60, 80, 100, 200, 300, 400, 600, 800, and 1000 times 60 μJy per CLEAN beam area. The peak intensity is 86.3 mJy per CLEAN beam area.

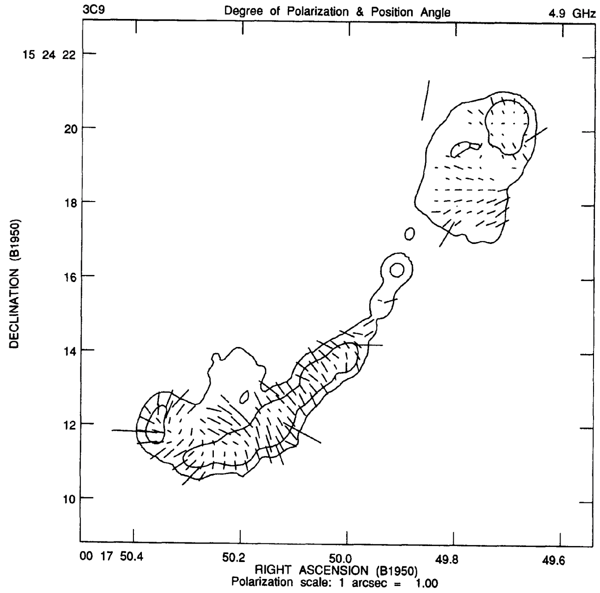

FIG. 2. Distribution of degree of linear polarization p and **E**-vector position angle χ over 3C 9 at 0″.36 resolution, superposed on contours from Fig. 1. A vector of length 1″ corresponds to p=1.

lobes is greatest at their outer edges, where it reaches ~40% in the southeast (jetted) lobe and ~30% in the northwest (counterjetted) lobe.

4.3 3C68.1

Figure 3 shows the total intensity image at 1."1 resolution from the B configuration data only. The source is a wide (53", $228h^{-1}$ kpc) double with symmetrically placed but asymmetrically bright lobes (the integrated flux density of the northern lobe is 16 times that of the south lobe at 4.9 GHz). The weak central feature E had not previously been detected. Its radio position agrees well with that of the optical identification. Between feature E and the north lobe is an elongated feature D, that appears to be a bright segment of a jet pointing toward a ridge in the north lobe. There is an isolated, extended, bright knot (F) on the likely path of a counterjet, directly opposite the peak of feature D. At this resolution, there are several subsidiary peaks (G,H,I) in the south lobe.

Figure 4 shows the polarization data at 1."1 resolution superposed on contours from Fig. 3. In the lobes, the **E** vectors are perpendicular to the adjacent boundary, and confused near the bright hot spots. At this resolution, the north jet is only weakly (9%) linearly polarized.

Figure 5(a) shows the total intensity of the north lobe, jet, and the central feature at 0."35 resolution from the combined A and B configuration data. Figure 5(b) shows the south lobe

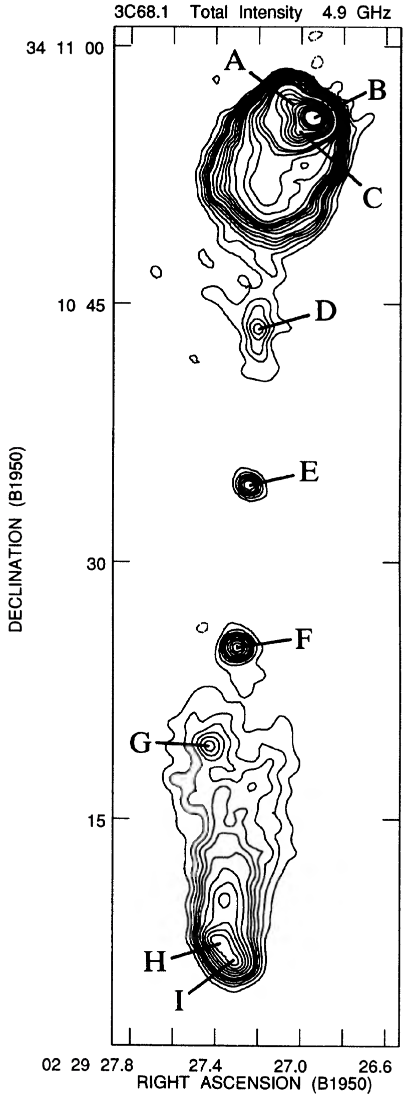

FIG. 3. Distribution of total intensity (Stokes I) over 3C 68.1 with 1."1 (FWHM) resolution. E is the central feature and B is the jetted hot spot. D, C, and the ridge joining them are the jet, and F is the counterjet candidate. Contours are drawn at −1 (dotted), 1, 2, 3, 4, 5, 6, 8, 10, 12, 14, 16, 20, 30, 40, 60, 80, 100, 200, 300, 400, 500, 600, 800, 1000, 1200, and 1400 times 150 μJy per CLEAN beam area. The peak intensity is 311 mJy per CLEAN beam area.

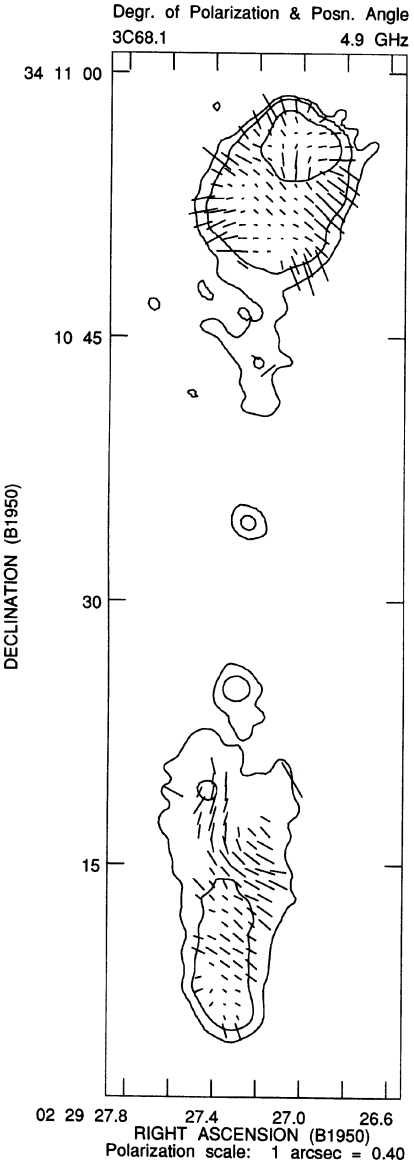

FIG. 4. Distribution of degree of linear polarization p and E-vector position angle χ over 3C 68.1 at 1."1 resolution, superposed on contours from Fig. 3. A vector of length 1" corresponds to p=0.4.

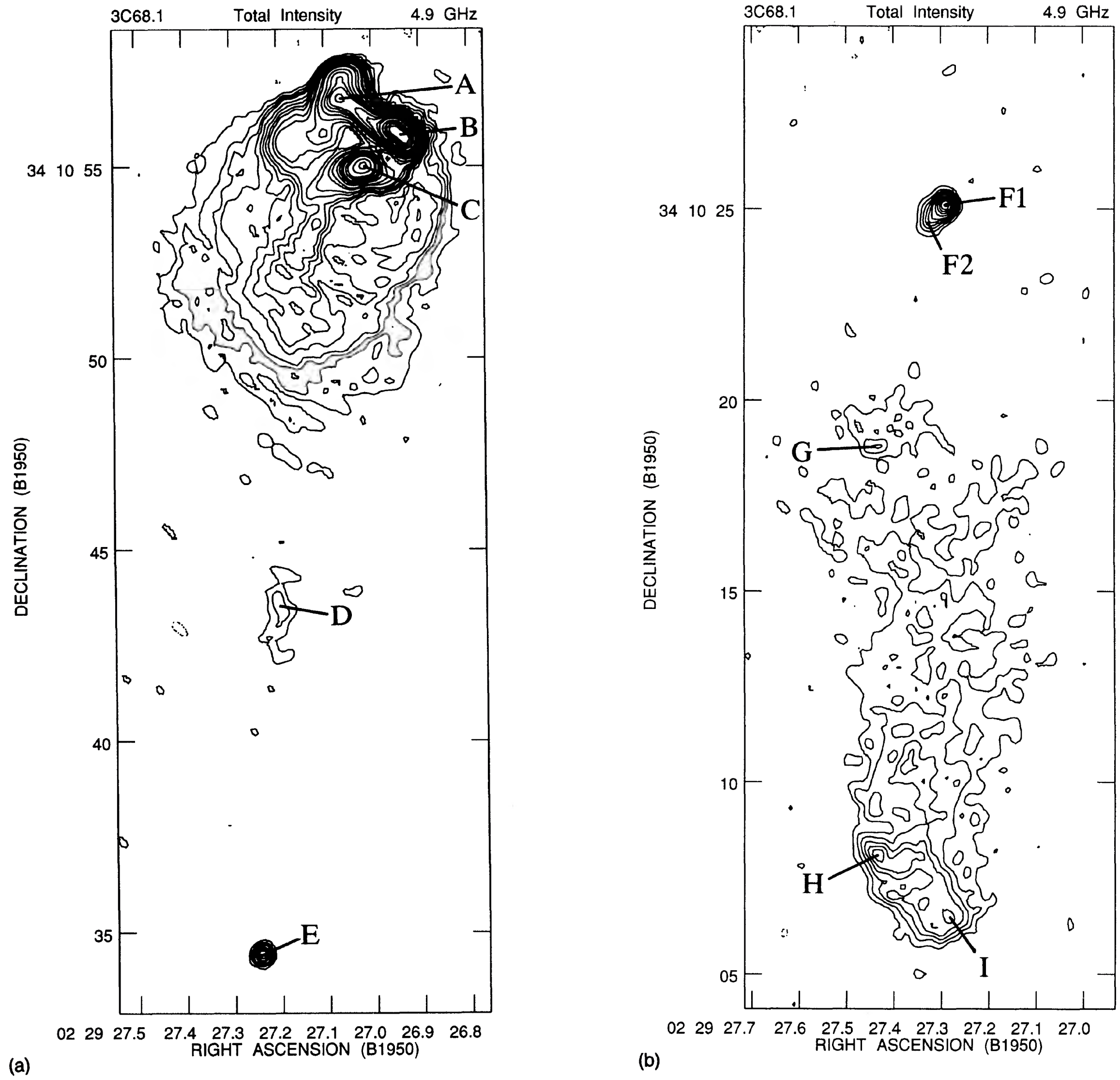

FIG. 5. Distribution of total intensity (Stokes I) over 3C 68.1 with 0″.35 (FWHM) resolution. (a): North lobe, jet (D, C and the ridge joining them), and central feature (E). Contours are drawn at −1 (dotted), 1, 2, 3, 4, 6, 8, 10, 12, 16, 20, 30, 40, 60, 80, 100, 120, 160, 200, 300, 400, 600, 800, 1000, and 1200 times 80 μJy per CLEAN beam area. (b): South lobe and counterjet candidate (F1, F2). Contours are drawn at −1 (dotted), 1, 2, 3, 4, 5, 6, 8, 10, 12, 14, and 16 times 60 μJy per CLEAN beam area. The peak intensity is 124 mJy per CLEAN beam area.

and the possible counterjet knot F at the same resolution. The sensitivity of these images near the north lobe and jet knot D is limited by sidelobe responses to the northern hot spot.

Both D and F are resolved along the major axis of the source, but their morphologies are dissimilar. The jet segment D is well resolved and qualifies as a jet in its own right (Table 8) using the 4:1 axial ratio criterion for jethood. The counterjet candidate F contains a bright, compact knot F1 and a faint extension F2 toward the southeast. We consider this combination a counterjet *candidate* rather than a confirmed counterjet, as it does not satisfy the 4:1 axial ratio criterion.

The bright emission complex in the north lobe is resolved into multiple features (A, B, C and extensions), as previously documented by Swarup *et al.* (1984). A narrow feature extending through the center of the north lobe along the axis of feature D projected toward feature C is taken to be an extension of the jet in what follows. There are also several reasons to believe that feature C is a jet knot. It cannot be the hot spot by our definition, as feature B has higher surface brightness. It might be considered a secondary feature of the lobe (not in the path of the jet), but there is evidence that a sinuous ridge joins its west side to B and its east side to the extension of the jet into the north lobe. Feature C may therefore mark the location of a large change in the direction and the surface brightness of the jet. In what follows, we consider that B, which is the brightest feature in the lobe and lies on the ridge emanating from C, is a hot spot marking the terminus of a jet that deflects and brightens significantly at C. B itself shows evidence for compact substructure (see Table 12). An image with improved angular resolution and sensi-

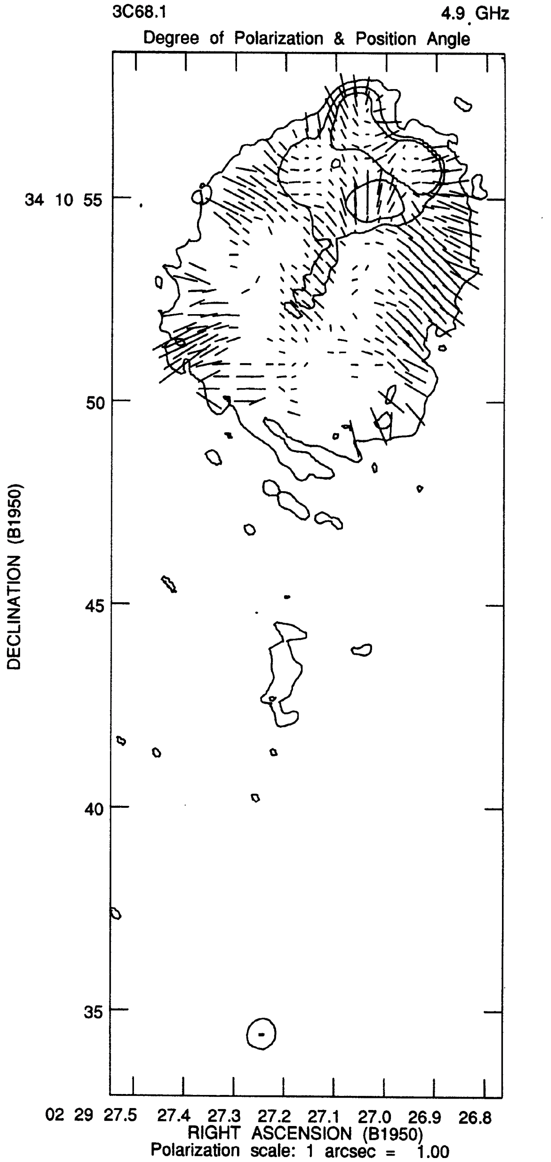

FIG. 6. Distribution of degree of linear polarization p and E-vector position angle χ over the north lobe and jet of 3C 68.1 at 0″35 resolution, superposed on contours from Fig. 5. A vector of length 1″ corresponds to $p=1$.

tivity would be useful to check these interpretations of the northern jet and of the (A+B+C) emission complex.

The most compact feature of the south lobe at this resolution is H, but this has insufficient brightness contrast with other features of the lobe to be considered a hot spot by our definition.

Figure 6 shows the high-resolution polarization data for the north lobe and jet, superposed on contours from Fig. 5(a). There is no significant linearly polarized emission from the jet at this resolution. The increased resolution also reveals a well organized pattern in the lobe's polarization: the **E** vectors tend to be perpendicular to the adjacent lobe boundary, and to the ridge line of the probable outer jet. The degree of polarization increases from <20% to ~50% toward the outer edges of the lobe. This resolution also shows that the counterjet candidate (not shown in Fig. 6) is about 5% linearly polarized at the peak F1, and about 15% polarized at the south and west edges of the more extended emission F2 near this peak.

4.4 3*C*175

Figure 7 shows the total intensity image at 1″3 resolution from the B configuration data only. The source is a wide (52″, $212h^{-1}$ kpc) double with asymmetrically placed lobes that have faint extensions toward the center of the source. A previously unknown jet links the central feature to the fainter, further southwest lobe. Although the contour at 100 μJy per CLEAN beam area apparently extends along a plausible counterjet path just to the east of the central feature, this detail is close to the level of the peak fluctuations far from the lobes. As there is no evidence for elongated emission here in our higher-resolution data (see Fig. 8), we conclude that there is no credible evidence for a counterjet.

Figure 8 shows the total intensity image at 0″38 resolution from the combined A and B configuration data. The inner jet follows PA 237°4±0°3 for the first 12″ ($49h^{-1}$ kpc) between the compact central feature M and knot I, but further out it curves southward toward feature D in the southwest lobe. It expands steadily between features L and H. Beyond H the transverse brightness profile is asymmetric, with sharper gradients to the northwest.

Using our classification scheme, the compact feature C is the hot spot, based on the evidence for a large, abrupt change in the ridge line direction and dramatic decollimation beyond it. Note, however, that the less compact feature A protrudes through the wall of the lobe at its southwest edge and is close to the continuation of the original line of the jet. Although these are attributes of features that might be called hot spots in other sources, there is insufficient brightness contrast between A and the nearby lobe emission for A to meet our definition of a hot spot. (Feature A therefore fails to meet our definition in its own right as well as by comparison with C). The northeast lobe is strongly edge-brightened and has the compact hot spot (O) at its outermost edge. This hot spot is at the vertex of a bright "U"-shaped region of emission that extends away from and behind it on both sides. Note that O is displaced from the axis of the inner jet projected into the northeast lobe, but this axis intersects the narrower northern arc of the U-shaped emission region near the hot spot. The outer boundaries of both lobes are delineated by sharp brightness gradients, to the south and west in the southwest lobe and to the south and east in the northeast lobe.

Figures 9(a) and 9(b) plot the polarization data for the lobes on contours from Fig. 8. The degree of linear polarization of the jet varies from <14% at knot I to 31% at knot K, but the signal is marginal except near the first knot and for about 5″ before feature D. The **E** vectors are within 10° of perpendicular to the jet axis at knots L and K but become closer to parallel by feature D, where the degree of polarization again rises to 29%. On the extended ridges within the lobes, the **E** vectors are generally perpendicular to the ridge

1994AJ....108..766B

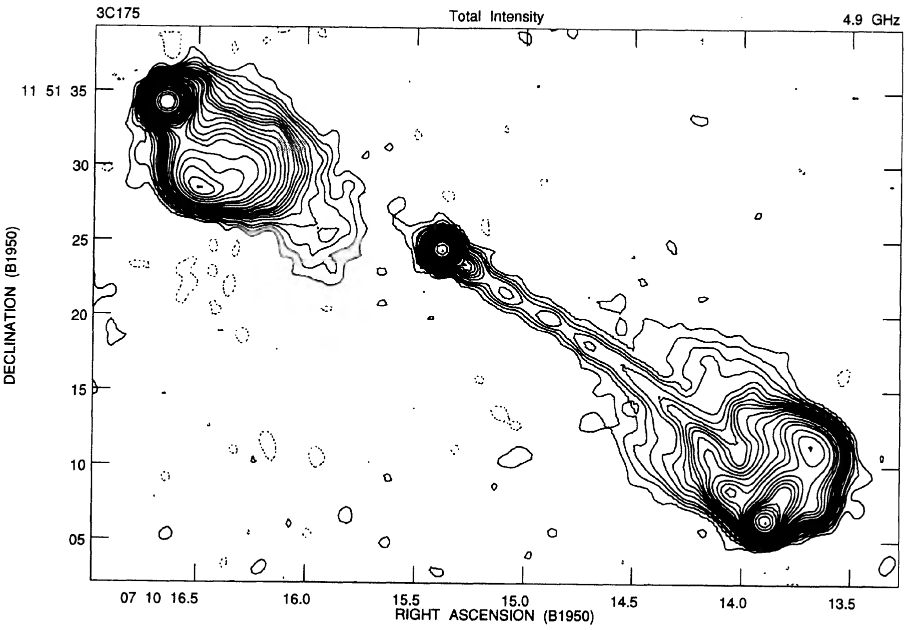

FIG. 7. Distribution of total intensity (Stokes I) over 3C 175 with 1.″3 (FWHM) resolution. Contours are drawn at −1 (dotted), 1, 2, 3, 4, 6, 8, 10, 12, 14, 16, 20, 24, 30, 40, 50, 60, 80, 100, 120, 140, 160, 200, 240, 300, 400, 500, 600, 800, and 1000 times 100 μJy per CLEAN beam area. The peak intensity is 145 mJy per CLEAN beam area.

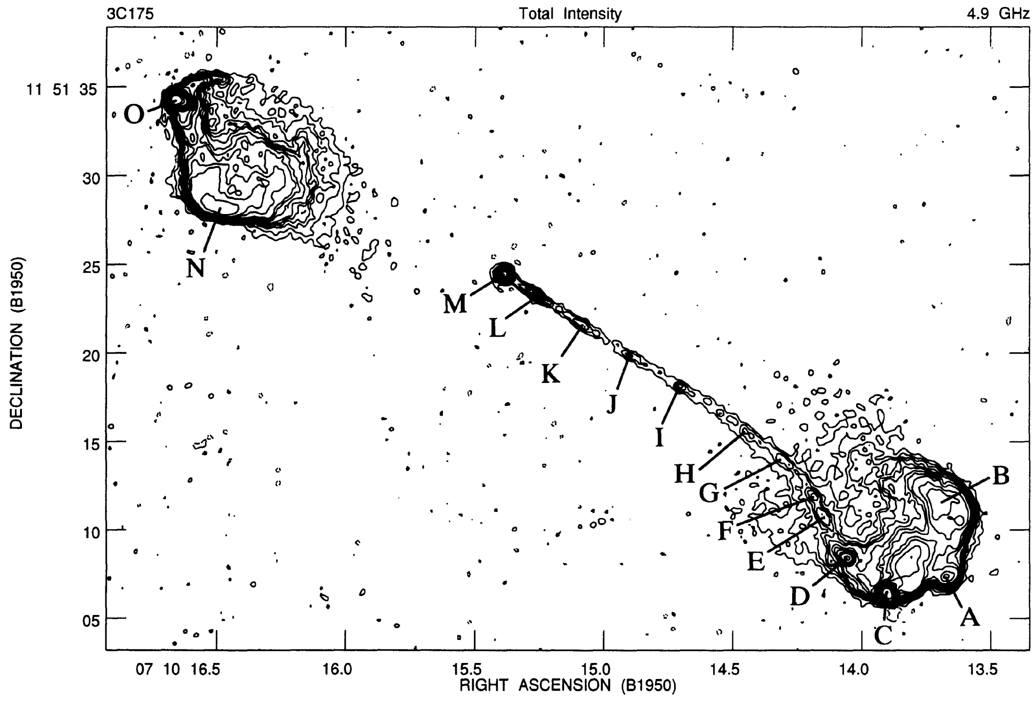

FIG. 8. Distribution of total intensity (Stokes I) over 3C 175 with 0.″38 (FWHM) resolution. M is the central feature and C is the jetted hot spot. O is the counterjetted hot spot and there is no counterjet candidate. Contours are drawn at −1 (dotted), 1, 2, 3, 4, 5, 6, 8, 10, 12, 16, 20, 30, 50, 70, 100, 120, 160, 200, 300, 500, 700, 1000, and 1200 times 50 μJy per CLEAN beam area. The peak intensity is 65.0 mJy per CLEAN beam area.

1994AJ....108..766B

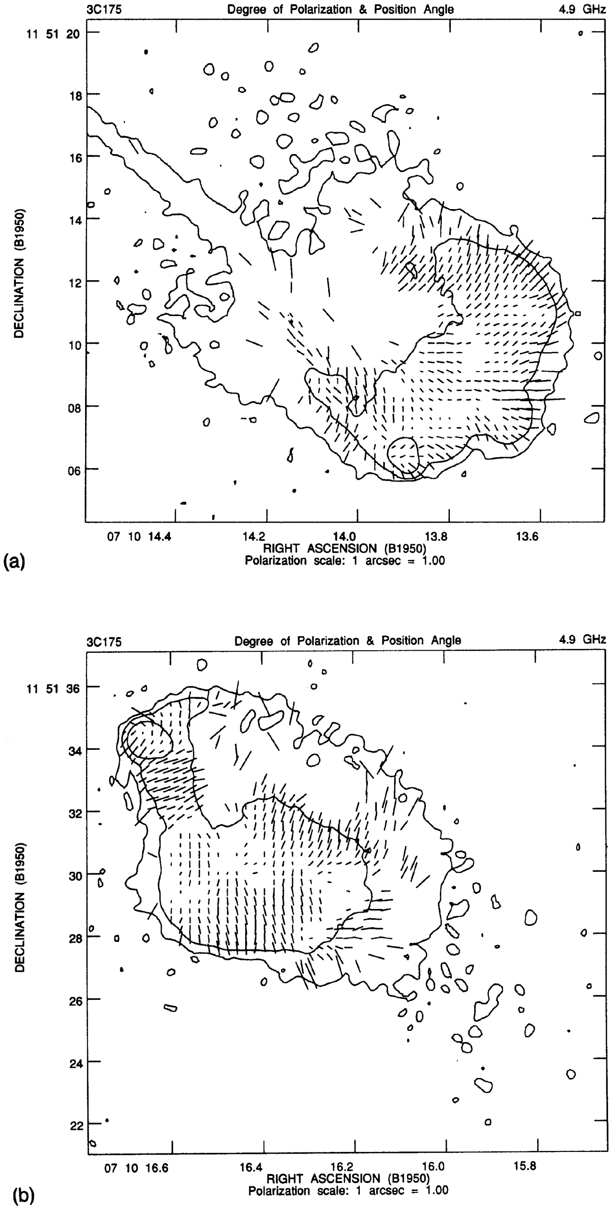

FIG. 9. Distribution of degree of linear polarization p and **E**-vector position angle χ over 3C 175 at $0\farcs38$ resolution, superposed on contours from Fig. 8. A vector of length 1″ corresponds to $p=1$. (a): Southwest lobe. (b): Northeast lobe.

lines. Near the hot spots, the distributions are more complex. The highest degrees of polarization occur near the edges of the lobes, 35% to 45% near knot A, and 40% to 55% north of feature B.

4.5 3*C*204

Figure 10 shows the total intensity image at $0\farcs34$ resolution from the A and B configuration data. The source is about 37″ ($159h^{-1}$ kpc) in extent with symmetrically placed lobes, both of which have faint extensions toward the south. Bremer *et al.* (1992) report [O II] emission extending $\sim$8″ south and $\sim$4″ north of the quasar.

A jet consisting of a string of bright knots (I to E) superposed on fainter extended emission links the compact central feature J to a recessed bright feature (D) in the west lobe. The jet axis is roughly perpendicular to the extended optical line emission. The jet is straight for most of its length but deflects toward the north shortly before reaching D. There are further bright features (C and B) downstream before the extended edge-brightened region A. Feature B is noticeably elongated perpendicular to the direction to D and could be considered a candidate for the hot spot. Only D meets our definition, however, because (a) its surface brightness exceeds that of B by a factor of 10 or more, (b) there is a large change in ridge line direction at its location, and (c) there is no evidence for jet emission beyond it that is as well collimated as the emission leading toward it. There is no evidence of a counterjet on the east side although there is a bright hot spot (L) at the eastern edge of the east lobe.

Figures 11(a) and 11(b) plot the polarization data on contours from Fig. 10. The jet has $\sim$20% to $\sim$30% linear polarization at knots I, G, F, and E; the **E** vectors are nearly perpendicular to the jet axis at I and F but are misaligned with it at G and E. On the extended ridges within the lobes, the **E** vectors are generally perpendicular to the ridge lines. Near the brighter features D to B, the distributions are more complex. The highest degrees of polarization (50% to 60%) occur near the edges of the lobes—north of knot B, west of knot A, and on the trailing northern and southern boundaries of the east lobe.

4.6 3C 208

Figure 12 shows the total intensity image at $0\farcs37$ resolution from the A and B configuration data. The source is 14″ ($60h^{-1}$ kpc) in extent with symmetrically placed lobes. A jet consisting of several elongated knots (D,E,F) embedded in fainter emission links the compact feature G to a recessed hot spot (B) in the west lobe. B is the hot spot because it is (a) the brightest feature in the lobe (confirmed by an MEM image not shown here) and (b) the apparent terminus of the jet. The jet is straight for most of its length, but deflects toward the south shortly before reaching B. There is no evidence of a *narrow* counterjet on the east side. It is unclear how the elongated, diffuse feature (H) is related to the other emission from the east lobe, but because it is resolved in all directions there is no strong reason to associate it with a counterjet. It might, however, prevent detection of a narrow counterjet if one took a curved route between G and the hot spot J in the east lobe.

Figure 13 plots the polarization data superposed on contours from Fig. 12. The jet is strongly (40% to 45%) linearly polarized at knots D and F. The detected **E** vectors are within 15° of perpendicular to the jet axis at knot E and beyond, but are misaligned by about 30° with this direction at knot F. On the extended ridges within the lobes, the **E** vectors tend to be perpendicular to the ridge lines. Near the hot spots B and J, the distributions are more complex. The highest degrees of polarization (25% to 40%) in the lobes occur near their edges.

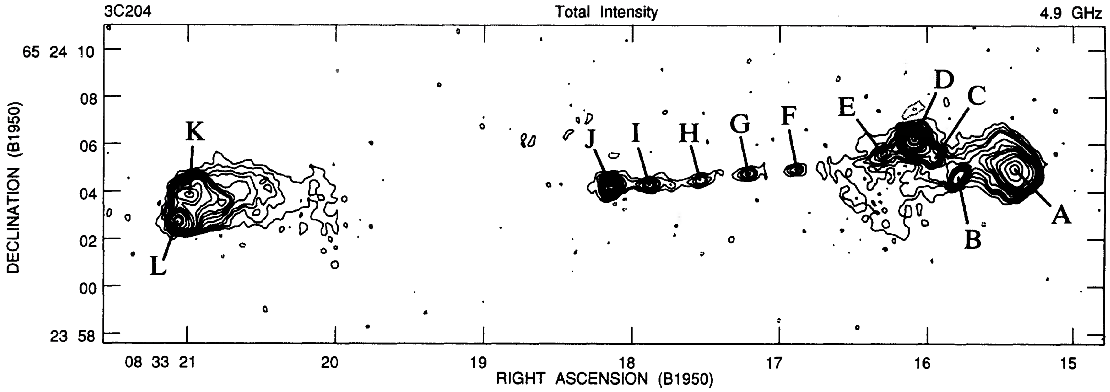

FIG. 10. Distribution of total intensity (Stokes *I*) over 3C 204 with 0″.34 (FWHM) resolution. J is the central feature and D is the jetted hot spot. L is the counterjetted hot spot and there is no counterjet candidate. Contours are drawn at −2 and −1 (dotted), 1, 2, 3, 4, 6, 8, 10, 12, 16, 20, 30, 40, 60, 100, 200, 300, and 500 times 70 μJy per CLEAN beam area. The peak intensity is 42.4 mJy per CLEAN beam area.

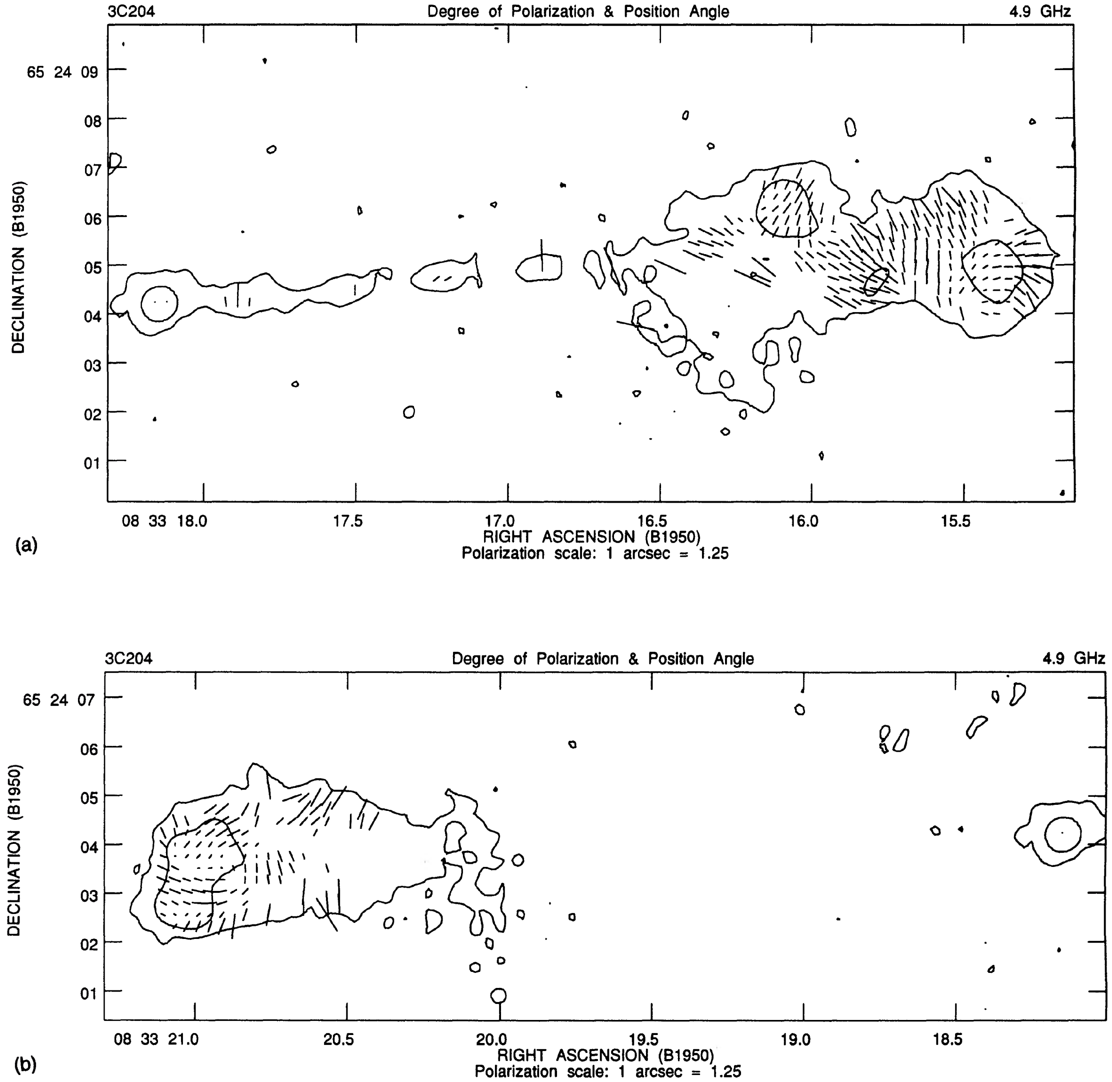

FIG. 11. Distribution of degree of linear polarization p and E-vector position angle χ over 3C 204 at 0″.34 resolution, superposed on contours from Fig. 10. A vector of length 1″ corresponds to $p=1.25$. (a): West lobe, jet and central feature. (b): East lobe and central feature.

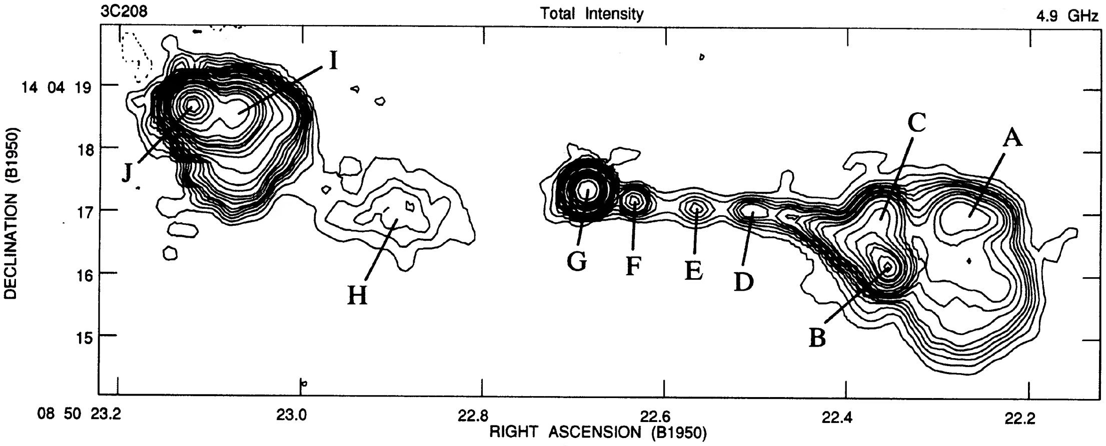

FIG. 12. Distribution of total intensity (Stokes I) over 3C 208 with 0″.37 (FWHM) resolution. G is the central feature and B is the jetted hot spot. J is the counterjetted hot spot and there is no counterjet candidate: the broad feature H is considered to be confusing lobe emission (see text). Contours are drawn at −1 (dotted), 1, 2, 3, 4, 5, 6, 8, 10, 12, 16, 20, 30, 50, 70, 100, 120, 160, 200, 300, 500, 700, 1000, and 1200 times 100 μJy per CLEAN beam area. The peak intensity is 145 mJy per CLEAN beam area.

4.7 3C 215

A 2.2 mJy source at (B1950.0) $09^{\mathrm{h}}\ 03^{\mathrm{m}}\ 48^{\mathrm{s}}.90$, +16° 58′ 49″.3 and a 1.6 mJy source at (B1950.0) $09^{\mathrm{h}}\ 03^{\mathrm{m}}\ 43^{\mathrm{s}}.29$, +16° 57′ 27″.0 are not shown in our figures but their effects were subtracted from all images of 3C 215. Neither of these sources aligns with the radio structure of 3C 215 in any way that suggests a physical relationship to the quasar.

Figure 14(a) shows the total intensity image at 1″.2 resolution from the B configuration data only. The source has a complex structure ~60″ ($196h^{-1}$ kpc) in extent. The compact feature C coincides with the optical identification. The north lobe is edge-brightened and broad with an extended region of enhanced emission that peaks at A. The south lobe is edge-darkened and resembles a multiply twisted plume. A jet enters it on a twisted path almost at right angles to the axis of elongation of the plume on its southward path. There is an elongated spine of emission in the north lobe that may be a counterjet, linking the weak feature B to the region near the peak of feature A. [The ridge line of this counterjet candidate is marked by large perturbations in the 2, 6, and 16 times 75 μJy/beam contours between B and A in Fig. 14(a), and by smaller perturbations in all the other contours along its path—see also the grey scale representation in Fig. 14(b)].

Figure 15, also at 1″.2 resolution, plots the polarization data on contours from Fig. 14(a). At this resolution, the polarization structure of the jet is smeared by the beam, but a complex distribution of polarization is evident across both lobes. The degree of polarization is greatest (45% to 60%) on the south and west edges of the north lobe and in the south lobe immediately below the jet. The **E** vectors are roughly perpendicular to the plume-like extensions of the south lobe, and to the ridge line of A. Elsewhere, the polarization distribution is complex and the **E** vectors show no simple (parallel or perpendicular) relationship to the major features.

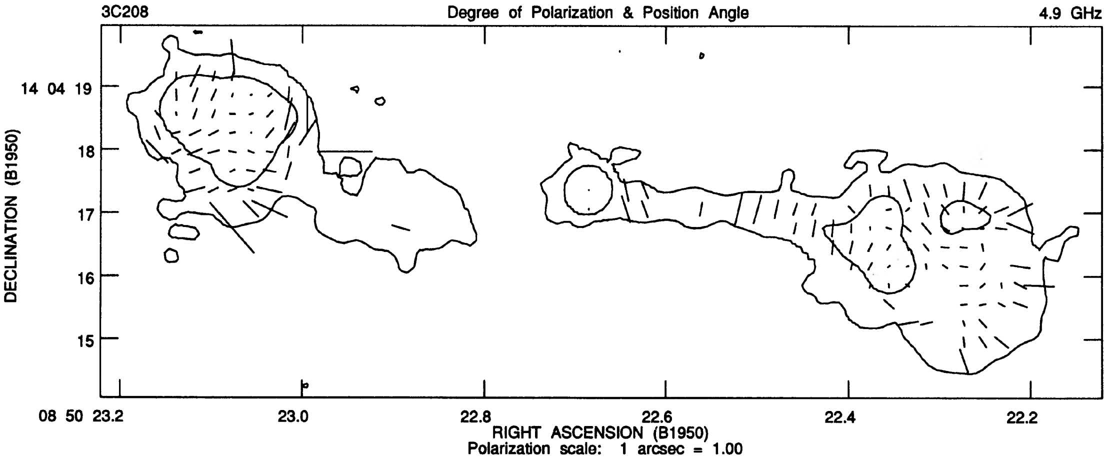

FIG. 13. Distribution of degree of linear polarization p and E-vector position angle χ over 3C 208 at 0″.37 resolution, superposed on contours from Fig. 12. A vector of length 1″ corresponds to $p=1$.

1994AJ....108..766B

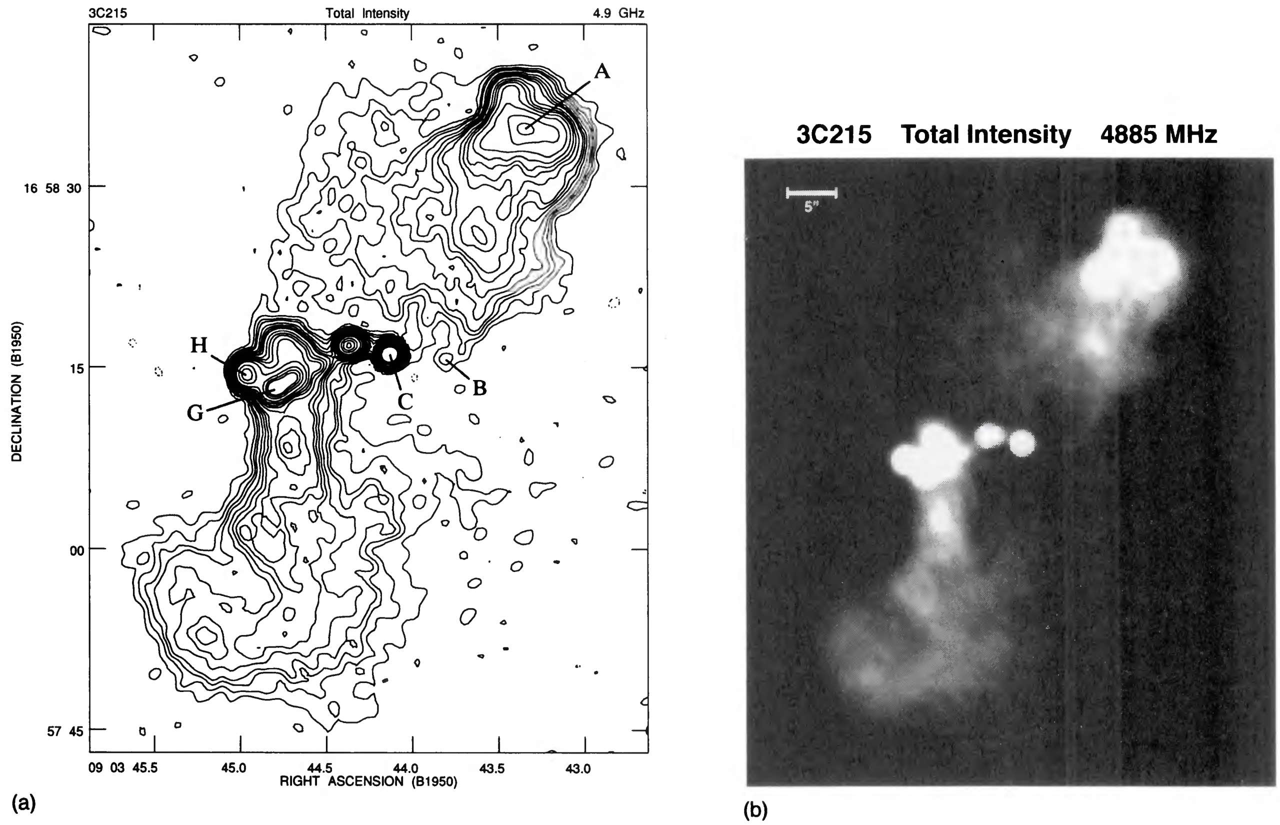

FIG. 14. Distribution of total intensity (Stokes I) over 3C 215 with 1."2 (FWHM) resolution. C is the central feature and G is the jetted hot spot. The counterjet candidate is B and the faint ridge linking it to A. (a): Contours drawn at −1 (dotted), 1, 2, 3, 4, 6, 8, 10, 12, 16, 20, 24, 30, 40, 60, 80, and 100 times 75 μJy per CLEAN beam area. The peak intensity is 16.2 mJy per CLEAN beam area. (b): Greyscale display emphasizing the flux density range containing the counterjet candidate.

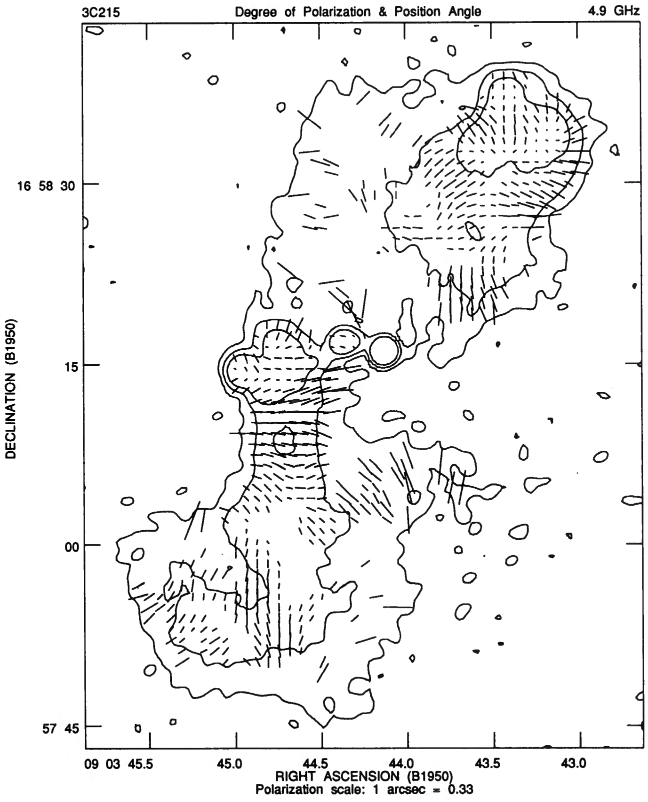

FIG. 15. Distribution of degree of linear polarization p and E-vector position angle χ over 3C 215 at 1."2 resolution, superposed on contours from Fig. 14. A vector of length 1" corresponds to $p=0.33$.

Figure 16 shows the total intensity image at 0."37 resolution from the A and B configuration data.

Figure 17(a) shows an enlargement of the inner region, which includes a series of bright curved knots (D,E,F) marking major bends in the path of a multiply twisted jet. A higher-resolution MEM deconvolution of this region shows feature G to be much brighter and more compact than the immediately preceding jet knots E and F. We classify G as the hot spot because it is also the site of a sudden change in the ridge line direction. (It meets our brightness contrast criterion for a hot spot on the normal high-resolution image after deconvolution of the synthesized beam.)

The diffuse feature H resembles a strongly, but smoothly curved section of jet, however, so that G might also be classifiable as a jet knot. On this alternative interpretation, there would be no hot spot terminating the jet. This might be consistent with the lobe's plume-like morphology, which resembles that of a low-power Fanaroff–Riley (1974) Type I source. The north lobe also lacks a clear hot spot, although it is edge-brightened.

Figure 17(b), also at 0."37 resolution, plots the polarization data for the jet and its environs on contours from Fig. 17(a). The jet knots are ~10% to ~20% linearly polarized. In most regions of the jet, the **E** vectors are perpendicular to the curved ridge line, and at the hot spot G, they are parallel to the incoming jet direction (as expected if it indeed marks an abrupt compression of an incident flow). Much of the

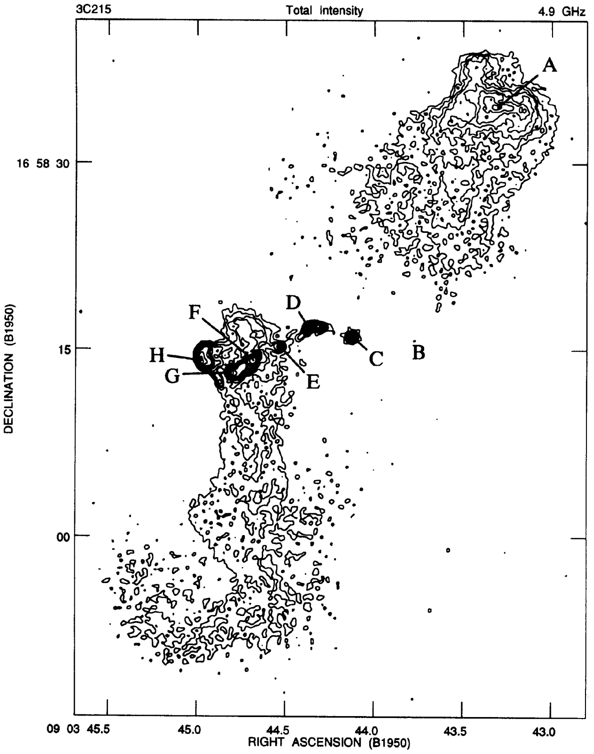

FIG. 16. Distribution of total intensity (Stokes *I*) over 3C 215 with 0″.37 (FWHM) resolution. C is the central feature and G is the jetted hot spot. The counterjet candidate is B and a faint ridge linking it to A (see also Fig. 14). Contours are drawn at −1 (dotted), 1, 2, 3, 4, 6, 8, 10, 12, 16, 20, 30, 50, 70, 100, and 200 times 60 μJy per CLEAN beam area. The peak intensity is 16.5 mJy per CLEAN beam area.

region around the jet segment from E to G is >60% polarized.

The relationship of the extended hook-like feature H to the jet is unclear. The **E** vectors in this region are perpendicular to the boundaries of the extended emission. Both the polarimetry and the total intensity data are consistent with the region north of the jet being the brightest part of a twisted plume that eventually meanders south to form the edge-darkened south lobe.

3C 215 is evidently an ambiguous source. It lacks many characteristics typical of strong sources, except for the compact appearance of knot G in the MEM image. It is noteworthy that this source, which has the most distorted jet and lobe structures in our sample, also has the longest *continuous* counterjet candidate.

4.8 3C 249.1

Figure 18 shows the total intensity image at 1″.1 resolution from the B configuration data combined with data from a snapshot observation in the C configuration kindly made available to us by R. Barvainis. The two lobes are asymmetric in size, intensity and surface brightness. The structure is ~53″ ($149h^{-1}$ kpc) in extent. The west lobe is edge-brightened with a well resolved hot spot (A) near its western end. The east lobe is edge-darkened except for a resolved ridge (L) along its southern boundary. A jet enters it on its extreme southern edge and terminates abruptly at K, only 7″.7 ($22h^{-1}$ kpc) from the central feature D. There is enhanced emission at C and B along a plausible counterjet path from the central feature D toward region A in the west lobe.

Figure 19, also at 1″.1 resolution, plots the polarization data on contours from Fig. 18. At this resolution, the polarization structure of the jet is smeared by the beam, but a complex distribution of polarization is evident across both lobes. The degree of polarization is greatest at the edges of the lobes, particularly east of feature K at the end of the jet, where it reaches 55% to 65%. The **E** vectors are roughly perpendicular to the main ridge in the east lobe and to the outer boundaries of the west lobe. Elsewhere, the polarization distribution at this resolution is complex and the vectors show no simple (parallel or perpendicular) relationship to the major features.

Figure 20 shows the total intensity of the jet and west lobe at 0″.35 resolution from the combined A, B, and C configuration data. All structures in the east lobe are fully resolved. The jet bends at least twice, near E and F, on its path to the resolved terminal hot spot K at its east end. A feature suggested by this image, and strongly supported by a higher-resolution MEM deconvolution, is that the jet bends sharply to the north and turns south again before entering the hot spot K from the northwest. There is also a curious, extended feature (H) running north–south that appears to connect to the jet near its most southern point, just west of knot I. A broad ridge joins the enhanced southern boundary feature L in the outer part of the east lobe to the region near the jet. The hot spot A in the west lobe is well resolved, with a hint of a shell structure reminiscent of that in the north lobe of 3C 219 (Perley *et al.* 1980; Clarke *et al.* 1992).

The emission along the putative counterjet path is a narrow elongated ridge for the first 3″ from the compact feature D, but peak C resolves into a diffuse arc whose status as counterjet-related emission is arguable. This arc is similar in size and luminosity to the "rings" in Hercules A (Dreher & Feigelson 1984). Feature B, also on a plausible path for a counterjet, has a similar flux density and size but is less obviously ring-like.

Figure 21 plots the polarization data at 0″.35 resolution on contours of total intensity. There is little polarization detected within 4″ of the central feature, and the degree of polarization peaks at 25% near knot I. The **E** vectors are oblique to the *local* ridge line of the curved jet at several locations, notably knot E and in the region south of feature H. The polarization structure in the east lobe around the jet is complex, with high (65% to 75%) polarizations near the end of the jet. The polarization in the west outer lobe is well organized with the **E** vectors generally perpendicular to the adjacent lobe boundary, but the polarization distribution appears more confused in the inner lobe. The highest degrees of polarization are again at the edges of the lobes, 45% to 55% on the south edge and 35% to 45% on the north edge. No significant polarization is detected near the putative counterjet features.

Richstone & Oke (1977) and Boroson & Oke (1984) describe an emission line system extending for several arcsec-

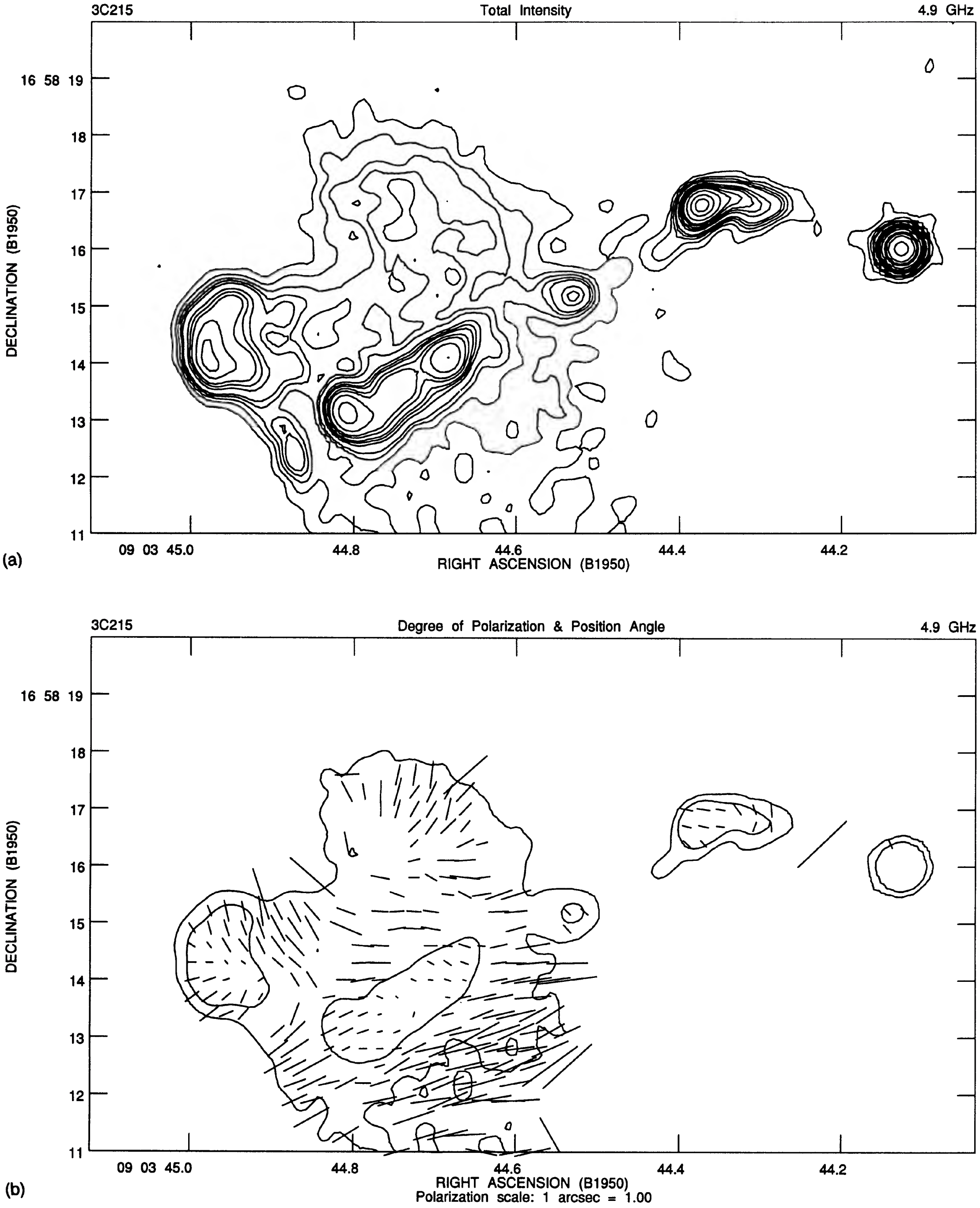

FIG. 17. (a): Enlargement of jet and north part of south lobe from Fig. 16. (b): Distribution of degree of linear polarization p and **E**-vector position angle χ near the jet in 3C 215 at 0."37 resolution, superposed on contours from (a). A vector of length 1" corresponds to $p=1$.

onds around the quasar, plus an extended optical continuum that may be of stellar origin.

4.9 3C 263

Figure 22(a) shows the total intensity image at 0."36 resolution from the A and B configuration data. (Little extra structure was seen on the lower-resolution images.) The structure is 51" ($198h^{-1}$ kpc) in extent. The lobes are asymmetrically placed and unequally bright, the jetted lobe being brighter and closer to the central feature C. A previously undetected jet links C to a bright hot spot (K) in the east lobe. Figure 22(b) is an enlargement of the eastern third of the source. The jet is strikingly linear, but it does not point directly at feature K. There is evidence for a curved "hook" (J) to the northwest of K, which may mark the final path of the deflecting jet. There is also a diffuse "bar" of emission

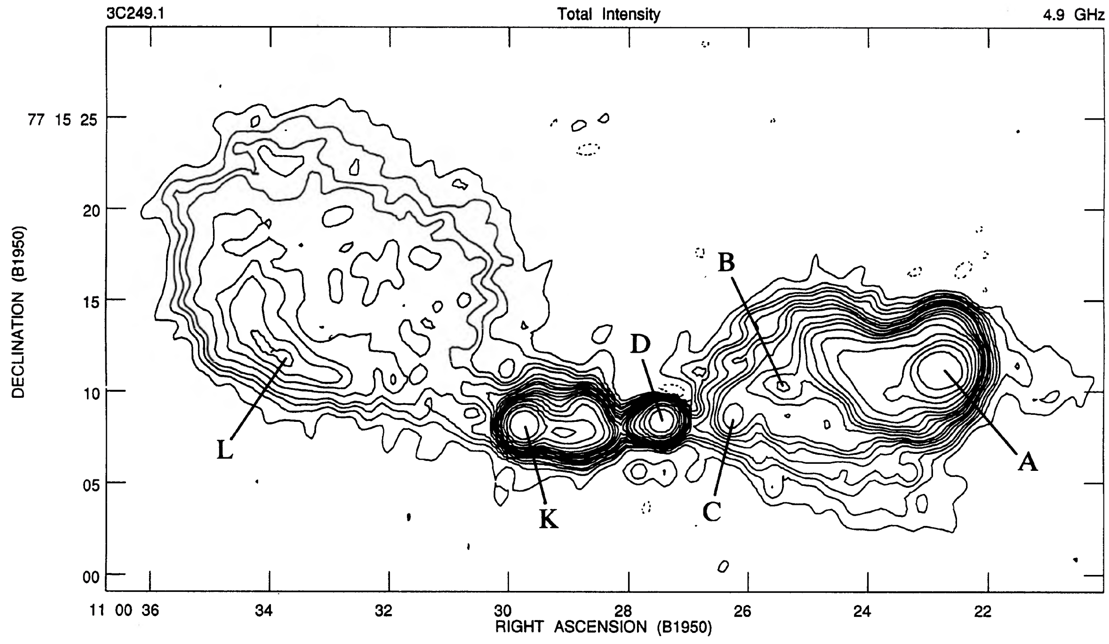

FIG. 18. Distribution of total intensity (Stokes I) over 3C 249.1 with 1.″1 (FWHM) resolution. Contours are drawn at −1 (dotted), 1, 2, 3, 4, 6, 8, 10, 12, 16, 20, 24, 30, 40, 60, 100, 160, and 300 times 100 μJy per CLEAN beam area. The peak intensity is 97.3 mJy per CLEAN beam area.

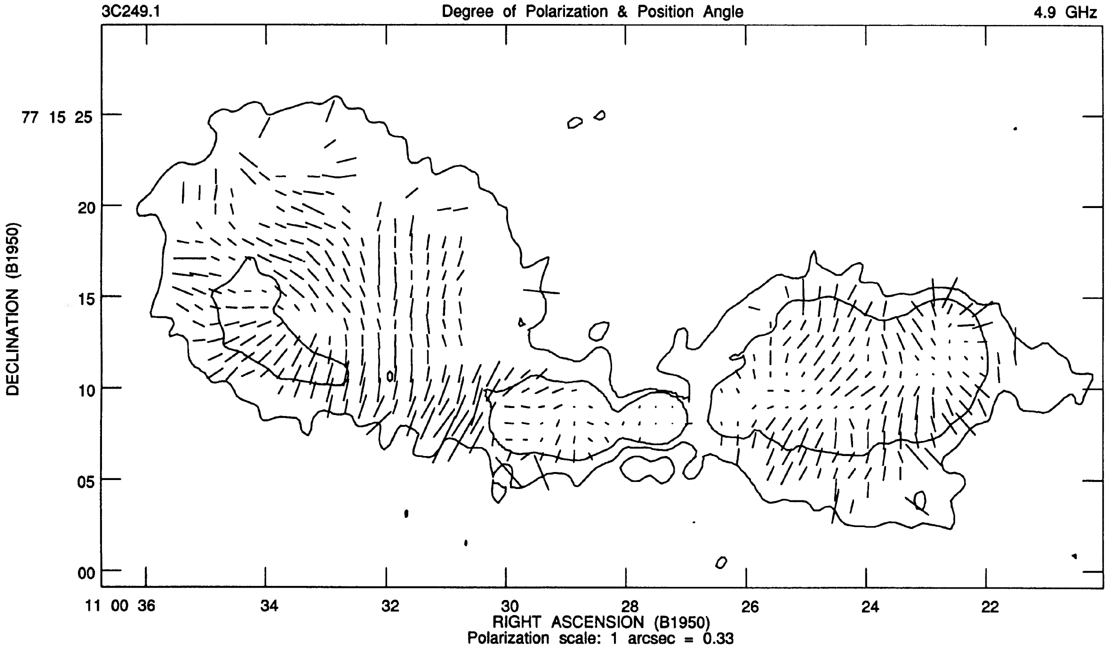

FIG. 19. Distribution of degree of linear polarization p and **E**-vector position angle χ over 3C 249.1 at 1.″1 resolution, superposed on contours from Fig. 18. A vector of length 1″ corresponds to $p=0.33$.

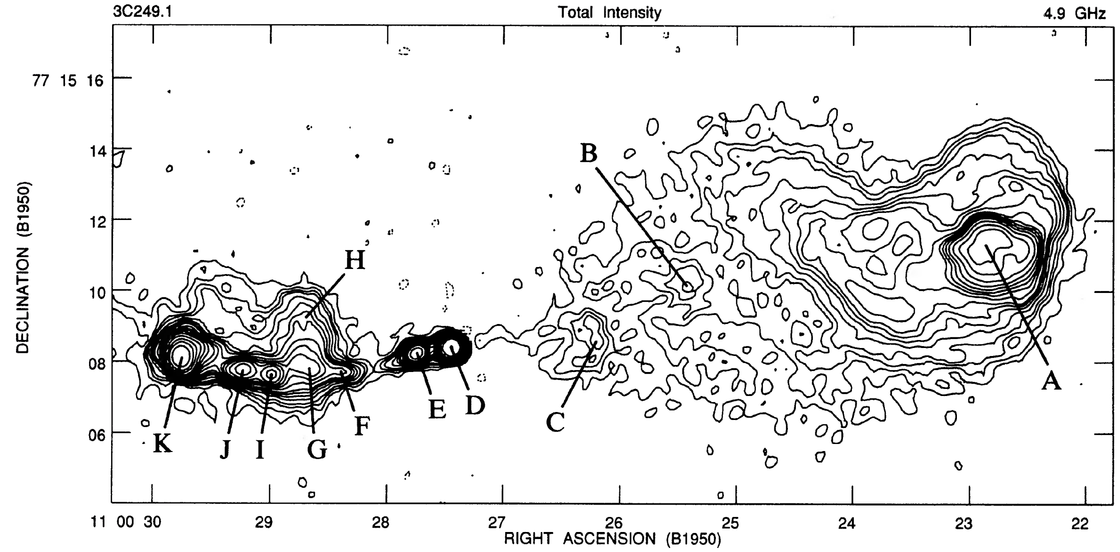

FIG. 20. Distribution of total intensity (Stokes I) over the jet and west lobe of 3C 249.1 from a composite MEM/CLEAN deconvolution restored with 0.″35 (FWHM) resolution. D is the central feature and K is the jetted hot spot. The counterjet candidate is the straight ridge linking D to the north end of the hook-like feature C. A is the counterjetted hot spot. Contours are drawn at −1 (dotted), 1, 2, 3, 4, 6, 8, 10, 12, 16, 20, 24, 30, 40, 60, 100, 160, 300, and 1000 times 65 μJy per restored beam area. The peak intensity is 71.0 mJy per CLEAN beam area.

(I) roughly perpendicular to the jet about 2″ upstream from the hot spot, reminiscent of the jet-crossing feature H in 3C 249.1 (Sec. 4.8). The jet contains a series of bright, elongated knots (D,E,F,G,H) and fainter, apparently continuous emission. (The image of the jet is corrupted by undeconvolvable sidelobes of the bright hot spot K, and only the features that we believe to be significant are labeled.) The west lobe appears more relaxed, with a recessed hot spot (B) and a bright resolved rim (A) to the northwest. There is no emission along the expected path of any similarly straight counterjet.

Figures 23(a) and 23(b), also at 0.″36 resolution, plot the polarization data on contours from Figs. 22(a) and 22(b). There is measurable (15% to ~25%) polarization at jet knots D, F, and G, with the **E** vectors perpendicular to the jet axis. The degree of polarization is <40% over most of the east lobe, but rises to about 50% in the region north of hot spot K and toward the southwest. The polarized signal from the diffuse emission to the north is weak, but there is evidence for 50% to 60% linear polarization near its northern boundary. The area between I and J is only weakly (4% to 8%) polar-

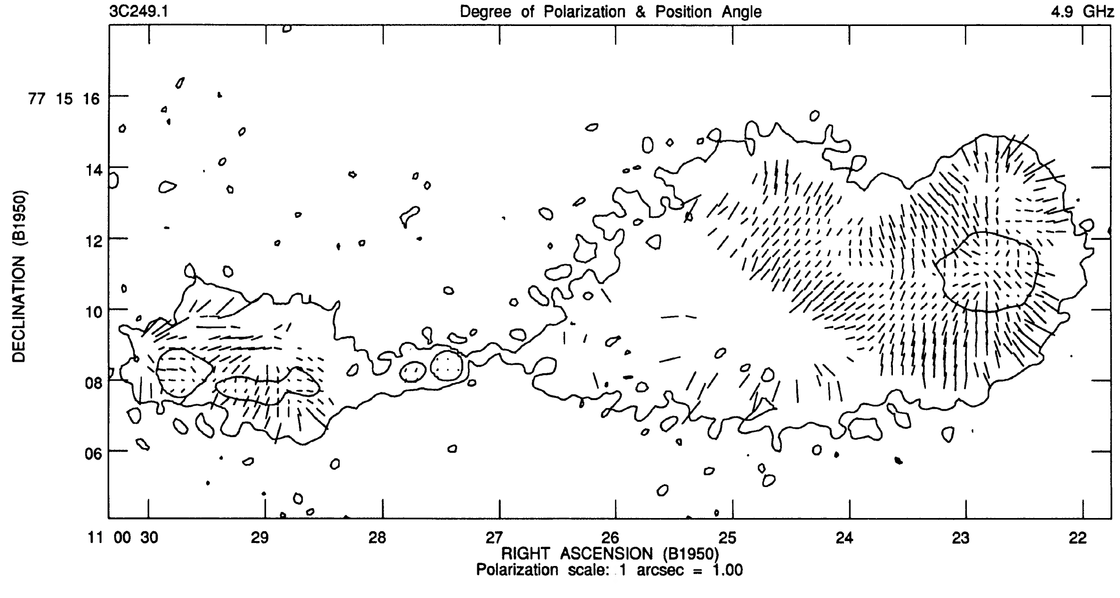

FIG. 21. Distribution of degree of linear polarization p and **E**-vector position angle χ over the jet and west lobe of 3C 249.1 at 0.″35 resolution, superposed on contours of total intensity. A vector of length 1″ corresponds to $p=1$.

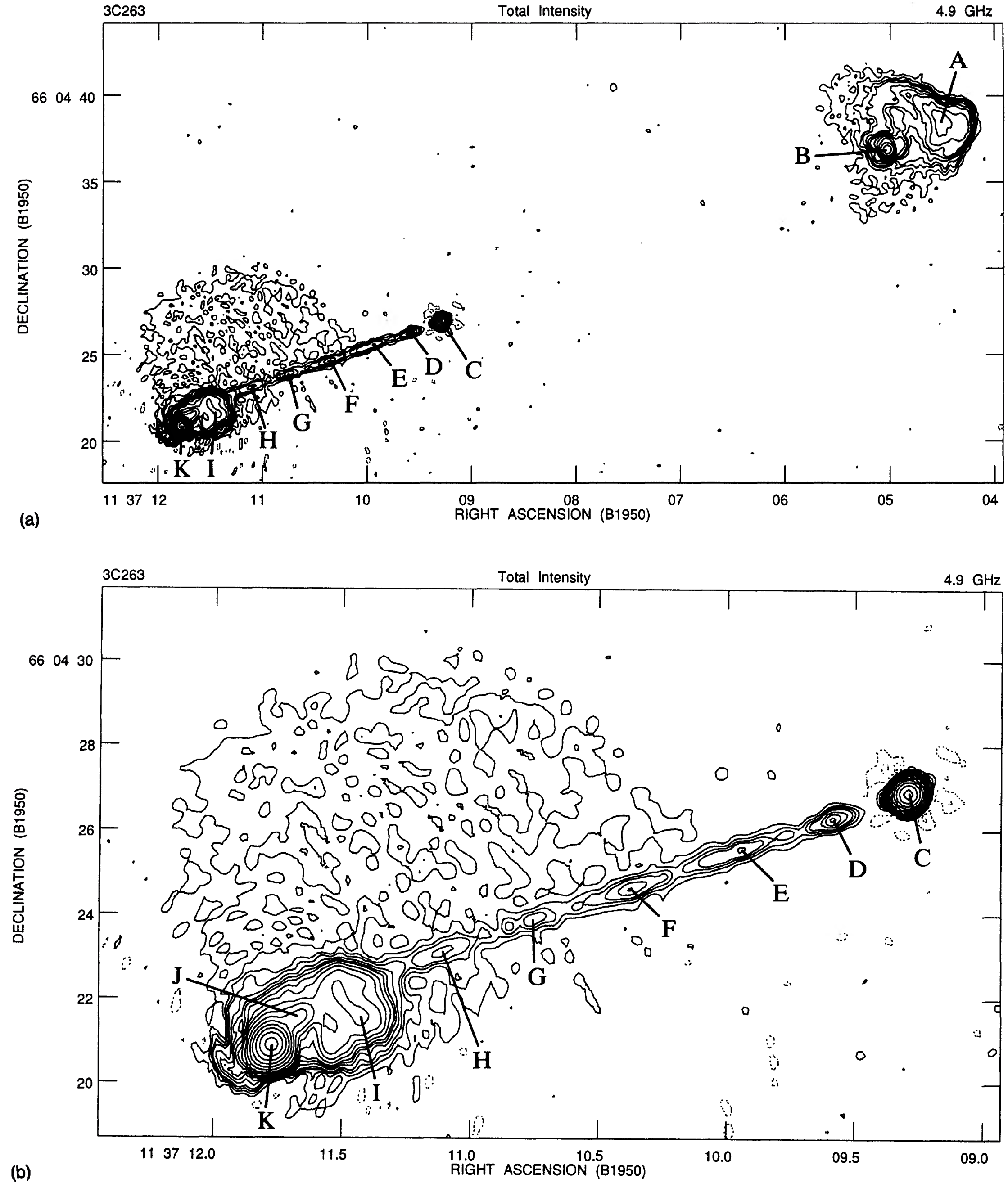

FIG. 22. (a): Distribution of total intensity (Stokes *I*) over 3C 263 with 0″.36 (FWHM) resolution. C is the central feature and K is the jetted hot spot. J has been considered part of the jet. B is the counterjetted hot spot and there is no counterjet candidate. Contours are drawn at −1 (dotted), 1, 2, 3, 4, 6, 8, 10, 14, 20, 30, 50, 100, 200, 400, 800, 1600, and 3200 times 75 μJy per CLEAN beam area. (b): Enlargement of central feature, jet and east lobe. The peak intensity is 347 mJy per CLEAN beam area.

ized. This low polarization, together with the pattern of the surrounding **E** vectors, suggests that the magnetic field direction in feature I is almost orthogonal to that of the adjacent lobe emission and roughly along the ridge of feature I. The degree of linear polarization in the west lobe is up to 50% and the vectors are highly organized, with the **E** vectors perpendicular to the adjacent boundaries of the lobe and parallel to the jet axis near the compact hot spot B.

4.10 3C 334

The data were confused by an 88 mJy compact source at (B1950.0) $16^{h}\,18^{m}\,18^{s}.96$, $+17°\,47'\,01''$. This is not shown in our figures but its effects were subtracted from all the images.

Figure 24 shows the total intensity image at 1″.15 resolution from the B configuration data only. The lobes are

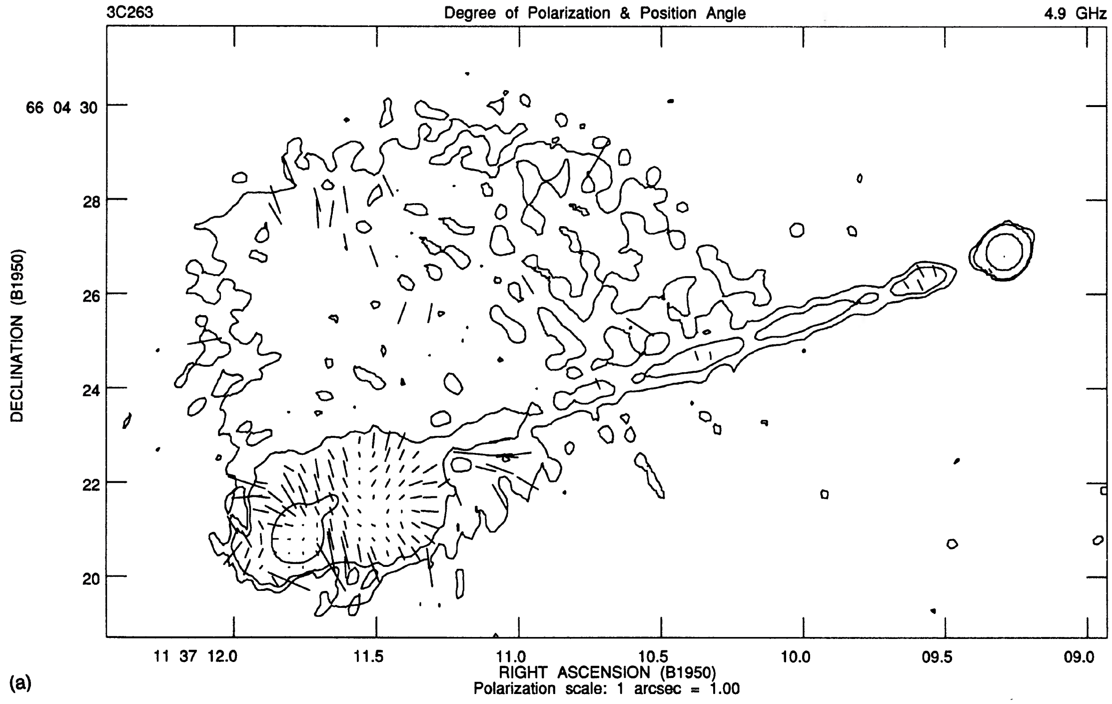

(a)

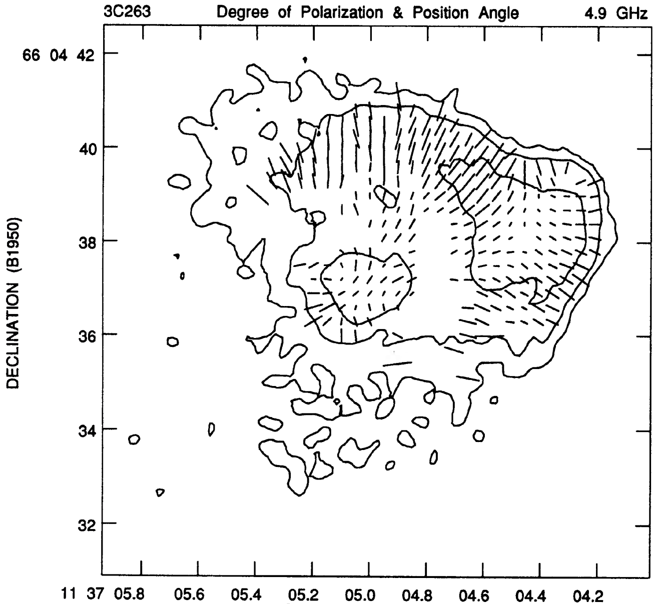

(b)

FIG. 23. Distribution of degree of linear polarization p and E-vector position angle χ over 3C 263 at 0.″36 resolution, superposed on contours from Fig. 22. A vector of length 1″ corresponds to $p=1$. (a): Central feature, jet and east lobe. (b): West lobe.

roughly symmetric in size, intensity, and surface brightness. The structure is ~58″ ($215h^{-1}$ kpc) in extent and has an overall S symmetry. The northwest lobe is sharply bounded to the north and west, but has a plume-like extension to the south. The southeast lobe is weakly edge-brightened on its southeast side, but the lobe emission is everywhere fainter than the jet, which deflects as it enters it from the west.

There is no sign of emission opposite the straight segment of the jet (the first 13″ from the central feature E). There are, however, two relatively compact features on the counterjet axis. The closer, D, is an elongated knot that is connected to the bright complex B in the northwest lobe by a weak bridge of emission. The second is a detached compact 1.8 mJy source (A) 55″ from the central feature, well aligned with the straight segment of the jet at this resolution. Its position is (B1950.0) 16^h 18^m $04\overset{s}{.}86$, +17° 44′ 14.″1.

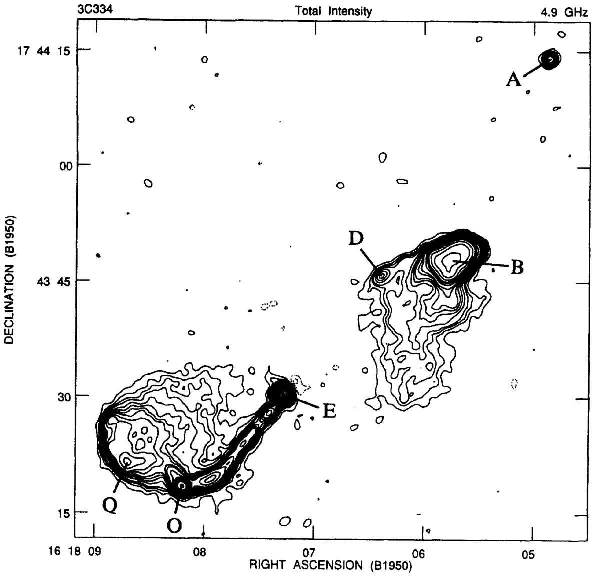

FIG. 24. Distribution of total intensity (Stokes *I*) over the field of 3C 334 with 1.″15 (FWHM) resolution. E is the central feature and A is a confusing source, discussed in the text. O is the jetted hot spot and D is part of the counterjet candidate (see also Fig. 25). Contours are drawn at −2 and −1 (dotted), 1, 2, 3, 4, 6, 8, 10, 12, 16, 20, 30, 40, 50, 70, 100, 150, 200, 300, 500, 700, and 1000 times 110 μJy per CLEAN beam area. The peak intensity is 138 mJy per CLEAN beam area.

We calculate the probability that feature A is a random confusing source as follows. First, we note that the angle between the straight jet axis and the line joining the central feature to A is 1°. We then assume that our attention would have been drawn to any similarly well aligned neighboring source that was within two source diameters of the central feature of any of the 12 sources that we imaged. We use the rms largest angular size (47″) of the 12 sources that we observed to estimate the mean area (0.041 sq arcmin) per source of the sector in which we would have noticed such a good alignment with a particular axis of the source. Further, we consider that there are four axes per source for which an alignment of a neighboring object might be considered "interesting" (e.g., the straight jet axis, the axis opposite to this, and the axes joining the central feature to either hot spot). The 5 GHz source counts of Condon (1984) predict 0.0076 sources per square arcminute brighter than 2 mJy at 5 GHz. Taking all these factors into consideration, we would expect to find only 0.015 "well aligned" confusing sources among our 12 target sources, whereas we observe 1. This estimate of the expected number of confusing sources does not account for the fact that compact, flat-spectrum objects dominate the source counts at high frequency. Feature A is noticeably resolved and has a steep spectral index (1.1 between 1.5 and 5 GHz), which makes it less likely that we would have observed such a well aligned object by chance.

Although this conservative statistical calculation suggests that A may be associated with 3C 334, we have no other reason to believe that it is an outlying part of the source. Specifically, an image of 3C 334 and its environs tapered to 3.″2 (FWHM) resolution showed no evidence of a connection between feature A and the northwest lobe. While it is conceivable that feature A is an outlying remnant of earlier activity in 3C 334, we do not treat it as part of the source structure in what follows.

Figure 25(a) shows the total intensity of the jet and southeast lobe at 0.″35 resolution from the A and B configuration data. All structures in the lobe and the jet are at least partially resolved. The ridge line of the jet oscillates in the first 4″ from the central feature E, but the oscillation does not grow appreciably beyond knot H until the large-scale deflection near knot N. The jet consists of several elongated knots (F,G,H,I,J,K,M,N) embedded in fainter structure. The transverse profile of the jet is clearly asymmetric beyond knot M. A slim "ray" of emission (L and its extension to the northwest) joins the jet from the west near knot N. The sudden >50° change in direction of the ridge line, coupled with the brightness and compactness of feature O, identifies O as the hot spot. Downstream from O, an undulating ridge links features P, Q, R, and S. Beyond Q, this forms the edge-brightened boundary of the lobe. The brightness contrast and appearance of collimation of this ridge might classify it as a jet if it emanated from a central feature rather than from a hot spot. The ridge may therefore be an example of extended secondary outflow from a hot spot. It illustrates the difficulty of distinguishing uniquely between jet and hot spot features.

Figure 25(b) shows the total intensity of the northwest lobe, also at 0.″35 resolution from the combined A and B configuration data. The first knot (D) on the putative counterjet path is resolved, is elongated along this path, and is brightened toward the central feature (E). This knot is at almost the same distance from the central feature as the hot spot O in the southeast lobe. The most compact feature in the northwest lobe (C) lies at the other end of the weak emission ridge that traces the lobe's northern boundary. The weak emission ridge and knot D are therefore candidates for counterjet emission, though the presence of ridges at the edges of other lobes in this sample makes this identification controversial. The bright "head" of the lobe breaks into a complex tangle of knots and filaments for several arcseconds around the peak B at this resolution. Neither B nor C has sufficient brightness contrast with their surroundings to qualify as hot spots by our definition, however, so we adopt the view that there is no hot spot in the northwest lobe. Several filaments appear to trail into the plume-like extension toward the south.

Figures 26(a) and 26(b), also at 0.″35 resolution, plot the polarization data on contours from Figs. 25(a) and 25(b). Linear polarization is detected all along the jet. The degree of linear polarization tends to decrease outward, from ~40% near the base to 20% to 30% in the outer jet. Most **E** vectors are within 10° of the perpendicular to the local ridge line. The narrow "ray" L that joins the jet from the west near its southern limit is apparently >70% polarized, with the **E** vectors perpendicular to its ridge line. The undulating line of knots beyond hot spot O also has **E** vectors perpendicular to the adjacent lobe boundary, except in the region P immediately downstream from O. In the most highly polarized regions away from feature L, on the east edge of the southeast

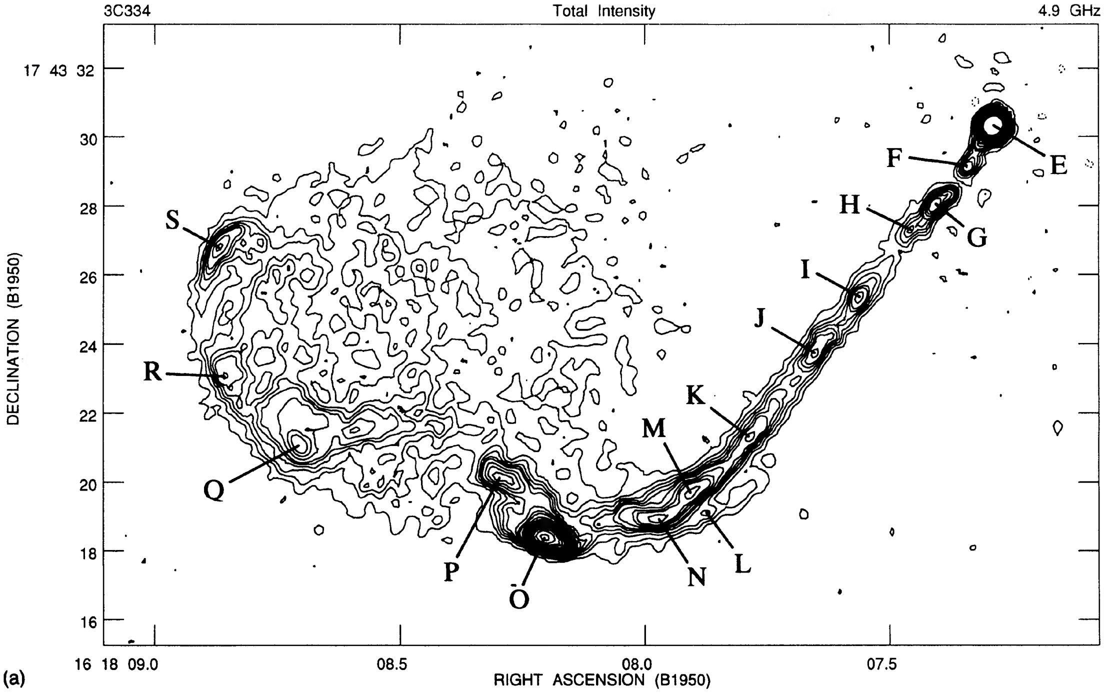

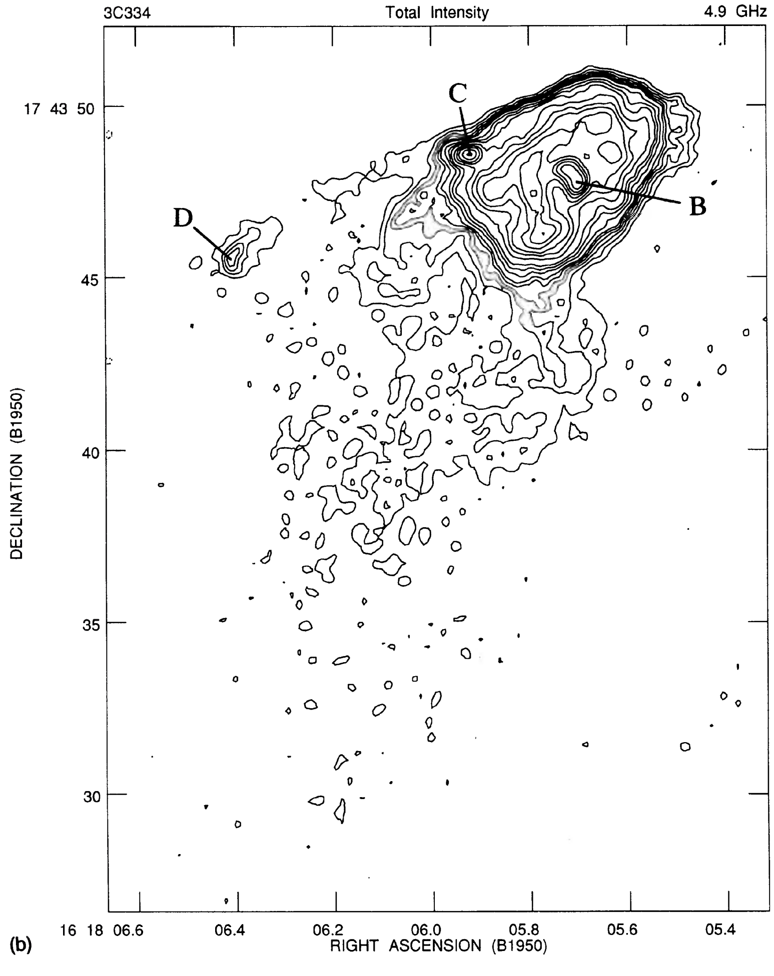

FIG. 25. (a): Distribution of total intensity (Stokes *I*) over the central feature (E), jet, and southeast lobe of 3C 334 with 0."35 (FWHM) resolution. O is the jetted hot spot. Contours are drawn at −1 (dotted), 1, 2, 3, 4, 5, 6, 8, 10, 12, 16, 20, 24, 30, 36, 50, 60, 70, 90, 120, 150, 200, 300, and 500 times 50 μJy per CLEAN beam area. (b): Northwest lobe and counterjet candidate (D and the ridge linking it to C). The peak intensity is 130 mJy per CLEAN beam area.

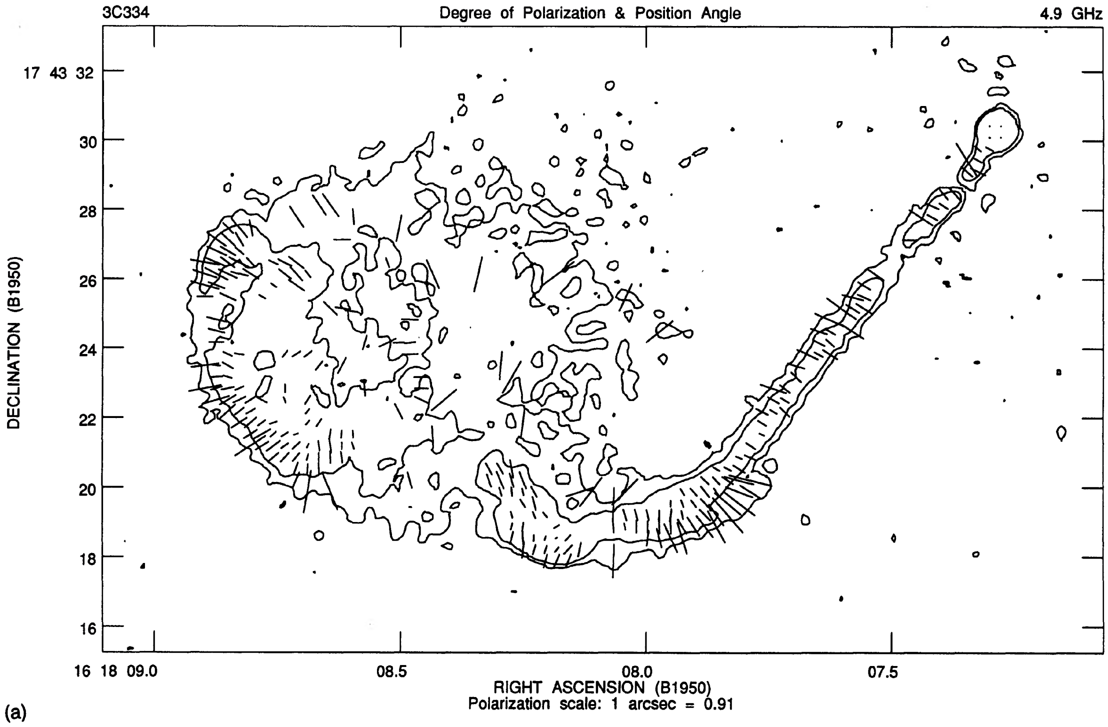

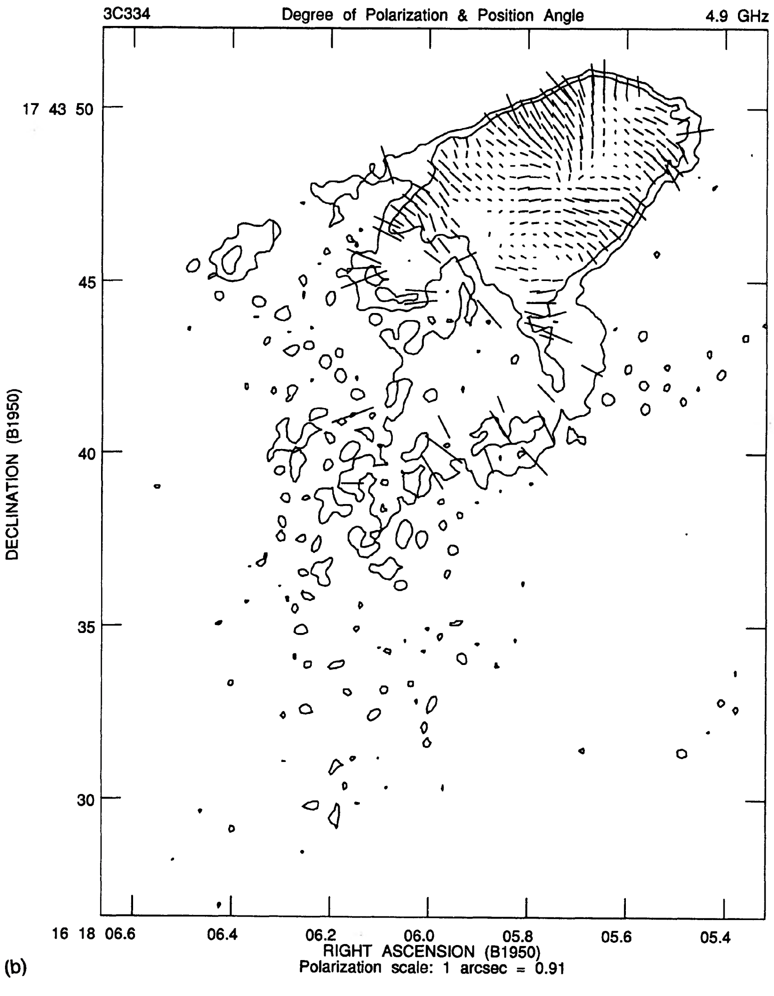

FIG. 26. Distribution of degree of linear polarization p and **E**-vector position angle χ over 3C 334 at 0."35 resolution, superposed on contours from Fig. 25. A vector of length 1" corresponds to $p=0.91$. (a): Central feature, jet, and southeast lobe. (b): Northwest lobe and counterjet candidate.

lobe, the degree of linear polarization ranges from 45% to 50%.

The polarization distribution in the northwest lobe is strikingly well ordered considering the complexity of the brightness distribution. The vector orientations are again perpendicular to the local lobe boundaries and to the ridge lines of the filaments. Unfortunately, the polarized signal from the ridge and knot that are possibly part of the counterjet is undetectable at this resolution. The degree of polarization is highest on the lobe's north edge, where it reaches 50% to 60%, and in a few filaments where it reaches 70%.

4.11 3C 336

Figure 27 shows the total intensity image at 0.″34 resolution from the A and B configuration data. The structure is about 28″ ($118h^{-1}$ kpc) in extent with asymmetrically placed and unequally bright lobes. A jet consisting of a string of bright knots (G,F,E,D,C) of increasing brightness superposed on fainter extended emission links the compact feature H to a recessed and elongated feature (B) in the south lobe. C marks an abrupt change in the direction and collimation of the previously straight jet, but B qualifies as the hot spot by its surface brightness and compactness. A more diffuse feature (A) lies beyond the hot spot but its relationship to it is unclear at this resolution.

There is no sign of a counterjet within the diffuse emission north of feature H, opposite the straight segment of the jet, but there is a conspicuous knot (I) on the jet axis to the west of the north lobe. This knot is followed by a "hook" of emission (J) that curves toward the brightest part (K) of the extended ridge on the east side of the north lobe. I probably marks a major change in direction of a (hitherto undetectable) counterjet. J may thus be part of a deflected flow that leads ultimately into K. Feature K has a higher surface brightness than I at this resolution, but barely qualifies as a hot spot because its angular size is so large relative to the largest extent of the source. An MEM deconvolution (not shown) suggests that K contains finer-scale structure that is indeed brighter than I. We therefore adopt K as the hot spot in the counterjet lobe, and consider features I and J to be the brightest parts of a curved counterjet candidate. The MEM deconvolution also suggests that the north rim of this lobe is edge-brightened, and that filamentary features to the southwest of K connect the hot spot to the more extended lobe emission.

Figures 28(a) and 28(b) plot the polarization data on contours from Fig. 27. The degree of linear polarization of the jet increases from <13% at the first knot (G) to 23% by knot D and 20% at knot C. The **E** vectors are generally within 20° of being perpendicular to the jet axis. The highest degrees of polarization (40% to 50%) occur near the edges of both lobes, and reach 50% to 70% at the east edge of the north lobe. The **E** vectors are roughly perpendicular to the adjacent lobe boundaries.

Hintzen *et al.* (1991) found an over-density of images within 15″ of the quasar at V and I bands and concluded that 3C 336 is at the center of a rich cluster of galaxies. Bremer *et al.* (1992) detected [O II] line emission with a velocity shear around the quasar, and suggest that the quasar is at the center of a strong cooling flow.

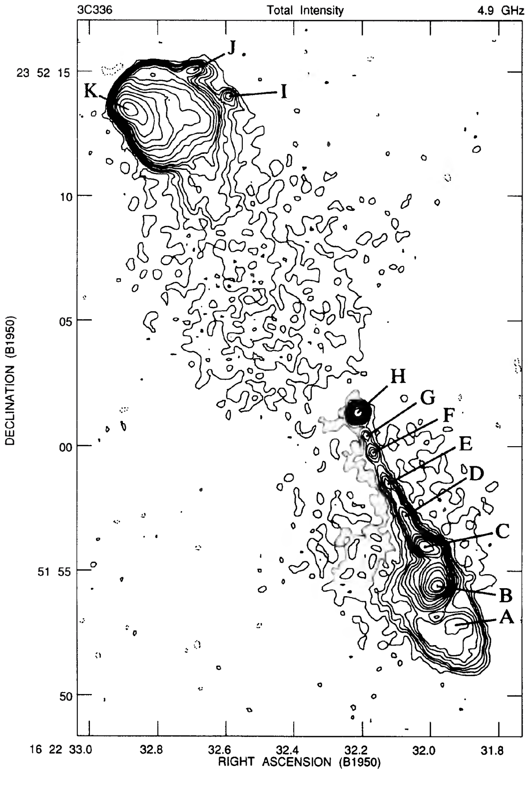

FIG. 27. Distribution of total intensity (Stokes I) over 3C 336 with 0.″34 (FWHM) resolution. H is the central feature and B is the jetted hot spot. K contains the counterjetted hot spot. I and J are part of the counterjet candidate. Contours are drawn at −1 (dotted), 1, 2, 3, 4, 6, 8, 10, 14, 20, 30, 50, 70, 120, 200, 400, 600, and 1000 times 50 μJy per CLEAN beam area. The peak intensity is 50.4 mJy per CLEAN beam area.

4.12 3C 351

Figure 29 shows the total intensity image at 3.″5 resolution from a brief VLA C-configuration observation kindly supplied by R. Barvainis. This shows that both lobes have diffuse extensions that are not well imaged in our higher-resolution data, which give details only of the brighter structures. These extensions can also be seen on the 1.45 GHz contour map of 3C 351 by Leahy *et al.* (1989).

Figure 30 shows the total intensity image at 1.″15 resolution from our B configuration data and the C configuration snapshot. The lobes are roughly symmetric in size but differ greatly in intensity and surface brightness. The structure is ~75″ ($230h^{-1}$ kpc) in extent. The northeast lobe includes a complex of bright features (J, L, M), previously detected by Kronberg *et al.* (1980), and several filaments. A large, faint "fan" of emission extends some 30″ to the west of this complex. The southwest lobe has a bright feature (A) on its outer edge. An abbreviated jet points from the partially resolved central complex toward the brightest feature (J) in the northeast lobe. A marginally detected curved emission arc, whose brightest features are at H and I, may continue this jet toward

1994AJ....108..766B

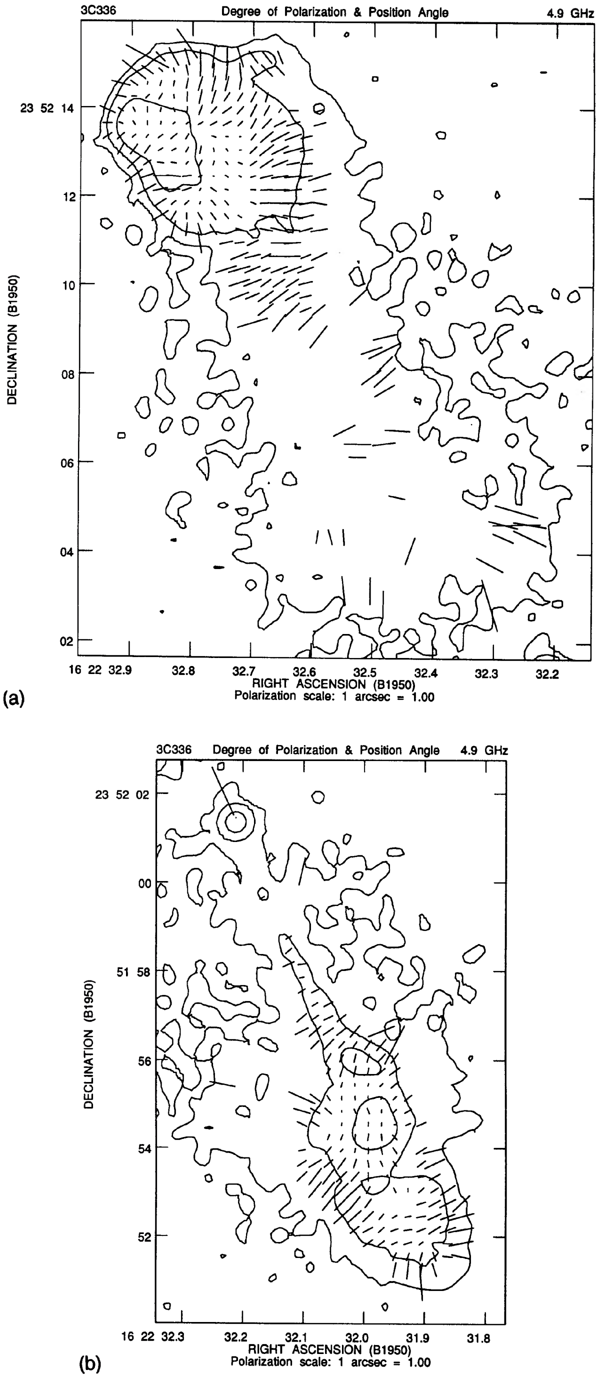

FIG. 28. Distribution of degree of linear polarization p and **E**-vector position angle χ over 3C 336 at 0.″34 resolution, superposed on contours from Fig. 27. A vector of length 1″ corresponds to $p=1$. (a): North lobe. (b): Central feature, jet, and south lobe.

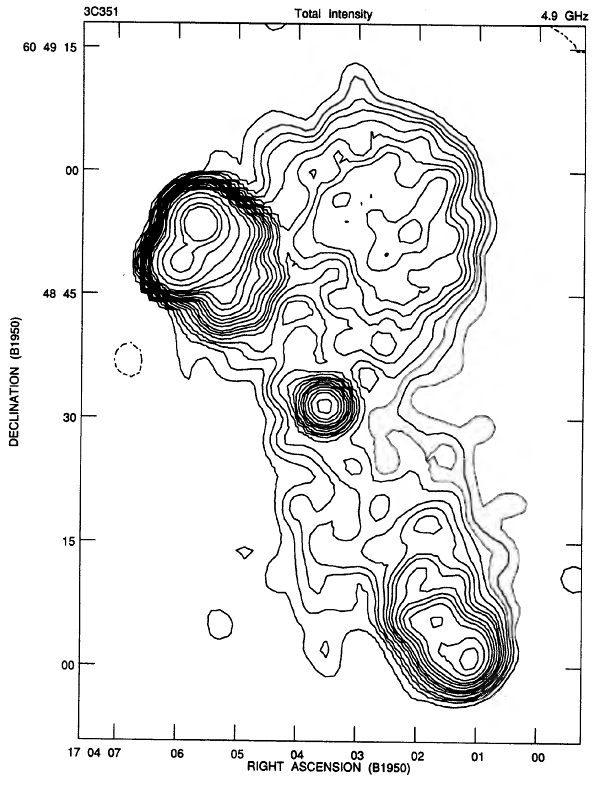

FIG. 29. Distribution of total intensity (Stokes I) over 3C 351 with 3.″5 (FWHM) resolution. Contours are drawn at −1 (dotted), 1, 2, 3, 4, 6, 8, 10, 12, 16, 20, 24, 30, 40, 50, 70, 100, 200, 400, 800, and 1200 times 200 μJy per CLEAN beam area. The peak intensity is 506 mJy per CLEAN beam area.

J. The brightness and compactness of J nominate it as the hot spot and it is likely, but we cannot be certain, that it also marks the termination, or deflection point, of the jet.

Figure 31(a) shows the polarization data from the B configuration data only at 1.″15 resolution on contours of total intensity for the northeast lobe and the jet only. The degree of polarization rises rapidly to 20%–25% away from the bright complex of emission to the north and west of the hot spot J. The **E** vectors are perpendicular to the lobe and fan boundaries near the edges of these structures, but are parallel to the axis of greatest elongation of the fan at its center. The degree of polarization reaches 50% to 65% toward the west edge of the fan. Figure 31(b) shows the polarization data for the southwest lobe at the same resolution. The basic pattern is similar to that in the northeast lobe except that there is apparently little perturbation at feature A, unlike the strong perturbation near J.

Figure 32 shows the total intensity of the central region and the bright complex in the northeast lobe at 0.″37 resolution from the A and B configuration data. The curved inner jet (features E, F, G) points toward the hot spot J at the lobe's extreme eastern edge. There is marginal evidence of a continuation of this curved jet through features H and I into J, but this emission is too faint to represent in the contour display. It is also confused by sidelobe responses to the hot spot, which limit our sensitivity in this region. A narrow filament K joins J to the bright resolved feature L on the lobe's north side. A network of filaments extends both south and west from this feature.

The extended central region of Fig. 30 is here resolved into two knots D and E, of almost equal brightness, with a further, weak knot C to the southwest. The available evidence strongly favors identifying the compact knot D as the

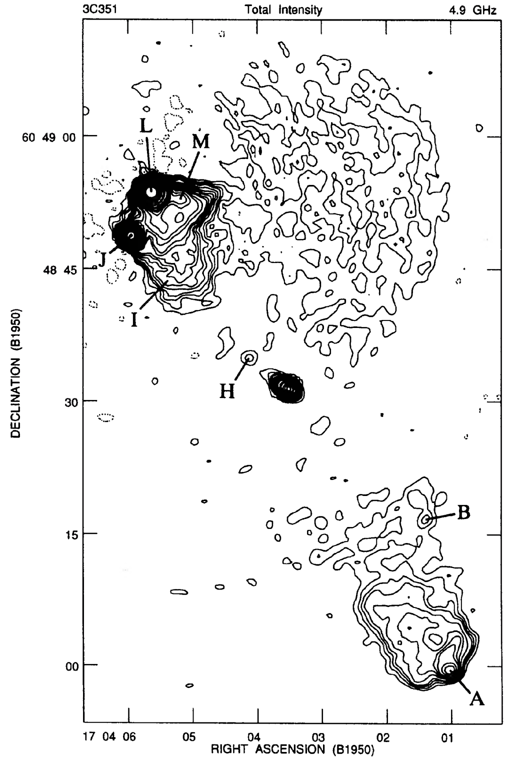

FIG. 30. Distribution of total intensity (Stokes I) over 3C 351 with $1''.15$ (FWHM) resolution. J is the jetted hot spot. H and I are part of the outer jet. Contours are drawn at -1 (dotted), 1, 2, 3, 4, 6, 8, 10, 12, 16, 20, 30, 40, 60, 80, 100, 120, 160, 200, 300, 400, 600, 800, 1000, 1200, and 1600 times 120 μJy per CLEAN beam area. The peak intensity is 318 mJy per CLEAN beam area.

true central feature, and knot E as a jet knot, while C may be part of a counterjet. First, the optical position for the nucleus of 3C 351 (see Table 5 below) is within $0^{\rm s}.022$ in α and $0''.15$ in δ of our radio position for D. The accuracy of the optical position (Clements 1983) is $\pm 0^{\rm s}.011$ in α and $0''.08$ in δ. Our radio error is $\sim 0''.2$ relative to the position given for 3C 345 in Table 3. The optical nucleus and D thus coincide to within the positional errors. Second, VLBI observations of 3C 351 by Hough *et al.* (19xx) rule out C as a candidate for the central feature—the VLBI correlated flux density at 8.4 GHz is $\sim$5 mJy. Third, analysis of the residual fringe rates for these VLBI data yields a position for the compact structure that is incompatible with our position for E but agrees well with that of D.

Note that feature B, which is near the projected axis of the main jet, might mark a point of deflection of a counterjet in the southwest lobe toward the brighter region A. Feature A itself has insufficient brightness contrast with the lobe to be termed a hot spot using our definition.

Figures 33(a) and 33(b) show the polarization data on contours from Fig. 32. Figure 33(a) covers the bright complex in the northeast lobe while Fig. 33(b) displays the region close to the central feature. In the lobe, most **E** vectors are perpendicular to the ridge lines of the filaments. In the extended jet, where the degree of polarization ranges from 11% to 31%, they are nearly perpendicular to the jet axis. The relatively low (7%) polarization at knot D (compared with the 13% polarization at knot E) supports our view that D contains the central feature. (The degrees of polarization at central features are usually much lower than those at jet knots—compare Tables 5 and 11 below.) At this resolution, which is too high to detect the "fan" emission, the highest degrees of polarization in the lobes are 35% to 50% on the

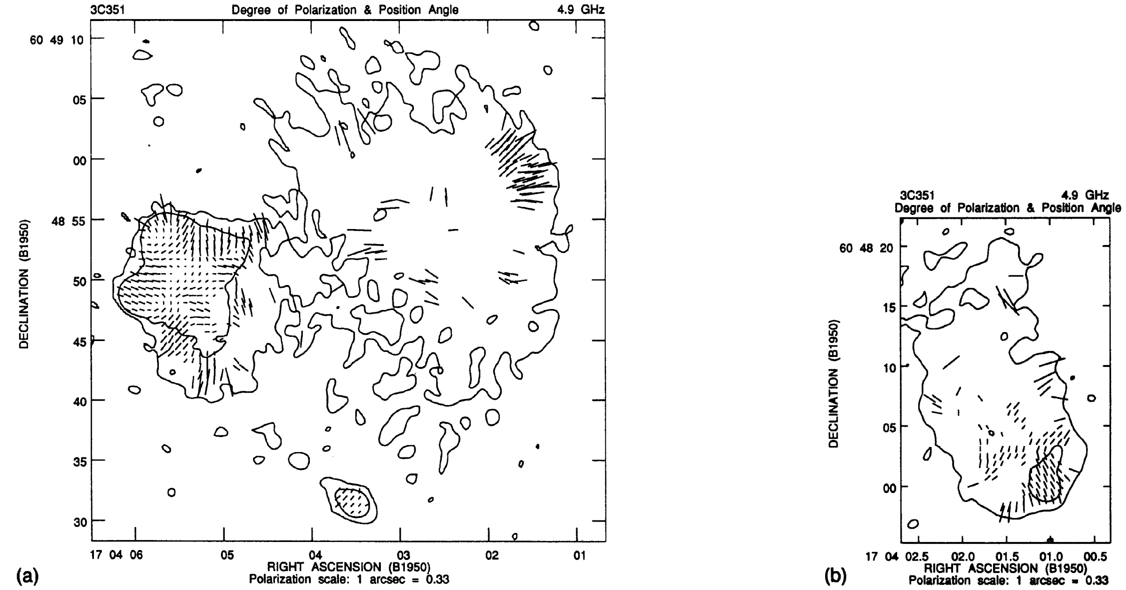

FIG. 31. Distribution of degree of linear polarization p and **E**-vector position angle χ over 3C 351 at $1''.15$ resolution, superposed on contours of total intensity. A vector of length $1''$ corresponds to $p=0.33$. (a): Northeast lobe, outer jet, and central feature. (b): Southwest lobe.

1994AJ....108..766B

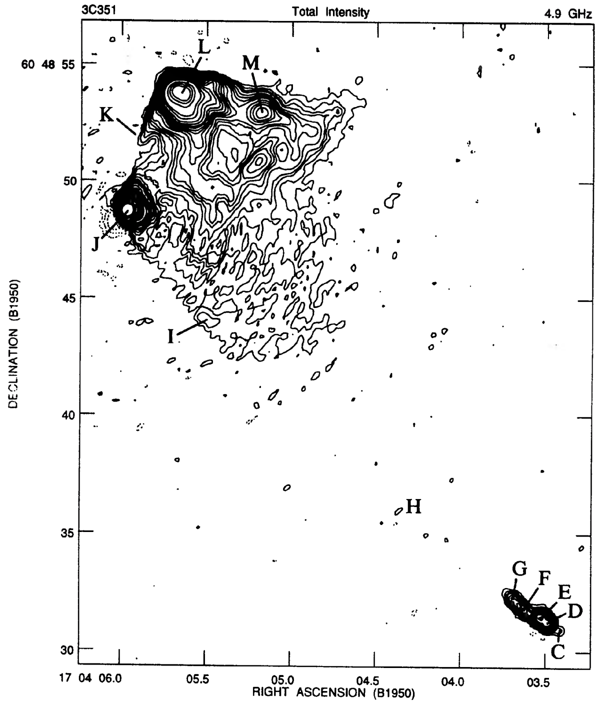

FIG. 32. Distribution of total intensity (Stokes *I*) over the central region, jet (E, F, G, and a faint ridge from H to the hot spot J through I), and northeast lobe of 3C 351 with 0."37 (FWHM) resolution. D contains the central feature and C is the counterjet candidate. Contours are drawn at −4, −2, and −1 (dotted), 1, 2, 3, 4, 6, 8, 10, 12, 16, 20, 24, 30, 40, 50, 70, 100, 150, 200, 400, 600, and 800 times 70 μJy per CLEAN beam area. The peak intensity is 159 mJy per CLEAN beam area.

north side of the northeast lobe, and north of feature A in the southwest lobe (not shown).

4.13 3C 432

Figure 34 shows the total intensity image at 0."37 resolution from the A and B configuration data. The lobes of this small (15″, $63h^{-1}$ kpc) source are roughly equally bright but are asymmetrically placed around the central feature C, the jetted lobe being further from this feature. The (previously undetected) jet contains an elongated knot (D) and possibly a weak ridge in the southeast lobe pointing toward the brightest part of the hot spot H. This ridge is not well resolved from other lobe substructure, so we cannot be certain that it is a continuation of the jet, but we include it in our integration of the jet flux density in Sec. *5.2.1.* The structure on the west edge of the southeast lobe (features E, F, G) resembles a barely resolved ring girdling the path of the jet. There is no sign of a counterjet. The hot spot in the northwest lobe is hard to identify uniquely at this resolution, but both an MEM deconvolution and Gaussian model-fitting imply that B is compact, bright, and exactly opposite the jet. We therefore believe that B marks the end of a counterjet in the northwest lobe, but emphasize that the MEM image was needed to confirm that it is a hot spot meeting all our criteria.

Figure 35 plots the polarization data on contours from Fig. 34. The most strongly polarized features (30% to 50%) are E, F, and G on the west side of the southeast lobe; the **E** vectors are perpendicular to the ridge line in and between these features. The jet and the southeast hot spot are unpolarized at this resolution. The northwest lobe is most highly polarized (40% to 50%) on the outer edge, the **E** vectors

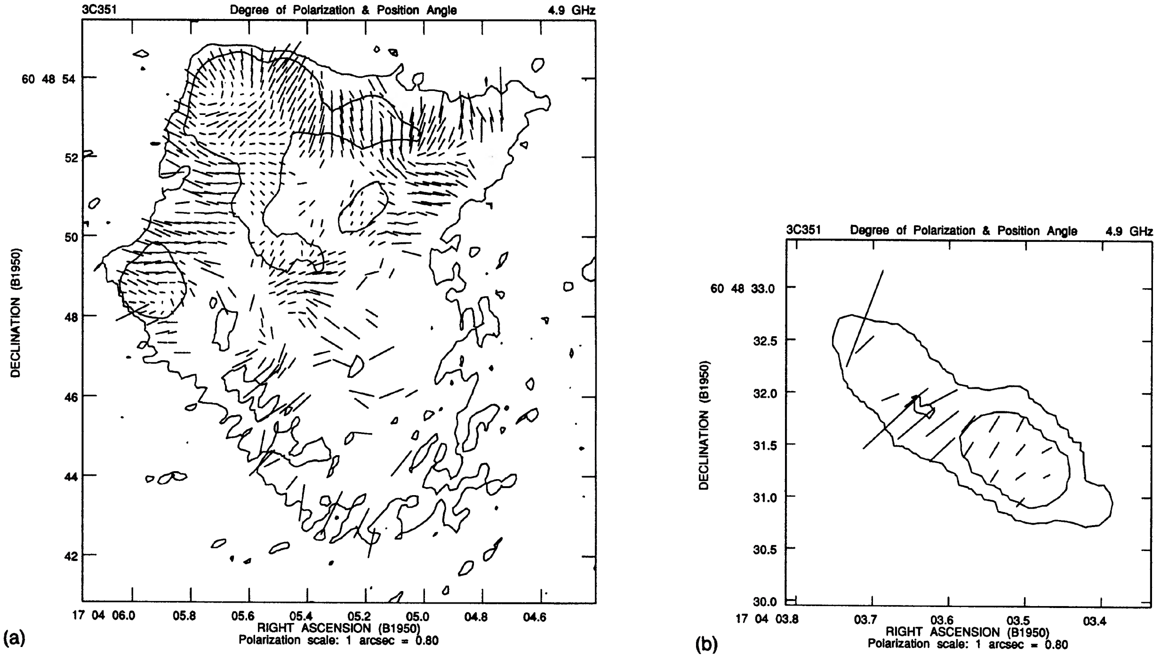

FIG. 33. Distribution of degree of linear polarization p and **E**-vector position angle χ over 3C 351 at 0."37 resolution, superposed on contours from Fig. 32. A vector of length 1″ corresponds to $p=0.8$. (a): Northeast lobe. (b): Inner jet and central feature.

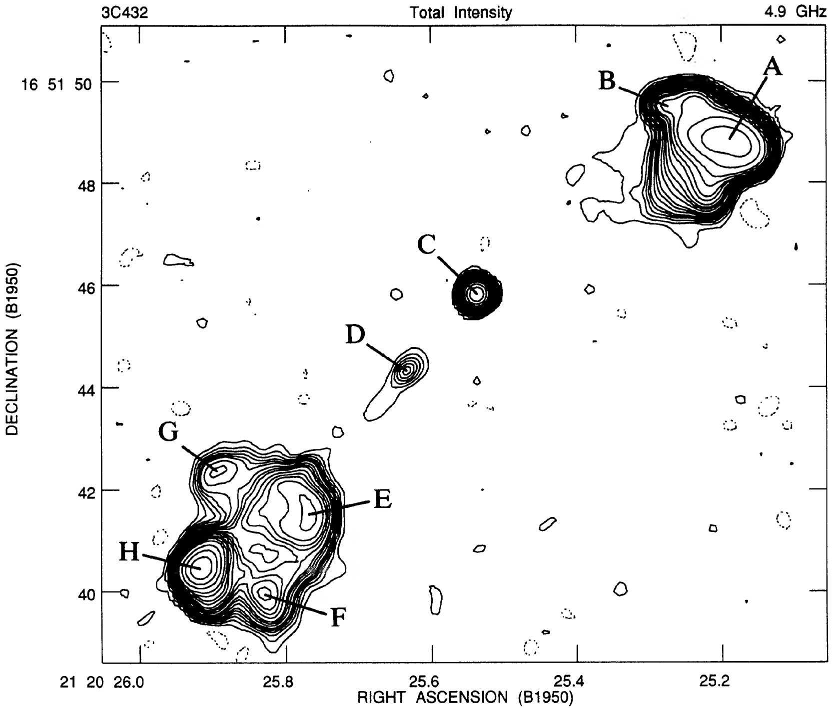

FIG. 34. Distribution of total intensity (Stokes I) over 3C 432 with 0.″37 (FWHM) resolution. C is the central feature. D and its weak extension to the southeast are the jet. H contains the jetted hot spot. There is no counterjet candidate, but B contains fine structure that we believe is the counterjetted hot spot (see text). Contours are drawn at −1 (dotted), 1, 2, 3, 4, 5, 6, 8, 10, 12, 16, 20, 24, 30, 40, 50, 70, 100, 200, 400, and 800 times 50 μJy per CLEAN beam area. The peak intensity is 73.1 mJy per CLEAN beam area.

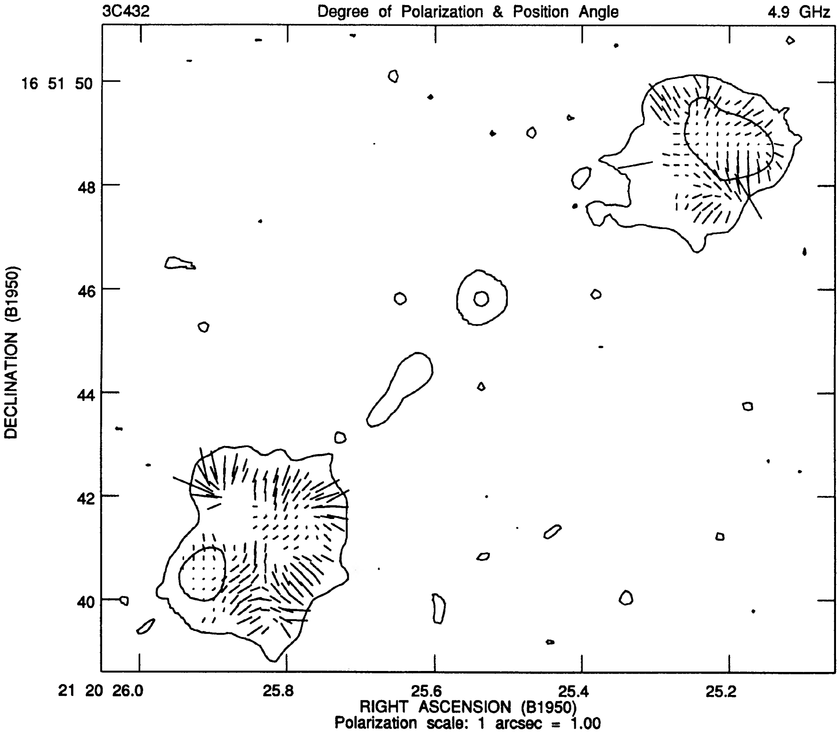

FIG. 35. Distribution of degree of linear polarization p and E-vector position angle χ over 3C 432 at 0.″37 resolution, superposed on contours from Fig. 34. A vector of length 1″ corresponds to $p=1$.

everywhere being perpendicular to the adjacent lobe boundary.

5. PHYSICAL PROPERTIES

In what follows, we combine the results from the above observations with those derived from the 4.9 GHz image of 3C 47 by Fernini *et al.* (1991), which we reprocessed through all the parameter-estimation steps described below. Figure 36 shows the total intensity image of 3C 47, together with our labeling for the major features described below (this labeling differs from that of Fernini *et al.*, to identify some features that they did not distinguish).

5.1 The Central Features

Table 5 lists observed parameters for the central features of the 13 quasars. For each source, we estimate the parameters of the part of the central feature that is unresolved to the VLA. The positions are therefore those of the peak intensities of these features. The quoted flux densities and size limits are the peak flux densities and the 1σ upper limits to the FWHM given by fitting two-dimensional Gaussian models and a background baseline level to a small region around the peak using the AIPS task IMFIT.

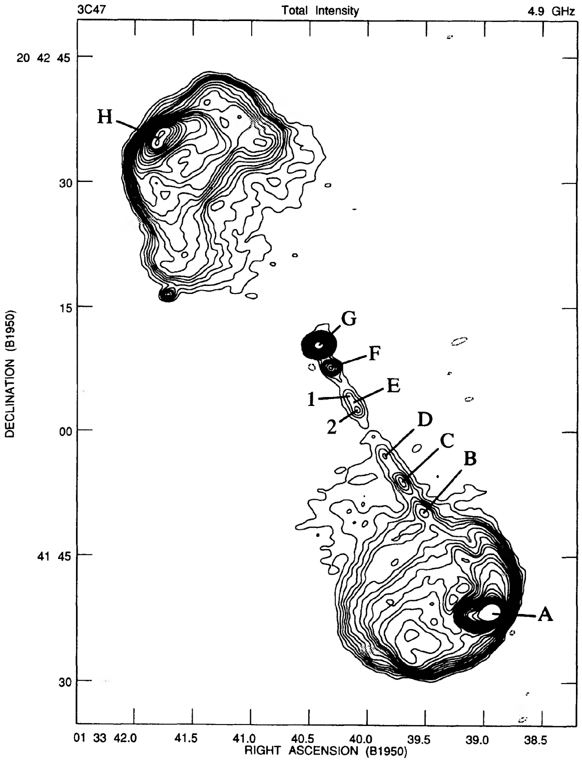

FIG. 36. Distribution of total intensity (Stokes I) over 3C 47 with 1.″45 by 1.″13 (FWHM) resolution (major axis in PA−81.°8), as imaged by Fernini *et al.* (1991). G is the central feature and A contains the jetted hot spot. There is no counterjet candidate, and H does not meet our compactness criterion for being a hot spot. Contours are drawn at −1 (dotted), 1, 2, 3, 4, 5, 6, 8, 10, 12, 14, 16, 20, 24, 30, 40, 50, 60, 80, 100, 120, 140, 160, 200, 240, 300, and 400 times 120 μJy per CLEAN beam area. The peak intensity is 196 mJy per CLEAN beam area.

For 3C 334, a single-component model gave unusually large residuals and an unusually high upper limit (0.″12) to the fitted FWHM. A two-component model in which E1 has the listed parameters and a second feature (E2) has FWHM 0.″27 along PA 141.°4 fits the data much better. We therefore treat E1 as the true central feature, and E2 as part of the extended jet emission. For the other sources, any evidence for such extended emission on scales of ~0.″2 near the central feature is marginal. The flux densities of the possible emission on this scale in the other sources are less than the uncertainties in the integrations over the well resolved jet emission.

Table 5 also lists the positions for the optical identifications of these quasars from the references cited by Laing *et al.* (1983), from Clements (1983), or from Argue & Kenworthy (1972), whichever has the smaller quoted error. The optical positions are generally accurate to better than 0.″5 in their reference frame and the radio positions to ~0.″2 relative to the calibrators listed in Table 3. As the positions of the radio central features and the optical objects usually agree within 1″ in both coordinates, we believe that the identifications are unambiguous. For 3C 208, the optical position given in the identification paper by Sandage & Wyndham (1965) disagrees with ours for the central radio feature by over 20″. Inspection of the Palomar Sky Survey shows that the object in the Sandage & Wyndham (1965) finding chart is within an arcsecond of our radio position, however. Thus Sandage & Wyndham's identification is correct even though its quoted optical position is erroneous.

Table 5 also lists the linear polarizations observed at the

TABLE 5. Parameters of central features.

Source		Position (B1950.0) h	m	s	°	′	″	Flux Density (mJy)	Fitted FWHM (″)	p χ
3C 9	r	00	17	49.908	15	24	16.23	4.9 ± 0.2	<0.104	<0.008
	o	00	17	49.944	15	24	16.21			
3C 47	r	01	33	40.422	20	42	10.40	73.6 ± 0.1	<0.086	0.001
	o	01	33	40.425	20	42	10.16			+64.6
3C 68.1	r	02	29	27.245	34	10	34.43	1.1 ± 0.1	<0.133	<0.04
	o	02	29	27.24	34	10	34.1			
3C175	r	07	10	15.387	11	51	24.47	23.5 ± 0.6	<0.077	<0.002
	o	07	10	15.379	11	51	23.95			
3C204	r	08	33	18.143	65	24	04.20	26.9 ± 0.2	<0.048	<0.003
	o	08	33	18.146	65	24	03.86			
3C208	r	08	50	22.686	14	04	17.36	51.0 ± 0.2	<0.030	0.007
	o	08	50	22.70	14	04	16.9			-19.1
3C215	r	09	03	44.126	16	58	16.00	16.4 ± 0.2	<0.047	<0.005
	o	09	03	44.14	16	58	16.1			
3C249.1	r	11	00	27.443	77	15	08.41	71 ± 0.7	<0.053	0.004
	o	11	00	27.439	77	15	08.57			-21.6
3C263	r	11	37	09.292	66	04	26.90	157 ± 0.5	<0.034	<0.001
	o	11	37	09.343	66	04	26.94			
3C334	r	16	18	07.287	17	43	30.32	111 ± 1.7	<0.07	0.004
	o	16	18	07.309	17	43	30.40			+74.5
3C336	r	16	22	32.212	23	52	01.35	20.4 ± 0.2	<0.038	0.003
	o	16	22	32.214	23	52	02.0			+27.9
3C351	r	17	04	03.488	60	48	31.23	6.5 ± 0.2	<0.077	0.072
	o	17	04	03.466	60	48	31.08			-58.7
3C432	r	21	20	25.537	16	51	45.82	7.5 ± 0.2	<0.062	<0.005
	o	21	20	25.532	16	51	46.4			

central features; the degrees of linear polarization are usually much lower than those of the jet knots (see Table 11 below).

In 6 of the 13 sources (3C 47: Vermeulen *et al.* 1993; 3C 204: Hough *et al.* 1993; 3C 208: Hough 1994; 3C 249.1: Hough 1986; 3C 263: Zensus *et al.* 1987; 3C 334; Hough *et al.* 1992), VLBI closure phase data determines the sidedness of the milliarcsecond-scale extended structure near the central feature. In all six cases, the fainter and more extended of two dominant VLBI components is on the same side of the brighter, more compact component as the large-scale jet. These VLBI observations have also measured outward proper motions on milliarcsecond scales with pattern speeds of $3.7h^{-1}c$ in 3C 47, $\leq h^{-1}c$ in 3C 204, $1.3h^{-1}c$ in 3C 263, and $1.6h^{-1}c$ in 3C 334.

5.2 The Jets and Counterjets

5.2.1 Integral properties

Table 6(a) lists the integrated flux densities for the jet and candidate counterjet emission in each source, together with the lengths, measured in arcseconds from the central feature, of the regions over which the integration was done. These integrated flux densities were estimated using the AIPS facility TVSTAT as follows. The pixel intensities in a curvilinear region of the image that contains the jetlike feature were summed and normalized to a flux density. We then subtracted an estimate of the extended lobe emission that is superposed on this curvilinear region of the image. This estimate was made as follows. We defined two similarly shaped comparison regions on each side of the jet region. The sizes and shapes of these comparison regions matched those for the jet integrations as closely as possible, but were adjusted to exclude readily identifiable confusing features such as bright knots or filaments. The pixel sums from the comparison regions were renormalized to the same number of pixels as those in the jet regions before being averaged and subtracted from the jet integration. This procedure corrects the integrated flux densities for the jets for an extended contribution with the average surface brightness of any adjacent large-scale structure. In lobes with much internal structure, or when jets run near lobe boundaries, discrepancies in the integrated flux densities of the two comparison regions may dominate the uncertainty in our estimate of the integrated flux density of a jet.

The integrated flux densities of counterjets are harder to assess accurately because counterjets are fainter than the jets and so are more confused by lobe emission. Their faintness exacerbates ambiguities about which features to include in the integration. We also emphasize that none of the counterjet *candidates* in our new images unambiguously meets all of our adopted criteria for jethood. For example, in 3C 334 both lobes are filamentary. The jet is easy to distinguish from confusing filaments by its brightness contrast, but the fainter counterjet candidate is not. It is a candidate because it lies along a plausible *path* for the other beam, not because of its prominence relative to the filaments. This method of identifying counterjet candidates is fallible, however, because we cannot predict their paths uniquely. These paths need not *a priori* have any particular symmetry relative to those of the jets if jets can be bent by local "weather" in galactic environments or if they can have relativistic pattern speeds. The path problem also affects the choice of an integration region when obtaining upper limits for undetected counterjets. For many sources in this sample, the uncertainties in the counterjet integrations stemming from ambiguities over what areas of the image to include as counterjet candidates are as large as, or larger than, the uncertainties in the background corrections. The following cases are particularly troublesome:

3C 9: a possible continuation of the counterjet candidate through a ridge in its lobe, excluded in Table 6, could increase the counterjet flux density from 0.36 to 6.2 mJy. The ridge is not sufficiently distinct to be considered part of the counterjet on the present evidence, however.

3C 47: the combination of large-scale structure and lack of a hot spot in the counterjet lobe make the appropriate counterjet integration path and the lobe emission correction uncertain. The axis of the straight inner segment of the jet points toward a curved ridge of emission leading into feature H, but this ridge has too little brightness contrast relative to the rest of the lobe to be considered a counterjet candidate. Our upper limit for the counterjet is conservative and is determined entirely by scatter in the possible corrections for the lobe emission, rather than by suspicion of an explicit counterjet feature at this flux density level.

3C 208: the resolved feature H has been interpreted as confusing lobe emission, not as a broad counterjet-related feature. In setting an upper limit to the integrated counterjet emission, we use an integration region whose width equals that of the jet, traversing the ridge of feature H before bending northward toward the hot spot J. The integrations on the adjacent comparison paths disagree by almost 5 mJy because they contain different contributions from feature H and other background in the lobe. Use of the southern comparison region alone suggests that there is no excess flux density attributable to a counterjet, but use of the northern path pro-

TABLE 6. Integrated flux densities of jets and counterjet candidates.

(a) whole path

Source	Jet (mJy)	Length (")	Counterjet (mJy)	Length (")
3C 9	331 ± 3	8.0	0.36 ± 0.02	1.5
3C 47	23 ± 5	36.5	<4.2	29.0
3C 68.1	116 ± 6	21.0	2.52 ± 0.06	11.0
3C175	25 ± 3	27.5	<0.32	19.0
3C204	7.4 ± 0.5	12.1	<0.19	14.0
3C208	26 ± 3	4.8	<5.1	4.8
3C215	27 ± 2	9.7	4.2 ± 2.1	21.0
3C249.1	51 ± 4	7.0	1.0 ± 0.2	3.7
3C263	27 ± 6	15.6	<0.68	24.1
3C334	52 ± 1	17.0	3.3 ± 0.5	26.0
3C336	66 ± 5	6.9	3.3 ± 0.2	15.4
3C351	14 ± 3	24.3	0.18 ± 0.03	0.7
3C432	4.4 ± 3.3	6.8	<0.12	4.7

(b) straight jet path

Source	Jet (mJy)	Length (")	Counterjet (mJy)	Ratio
3C 9	1.18 ± 0.04	1.5	0.36 ± 0.02	3.3
3C 47	6.2 ± 1.5	19.6	<1.7	>3.7
3C 68.1	2.1 ± 0.1	13.0	2.52 ± 0.06	(1.2)
3C175	2.4 ± 0.1	6.7	<0.20	>12
3C204	5.1 ± 0.1	8.4	<0.19	>27
3C208	9.7 ± 0.2	4.1	<1.88	>5.2
3C215	2.9 ± 0.1	3.1	0.11 ± 0.04	26
3C249.1	12.4 ± 0.5	3.6	1.0 ± 0.2	12
3C263	7.5 ± 0.9	8.7	<0.22	>34
3C334	38.5 ± 0.7	12.1	<0.22	>175
3C336	3.9 ± 0.1	3.7	<0.41	>9.5
3C351	9.4 ± 0.1	2.7	0.18 ± 0.03	52
3C432	0.47 ± 0.05	2.2	<0.1	>4.7

duces a formal excess of 5.1 mJy on the counterjet path. Because we see no narrow feature within H that properly qualifies as a counterjet candidate, we take the 5.1 mJy value as a conservative upper limit.

3C 215: the low brightness contrast of a long counterjet candidate against an extended lobe with other weak internal structure leads to a large uncertainty in the background correction.

3C 249.1: only the initial narrow ridge-like feature is included in our counterjet integration. Each of the extended hook-like features B and C near the putative counterjet path contains an integrated flux density of 2.9 mJy. If both these less collimated features were also associated with the counterjet candidate, its integrated flux density could be increased from 0.95 to 6.75 mJy.

3C 334: we did not include knot C, which does not qualify as a hot spot by our definition but which lies on the projected counterjet path and is the most promising hot spot candidate in the counterjet lobe. Adding C to the counterjet integration would increase the estimate from 3.3 to 6.55 mJy.

3C 336: we included knots I and J in the counterjet integration, because there is a hot spot (K) elsewhere in the lobe and because J can plausibly be interpreted as part of a counterjet that deflects into K after brightening at I. (This case is the opposite of 3C 334, where knot C was excluded from the integration because it is the most promising hot spot candidate in the counterjetted lobe.) If higher-resolution data should show that knot I is the hot spot, there would be no counterjet candidate in this source.

Ambiguities about the paths of the counterjets contribute significantly to the uncertainties in the integrated flux densities in Table 6(a). Although none of the jets is perfectly straight, many have long, relatively straight inner sections. The counterjet paths are perhaps least ambiguous opposite these inner, straighter jet segments. Regions where jets and counterjets bend may also be the sites of particularly strong interactions with their environments. The straighter segments are where it is least likely that jet brightnesses are dominated by changes in the internal velocity field induced by such interactions. We therefore determined a second set of flux densities for the jets and counterjet candidates, using only the straighter regions of the jets and the corresponding rectangular areas of sky on the counterjet side.

These "straight jet" integrations were made from images that were rotated and regridded to make the initial segments of the jets lie along rows or columns of the data (using the AIPS task LGEOM). The jet flux density was integrated over a rectangular region within which (a) the ridge line of the jet deviates from the centerline of the box by less than a jet radius (or by less than the synthesized beam HWHM if the jet was unresolved) and (b) there is no obvious confusion by large gradients in the lobe emission. This integration was corrected for lobe emission by subtracting the mean of the integrations in the two identically sized rectangles alongside the jet. We also integrated over the geometrically equivalent rectangles on the counterjet side, to estimate or set limits to any counterjet emission opposite these straight jet segments. If the integration in the rectangle opposite the straight jet segment exceeded those in both comparison regions (i.e., if there is evidence for a counterjet candidate opposite the straight jet), the lobe correction was made as on the jet side—by subtracting the average of the two adjacent integrations. Otherwise, an upper limit was derived by subtracting the lower of the adjacent integrations.

Table 6(b) lists the "straight" jet and counterjet flux density integrations obtained in this way, together with the angular length of the path from the central feature to the outer boundaries of the integration regions, and the resulting jet/counterjet intensity ratio. Note that for 3C 68.1, the integrated flux density of the counterjet candidate exceeds that of the jet in this restricted region, so we list the ratio in parentheses.

The counterjet lobes in 3C 47 and 3C 175 contain curved "hooks" of emission that link their hot spot candidates to the line projected into the lobe from the axis of the straight segment of the jet. If these emission hooks could be better distinguished from other lobe features by higher-resolution observations, they might also be evidence for counterjets that brighten as they bend away from the axis of the straight jet, as in 3C 334 and 3C 336.

5.2.2 *Deflections and bending*

Table 7(a) quantifies the apparent deflections of each jet in several ways, reflecting different scales of jet bending and alternative deflection mechanisms. Figure 37 illustrates the six deflection measures that we have considered.

The angle η_1 is the difference between the initial and final directions of the jet, i.e., between the position angles of the jet when closest to the central feature and when closest to the terminal hot spot. The position angle can itself be measured in two ways.

The first, henceforth η_{1c}, uses the *central* feature as a reference. In this approach, the initial position angle is that of the line joining the central feature to the first jet knot and

TABLE 7. Jet deflection angles.

(a) Individual Sources

Source	Was A CounterJet Candidate Detected?	Referred to Central Feature η_1 (°)	η_2 (°)	η_3 (°)	Referred to Polynomial Tangent η_1 (°)	η_2 (°)	η_3 (°)
3C208	No	1.6	7.5	7.4	30.9	43.1	35.5
3C263	No	2.4	3.0	1.5	23.4	27.7	19.1
3C432	No	2.8	3.7	3.7	10.6	10.6	7.4
3C 47	No	4.4	4.4	2.0	4.2	8.4	8.4
3C204	No	6.1	6.1	2.3	34.7	34.7	15.8
3C175	No	6.7	7.2	2.4	1.2	31.4	23.7
3C336	Yes	6.9	9.1	3.0	4.4	24.7	18.2
3C351	Yes	7.0	13.6	6.6	8.7	32.4	15.9
3C 68.1	Yes	7.4	7.4	3.0	18.4	97.4	85.8
3C249.1	Yes	7.7	10.5	4.2	16.9	25.5	15.0
3C334	Yes	25.4	25.4	10.2	36.0	40.5	12.2
3C215	Yes	28.7	33.4	20.3	55.0	74.1	48.9
3C 9	Yes	31.2	31.2	9.6	87.3	87.3	37.5

(b) Sample Means

Mean of	Was A CounterJet Candidate Detected?	Referred to Central Feature η_1 (°)	η_2 (°)	η_3 (°)	Referred to Polynomial Tangent η_1 (°)	η_2 (°)	η_3 (°)
6	No	4.0	5.3	3.2	17.5	26.0	18.3
7	Yes	16.3	18.7	8.1	32.4	54.6	33.4

Notes to TABLE 7

η_1: Initial (nearest central feature) minus final (nearest hot spot)
η_2: Largest global difference along jet
η_3: Largest local difference along jet

1994AJ....108..766B

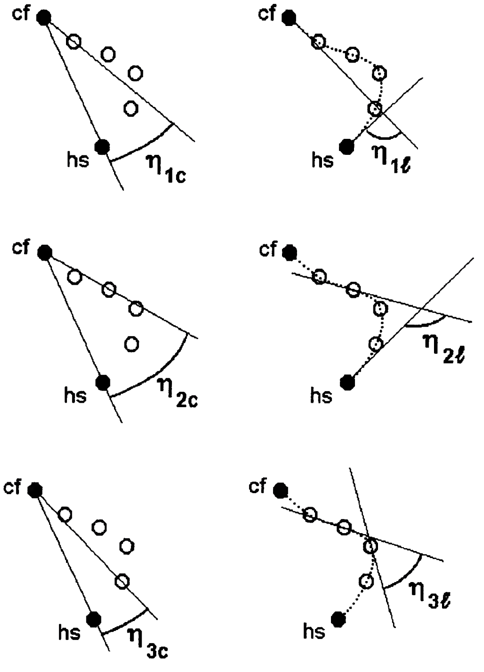

FIG. 37. The six measures of jet deflection introduced in Sec. *5.2.2* and Table 7. The filled circles labeled cf and hs denote the peaks of the central feature and jetted hot spot, respectively. The open circles denote the peaks of jet knots. The left column shows the centrally referenced deflection measures. The right column shows the deflection measures obtained from the tangents to the jets, as estimated by fitting a polynomial (dashed curve) to the positions of these features.

the final position angle is that of the line joining the central feature to the terminal hot spot. (This method can be thought of as measuring the "swing" of the central engine between the earliest and latest epochs, in a model of the jet trajectory based on purely ballistic outflow from an engine whose orientation varies.)

The second, henceforth η_{1l}, uses the *local* position angles of the tangents to the jet direction, as estimated by fitting a polynomial curve to the positions of the central feature, jet knots and hot spot. The order of the polynomial was increased until a minimum was reached in the reduced χ^2 of the fit. In this approach, the initial position angle is close to that used for η_{1c} but the final position angle is referred to the outermost segment of the jet rather than to the central feature. (This method can be thought of as measuring the changes in direction of the jet in a flow model in which the streamlines lie along the fitted polynomial.)

The angle η_2 is the largest difference in position angles between any two vectors characterizing the orientation of the jet. In a purely ballistic interpretation, η_{2c} measures the largest possible excursion that could be ascribed to the central engine on the time scale of the jet. In a streamline interpretation, η_{2l} measures the largest difference in flow direction between any two positions along the jet.

The angle η_3 measures the largest difference in position angles between any pair of adjacent knots in the jet, i.e., the largest local deflection anywhere along the jet path. η_{3c} is the largest difference in position angles, measured with reference to the central feature, between any adjacent knots in the jet (including the terminal hot spot). η_{3l} is the largest change in jet tangent directions between any adjacent knots in the jet.

Table 7(a) lists our estimates of all 6 angles for the jets in these 13 quasars, in order of increasing η_{1c}. We cannot estimate these angles reliably for the counterjets—the counterjet candidates are marginal detections, their inferred paths depend much more critically on interpretation of ambiguous features, and there are sometimes no hot spots (by our criteria) in the counterjetted lobes.

Note that although we have just characterized the measurement of these angles in terms of two simple models of jet kinematics, we do not wish to restrict ourselves to just these models. For example, the centrally referenced angles η_c could also measure jet deflection appropriately for models with outflow over a cone of directions within which some features appear brighter than others. In such models, a polynomial fitted to the jet ridge-line need not trace a flow line, and η_{1c} may estimate the (projected) opening angle of the cone. To summarize, the "locally referenced" estimates η_l may characterize the jet deflections well if the jet ridge-line traces a streamline, while the "centrally referenced" estimates η_c could characterize them better if it does not.

Table 7(a) is ordered by the "initial minus final" bending measure η_{1c} to emphasize a broad correlation within this sample between jet deflection and the detection of counterjet candidates: all sources with no counterjet candidates have $\eta_{1c}\leqslant 6\overset{\circ}{.}8$, whereas those with counterjet candidates have $\eta_{1c}>6\overset{\circ}{.}8$. This "perfect" ordering of counterjet candidate detection by η_{1c} must be coincidental, however: six jets, both with and without counterjet candidates, have $6°<\eta_{1c}<8°$. The "largest deflection" measure η_{2c} predicts counterjet candidate detection almost as well as η_{1c}.

Table 7(b) shows a more robust result—the average values of *all six* angles η for the sources without counterjet candidates are well below the corresponding averages for the sources with counterjet candidates. This connection between apparent jet bending and the presence of counterjet candidates evidently depends little on details of how the bending is quantified. We explore its implications in Secs. 6 and 7 below.

5.2.3 Internal structure

We derived approximate parameters for the most readily distinguishable discrete knots in the jets and counterjet candidates by fitting models to them using the AIPS task IMFIT. Well isolated knots were fitted by two-dimensional elliptical Gaussian models, superposed on a second-order background to account for underlying extended emission. Knots that are partially blended or confused by steep gradients in the underlying emission were modeled by multiple Gaussian components, some of which represented the background gradients. Table 8 gives the results of this model-fitting.

Both $\Delta\psi_{\rm ck}$ and $\Delta\psi_{\rm jet}$ measure the *inclination* of the jet knot to a reference direction. The distributions of $\Delta\psi_{\rm ck}$ and $\Delta\psi_{\rm jet}$ both peak strongly near 0°—87% of the jet knots have $\Delta\psi_{\rm jet}<20°$ and 84% have $\Delta\psi_{\rm ck}<20°$, although the inclinations $\Delta\psi_{\rm ck}$ reach 69°. Because most of the features that we

TABLE 8. Parameters of knots in jets and counterjet candidates.

Source	Knot ID	Θ (")	S_{int} (mJy)	LAS (")	SAS (")	ψ (°)	ψ_{ck} (°)	ψ_{jet} (°)	$\Delta\psi_{ck}$ (°)	$\Delta\psi_{jet}$ (°)	Φ/Θ
3C 9	C	1.03	0.36	0.44	0.23	160	161		1		0.22
3C 9	E	0.99	1.16	0.45	<0.17	158	156	153	2	5	<0.17
3C 9	F	2.78	22.9	0.31	0.24	167	150	134	17	33	0.088
3C 9	G	3.57	34.9	0.67	0.26	133	143	133	10	0	0.074
3C 9	H	5.42	170.	0.47	0.24	146	141	133	5	13	0.044
3C 9	I	6.47	71.5	0.51	0.28	133	139	118	6	15	0.043
3C 9	J	7.26	22.0	0.86	0.36	112	134	81	22	31	0.053
3C 47	F	3.06	1.96	0.91	0.54	43	29	31	14	12	0.18
3C 47	E1	7.96	1.79	3.89	0.82	30	31	30	1	0	0.10
3C 47	E2	9.23	0.16	<0.89	<0.89		31	31			
3C 47	D	15.57	0.92	2.58	0.37	27	31	33	4	6	0.023
3C 47	C	19.31	1.59	2.41	0.49	34	31	35	3	1	0.025
3C 47	B	23.73	2.45	1.97	1.04	37	32	37	5	0	0.044
3C 68.1	F2	9.63	1.26	0.69	0.42	154	175		21		0.045
3C 68.1	F1	9.35	1.26	0.28	0.20	12	177		15		0.021
3C 68.1	D	8.68	2.09	2.66	0.55	171	177	176	6	5	0.064
3C 68.1	C	20.75	95.5	0.58	0.37	103	172	80	69	23	0.026
3C175	L	2.22	1.44	0.67	0.08	58	57	57	1	1	0.038
3C175	K	5.21	1.23	2.20	0.22	57	57	57	0	0	0.042
3C175	J	8.46	0.72	1.09	0.23	64	57	58	7	6	0.028
3C175	I	11.92	0.63	0.79	0.27	62	58	58	4	4	0.023
3C175	F	21.72	1.13	1.05	0.45	33	54	34	21	1	0.022
3C175	E	22.68	1.12	1.22	0.35	37	53	29	16	8	0.016
3C175	D	25.23	3.14	0.59	0.29	62	51	37	11	25	0.012
3C204	I	1.63	1.29	0.20	<0.16	93	93	94	0	1	<0.098
3C204	H	3.79	0.70	0.49	0.09	102	94	97	8	5	0.024
3C204	G	5.83	0.66	0.42	<0.11	97	96	97	1	0	<0.019
3C204	F	7.85	0.56	0.55	0.02	98	95	96	3	2	0.003
3C204	E	11.64	2.04	0.88	0.24	118	97	111	21	7	0.022
3C208	F	0.77	1.59	0.33	0.06	75	77	81	2	6	0.074
3C208	E	1.72	1.23	0.56	0.22	85	81	87	4	2	0.13
3C208	D	2.72	1.73	0.60	0.12	82	83	86	1	4	0.042
3C215	D	3.60	6.89	0.33	0.08	117	78	110	39	7	0.028
3C215	E	5.84	1.23	0.46	0.32	93	98	123	5	30	0.055
3C215	F	8.25	6.31	0.55	0.33	131	103	120	28	11	0.043
3C249.1	E	1.01	8.82	0.35	0.13	114	100	103	14	11	0.13
3C249.1	I	5.19	6.72	0.43	0.21	81	99	85	18	4	0.042
3C249.1	J	5.97	9.19	0.55	0.17	84	96	80	12	4	0.029
3C263	D	1.90	1.75	0.65	0.12	112	109	108	3	4	0.065
3C263	E	4.42	3.22	2.68	0.14	109	109	109	0	0	0.033
3C263	F	6.95	1.73	1.07	0.10	109	109	110	0	1	0.015
3C263	G	9.35	1.17	1.15	0.17	109	109	108	0	1	0.018
3C263	H	11.81	1.88	1.69	0.15	110	109	109	1	1	0.012
3C263	J	15.38	16.8	0.39	0.38	102	110	128	8	26	0.024
3C334	D	19.73	0.88	0.81	0.44	158	140		18		0.023
3C334	E2	0.03	25.3	0.27	0.09	141	158	151	17	10	2.8
3C334	F	1.30	2.02	1.64	0.27	148	147	144	1	4	0.21
3C334	G1	2.39	0.41	0.16	<0.16	132	148	141	16	9	<0.07
3C334	G2	2.87	1.42	0.50	0.10	145	143	139	2	6	0.035
3C334	H	3.76	0.98	0.92	0.37	127	142	138	15	11	0.10
3C334	I	6.29	2.23	1.34	0.42	146	142	141	4	5	0.067
3C334	J	8.26	2.72	1.49	0.44	144	141	142	3	2	0.053
3C334	K1	10.00	3.01	3.28	0.48	136	141	142	5	6	0.048
3C334	K2	11.63	2.78	2.22	0.32	137	142	139	5	2	0.027
3C334	M	13.70	4.69	2.04	0.30	131	141	127	10	4	0.022
3C334	N1	13.96	1.05	1.08	0.30	107	139	122	32	15	0.025
3C334	N2	15.17	3.04	1.27	0.27	91	138	110	47	19	0.025
3C336	J	15.22	1.74	0.63	0.15	99	26		73		0.041
3C336	I	13.69	0.57	0.25	0.17	46	22		24		0.013
3C336	G	0.97	0.42	0.34	0.16	52	18	22	34	30	0.19
3C336	F	1.72	0.72	0.45	0.10	26	21	26	5	0	0.058
3C336	E	3.12	1.59	1.07	0.14	33	23	25	10	8	0.046
3C336	D	4.91	6.70	1.82	0.20	29	25	35	4	6	0.041
3C336	C	6.03	38.3	0.51	0.15	62	27	28	35	34	0.031
3C351	C	0.61	0.18	<0.43	<0.26		60				
3C351	E	0.40	8.27	0.10	0.06	59	53	60	6	1	0.15
3C351	F	1.21	2.14	0.67	0.15	50	60	55	10	5	0.12
3C351	G	1.85	0.76	0.29	0.25	48	54	36	6	12	0.14
3C432	D1	2.02	0.49	0.40	<0.40	135	138	137	3	2	<0.20
3C432	D2	2.79	0.18	0.60	<0.60	136	138	136	2	0	<0.22

Notes to TABLE 8

Knot ID: from Figures in Sec.4, fits with two Gaussian components carry additional designations 1 and 2
Θ: angular distance between peak of knot and central feature
S_{int}: integrated flux density of knot
LAS,SAS: major and minor axes of fitted elliptical Gaussian component
ψ: position angle of major axis of fitted component
ψ_{ck}: position angle of line from peak of knot to peak of central feature
ψ_{jet}: local position angle of tangent to jet (from polynomial fit)
$\Delta\psi_{ck}$: angle between fitted major axis and line to central feature
$\Delta\psi_{jet}$: angle between fitted major axis and local tangent to jet
Φ: FWHM of knot transverse to the line from it to the central feature

identify as jet knots align so well with the local jet axis, the distinction between a knot and underlying more continuous emission may be somewhat subjective, especially with limited angular resolution transverse to the jets. We can, however, legitimately recognize a class of strongly *misaligned* knots whose $\Delta\psi_{jet}$ and $\Delta\psi_{ck}$ values differ significantly from 0°. We return to the properties of these knots in Sec. *5.2.7*.

5.2.4 Spreading

Table 8 shows that we detect jet spreading in several sources: the transverse knot widths Φ tend to grow with angular distance Θ from the central feature. The knot widths Φ generally do not grow in linear proportion to Θ, however, as they would in a freely expanding jet. Instead, Φ/Θ is often larger at small Θ. This is a pattern exhibited by many well resolved jets in radio galaxies (e.g., Willis *et al.* 1981; Fanti *et al.* 1982; Perley *et al.* 1984; Killeen *et al.* 1986; Morganti *et al.* 1987; Bridle *et al.* 1991; Clarke *et al.* 1992)—an initial rapid spreading, followed by slower spreading, or recollimation.

We analyzed the collimation properties of the long, relatively straight jets in 3C 175, 3C 204, 3C 263, and 3C 334 in more detail. We used the SLICE facility in AIPS to make many profiles transverse to the average jet axes at one-beamwidth intervals along the straighter segments of these jets. These transverse profiles were analyzed using H. S. Liszt's DRAWSPEC profile analysis software to remove polynomial baselines and fit one-dimensional Gaussian models. This procedure allows us to examine the spreading of the fainter emission between the knots in addition to the local peaks that dominate the two-dimensional model-fitting. It is also free of the (at times unwarranted) assumption that the *longitudinal* brightness variations along the jets can be described as superposed Gaussian features. Figures 38 to 41 show spreading plots for these jets derived from both the one-dimensional profile-fitting (filled circles) and the two-dimensional model fits (open circles for measurements, open triangles for upper limits). The two approaches usually agree to within the error in the profile fitting. Where they disagree, the profile fitting tends to estimate larger widths than the knot modeling. For some cases, especially 3C 175, there is evidence that the fainter inter-knot emission is broader than the bright knots.

Figure 42 plots the *average* spreading rates $(\langle\Phi/\Theta\rangle)$ for these 3CR quasar jets against total lobe power at 1465 MHz, superimposed on an ensemble of such spreading data compiled by Bridle (1995a) for jets that are $>10h^{-1}$ kpc in projected length. The spreading rates from the present study are themselves uncorrelated with lobe power, but they strikingly confirm the absence of spreading rates >0.1 among powerful radio galaxies and quasars previously noted in a much smaller sample by Bridle (1984). As Fig. 42 shows data only for jets whose spreading rates have been directly determined, it may represent only the upper envelope of the true spreading rate distribution. Despite this selection, it is clear that spreading rates >0.10 on $>10h^{-1}$ kpc scales are common in sources with $P_{\rm lobe}^{1.5}<10^{25}h^{-2}$ W Hz^{-1} but rare in sources with $P_{\rm lobe}^{1.5}>10^{26}h^{-2}$ W Hz^{-1}.

Figures 39 to 41 give direct evidence for faster-than-average spreading in the jets in 3C 204, 3C 263, and 3C 334 when they are closest to the nucleus—none of these spreading plots extrapolates to the origin. (The transverse knot widths in the $\sim 8h^{-1}$ kpc inner jet in 3C 351, which is too short to be shown in Fig. 42, are also consistent with a high initial spreading rate of 0.13 for this jet segment, whereas the marginally detected outer jet appears to be better collimated than this.) The low average spreading rate of the large-scale jets in these powerful sources therefore seems to be a property that is imposed by interactions on many-kiloparsec scales, not by "initial conditions" near the central objects. The spreading rates and internal morphologies of these quasar jets should therefore be examined directly on subarcsecond scales, to determine the scale of the recollimation and to explore the detailed structures of the jets in the recollimation

1994AJ....108..766B

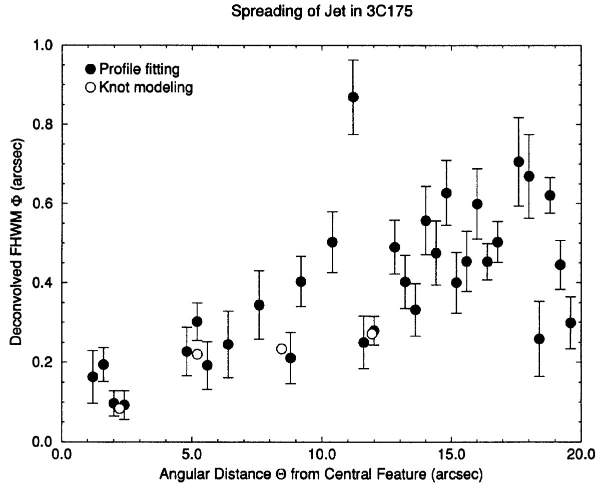

FIG. 38. The deconvolved FWHM Φ transverse to the jet in 3C 175 plotted against angular distance Θ from the central feature. Filled circles show one-dimensional Gaussian fits to the transverse intensity profiles, with their 1σ errors. Open circles show the results of two-dimensional Gaussian modeling of knots.

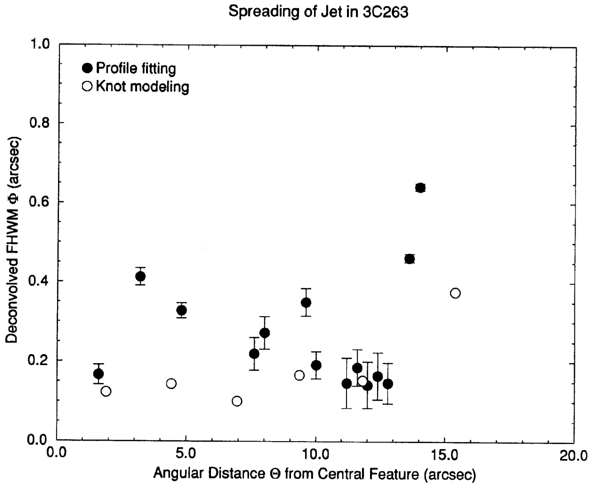

FIG. 40. The deconvolved FWHM Φ transverse to the jet in 3C 263 plotted against angular distance Θ from the central feature. Filled circles show one-dimensional Gaussian fits to the transverse intensity profiles, with their 1σ errors. Open circles show the results of two-dimensional Gaussian modeling of knots.

regime. The jets in 3C 204 and 3C 263 also show evidence of "flaring" (accelerated spreading) as they approach the hot spots.

5.2.5 Trains of knots

It has been suggested (Rees 1978; Sanders 1983; Smarr *et al.* 1984; Hardee & Norman 1989) that quasiperiodic trains of knots in jets arise from shock cell patterns in confined flows. The jets in 3C 175, 3C 204, 3C 263, and 3C 334 all contain trains of knots with an appearance of periodicity. Table 9 tabulates their main properties. A strictly periodic knot train would have equal values of $\Delta\Theta$ (Column 4) for all knots after the first. (If the central feature was itself part of this train, the first entry in this column would match the later entries.)

Table 9 shows that the knot trains from I to F in 3C 204 and from D to H in 3C 263 are particularly close to periodic, with periods near $2\farcs1$ in 3C 204 and $2\farcs5$ in 3C 263. In neither source does the central feature participate in the periodicity of the knot train—in both, it is closer to the first knot in the train than the periodicity would require. In 3C 175 the inter-knot separation lengthens with increasing distance from the central feature, while in 3C 334 there is no steady trend. 3C 334 has the lowest values of the ratio between the knot

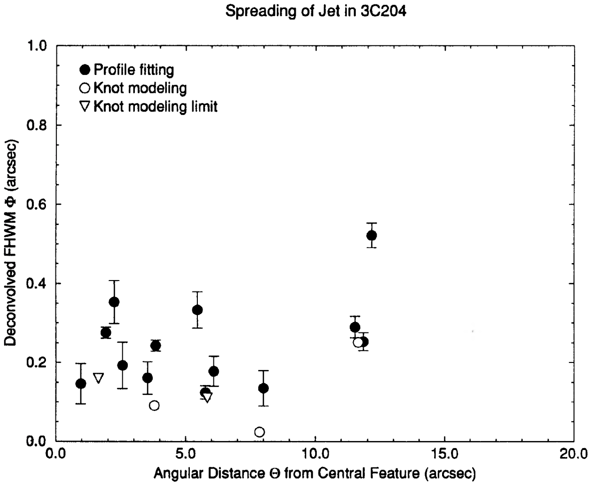

FIG. 39. The deconvolved FWHM Φ transverse to the jet in 3C 204 plotted against angular distance Θ from the central feature. Filled circles show one-dimensional Gaussian fits to the transverse intensity profiles, with their 1σ errors. Open circles show the results of two-dimensional Gaussian modeling of knots, triangles show upper limits from the knot modeling.

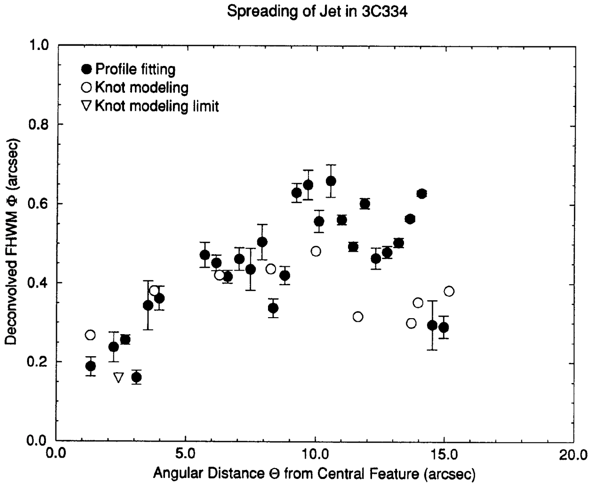

FIG. 41. The deconvolved FWHM Φ transverse to the jet in 3C 334 plotted against angular distance Θ from the central feature. Filled circles show one-dimensional Gaussian fits to the transverse intensity profiles, with their 1σ errors. Open circles show the results of two-dimensional Gaussian modeling of knots, triangles show upper limits from knot modeling.

1994AJ....108..766B

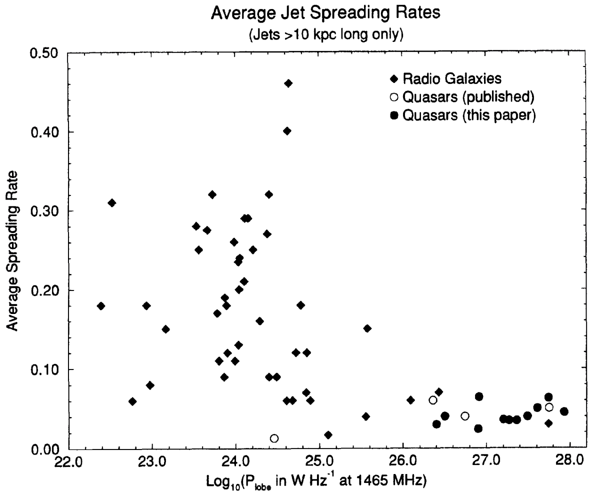

FIG. 42. Average spreading rates of jets that are longer than $10h^{-1}$ kpc in projection, plotted against lobe power in h^{-2} W Hz^{-1} at 1.5 GHz.

separation and the transverse FWHM (between 3.5 and 7). 3C 175 and 3C 263 exhibit higher values (between 12.5 and 14 for 3C 175, and between 14 and 25 for 3C 263), while those for 3C 204 are ill defined (17 to 100) but evidently larger than in 3C 334.

There is a trend for the jet knot closest to the central feature to be brighter than the more distant knots *until the jet is close to its terminating hot spot.* This statement holds for 3C 175, 3C 204, 3C 208, 3C 215, 3C 249.1, 3C 263, 3C 334 (interpreting E2 as the first jet knot and not as part of the central feature), and 3C 351. In 3C 68.1 and 3C 432, the jets do not contain long well resolved knot trains with which to test this statement. Only in 3C 9 and 3C 336 is it clearly false, in the sense that both jets have long segments in which they brighten with distance from the central feature. In several sources, a large fraction of the integrated jet flux density arises within a few hot spot diameters of the terminal hot spot: examples are 3C 68.1 (82% of the integrated jet flux density is in knot C), 3C 204 (28% of the integrated jet flux density is in knot E), 3C 263 (62% of the integrated jet flux density is in knot J), and 3C 336 (58% of the integrated jet flux density is in knot C).

TABLE 9. Trains of jet knots.

Source	Knot ID	Θ (")	ΔΘ (")	Φ (")
3C175	L	2.22	2.22	0.08
3C175	K	5.21	2.99	0.22
3C175	J	8.46	3.25	0.23
3C175	I	11.92	3.46	0.27
3C204	I	1.63	1.63	<0.16
3C204	H	3.79	2.16	0.09
3C204	G	5.83	2.04	<0.11
3C204	F	7.85	2.02	0.02
3C204	E	11.64	3.79	0.25
3C263	D	1.90	1.90	0.12
3C263	E	4.42	2.52	0.14
3C263	F	6.95	2.53	0.10
3C263	G	9.35	2.40	0.17
3C263	H	11.81	2.46	0.15
3C334	F	1.30	1.30	0.27
3C334	G1	2.39	1.09	<0.16
3C334	H	3.76	1.37	0.38
3C334	I	6.29	2.53	0.42
3C334	J	8.26	1.97	0.44
3C334	K1	10.00	1.84	0.48
3C334	K2	11.63	1.63	0.32
3C334	M	13.70	2.07	0.30
3C334	N1	13.96	0.26	0.35
3C334	N2	15.17	1.21	0.38

Notes to TABLE 9

Θ: separation of peak from central feature
ΔΘ: separation of peak from previous peak
Φ: FWHM of knot transverse to jet

5.2.6 Magnetic field strength, minimum pressure, and synchrotron lifetime

Where the jet and putative counterjet features are resolved, we can estimate the equipartition magnetic field strengths B_{eq}, minimum internal pressures, and the synchrotron lifetimes t_{syn} of the electrons radiating in the equipartition field strength at the observed frequency, subject to the conventional assumptions about synchrotron-emitting plasmas (Pacholczyk 1970). Table 10 summarizes the results, with limits to quantities for the unresolved features. These parameters may be used, *subject to the caveats given in the table*, for studies of jet confinement, recollimation, and stability.

Table 10 also computes the ratio ξ between the light-travel time t_c from the central feature to the jet knot and the synchrotron lifetime t_{syn}. Where $\xi > 1$, one or more of the following will apply: (a) the radiating particles have been reaccelerated since leaving the quasar nucleus, (b) the radiating particles did not (in their own frame) travel the entire distance from the nucleus radiating with their present emissivity, or (c) the field strength is below that given by the equipartition assumptions. ξ will be underestimated if the jets are oriented away from the plane of the sky, if much of the detected knot emission is in small structures such as sheets or filaments that do not fill the dimensions estimated here, or if there is more energy in ions than in radiating electrons. ξ will be overestimated if the spectra of the knots steepen above, or flatten below, 4.9 GHz.

Finally, note that if Doppler boosting is important in these jets, the values in Table 10 should be modified by beaming correction factors (see Sec. *7.1*).

5.2.7 Polarimetry

Table 11 lists the polarimetric properties of the total emission at the positions of the peaks of the knots in the jets and counterjet candidates. We have not corrected these polarization parameters for the contribution of more extended emission to the total or polarized intensities at these positions. Thus, if the jet is superposed on lobe emission, the quoted polarization is the sum of the jet and lobe contributions.

The values of the degree of polarization p at the knot peaks range from 5% to ~50%, but are typically ~25%. The degrees of polarization are uncorrelated with the orientation

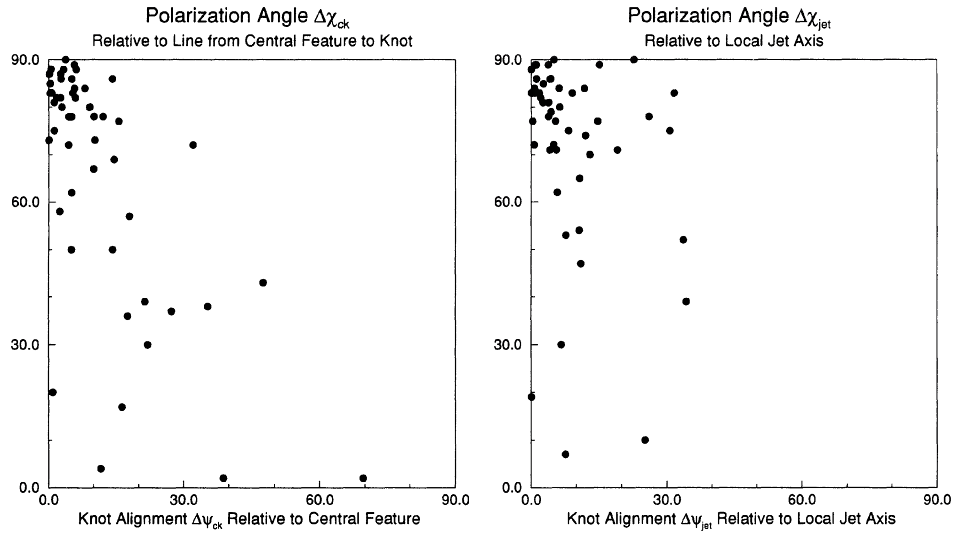

FIG. 43. Polarization alignment data for jet knots. (a—left) plots the angle $\Delta\chi_{ck}$ between the observed **E** vectors and the line joining the knot to the central feature against the orientation $\Delta\psi_{ck}$ of the major axis of the knot relative to the same reference direction. (b—right) plots the same relationship taking the local tangent to the jet as the reference direction.

of the **E** vectors relative to the jet ($\Delta\chi_{jet}$), to the major axis of the knot ($\Delta\chi_{k}$) or to the direction to central feature ($\Delta\chi_{ck}$). The degree of polarization also does not depend systematically on the orientation of the knots themselves relative to the tangent to the jet ($\Delta\psi_{jet}$), or relative to the direction to the central feature ($\Delta\psi_{ck}$).

By contrast, the orientational parameters correlate with each other. The **E**-vector orientation is systematic relative to the local axis of the jet, 78% of the jet knots having $\Delta\chi_{jet}>70°$. It is almost as well organized relative to the major axes of the individual knots, 67% having $\Delta\chi_{k}>70°$. (These correspond to the apparent magnetic vector lying within 20° of the local jet tangent and of the major axis of the knot, respectively). Figure 43 illustrates that the polarization and the knots are often well aligned with the jets and with the direction to the central feature—note the clustering toward the upper left-hand corners ($\Delta\chi=90°$, $\Delta\psi=0°$) in both panels.

Figure 43(a) also shows that the distribution of **E**-vector orientations for the more misaligned knots ($\Delta\psi_{ck}>15°$ in Table 8) differs markedly from that of the knots with $\Delta\psi_{ck}<15°$. The misaligned knots are much less likely to have $\Delta\chi_{ck}>70°$ (i.e., their apparent magnetic vector pointing within 20° of the central feature). In contrast, Fig. 43(b) shows that the **E** vectors at most knots align better with the jet tangent than with the direction to the central feature, and that their orientation relative to the jet is insensitive to the knot's orientation relative to the jet.

Note also that six of the seven points in Fig. 43(a) with $\Delta\psi_{ck}>20°$ and $\Delta\chi_{ck}<70°$ represent the largest bends in their jets. Thus, the trend for misaligned polarization at misaligned knots is dominated by data from the sharpest bends in the jets. (In all but one case—3C 215—the sharpest bend is also at the end of the jet that is farthest from the quasar. In all but one other case—3C 9—it is at the brightest knot, or knot complex for 3C 334.)

Five of the seven points with knot misalignments $\Delta\psi_{jet}>20°$ [Fig. 43(b)] also represent the sharpest bend in their jet, but three of these have $\Delta\chi_{jet}>70°$ and two have $\Delta\chi_{jet}<70°$. It is evidently harder to misalign the polarization with the jet tangent at the largest bends than it is to misalign the jet with the direction to the quasar.

These results show that the process that misaligns knots at bends in the jet also perturbs the pattern of magnetic fields along the jet axis. The trend for the **E** vectors to stay perpendicular to the jet tangent is stronger than any "memory" of the direction to the quasar.

There is no common progression of the degree of polarization p at the knot peaks with separation Θ from the central feature. In 3C 47, 3C 263, and 3C 334, the degrees of polarization at the knot peaks decrease outwards, but in 3C 336 they increase outwards, and in 3C 175 and 3C 204 they decline and recover. In other sources, the polarizations at the knot peaks fluctuate randomly.

We also plotted profiles of the degree of polarization p along the ridge lines of the straighter jet segments where they are relatively unconfused by lobe emission, to examine the polarization properties between the peaks listed in Table 11. We found no general trend for p to change *systematically* with increasing distance along these jet segments, but there are significant local *fluctuations* in many of them.

Fernini *et al.* (1991) commented that the degree of polarization of the jet in 3C 47 apparently increases as the jet enters the south lobe. The degree of polarization along the ridges of other jets in this sample also changes noticeably as the ridges cross into the lobes, but the change is sometimes a decrease. As the emission from the extended lobe structures is often highly polarized at these resolutions, the apparent

1994AJ....108..766B

degree of polarization along a jet ridge can change appreciably whenever the mixture of jet and lobe emission along the line of sight changes. Further analysis is needed to establish whether such changes in the apparent polarization at a jet ridge reflect changes in the polarization state of the jets, or just changes in the blend of polarizations being summed along the line of sight. Such analysis is beyond the scope of this paper. We emphasize however that, in straight jet segments that are *not* confused by lobe emission, we do not find that the degree of linear polarization changes systematically with distance from the central radio feature.

TABLE 10. Derived parameters of knots in jets and counterjet candidates.

Source	Knot ID	B_{eq} (Gauss) $h^{2/7}$	p_{min} (m^{-3} K) $h^{4/7}$	t_{syn} (yr) $h^{-3/7}$	ξ $h^{-4/7}$
3C 9	C	1.4E-04	6.6E+12	1.7E+05	0.08
3C 9	E	>2.2E-04	>1.8E+13	<8.2E+04	>0.16
3C 9	F	4.8E-04	8.2E+13	2.6E+04	1.4
3C 9	G	4.1E-04	6.1E+13	3.3E+04	1.5
3C 9	H	7.5E-04	2.0E+14	1.3E+04	5.4
3C 9	I	5.3E-04	9.9E+13	2.3E+04	3.8
3C 9	J	2.8E-04	2.8E+13	5.9E+04	1.7
3C 47	B	2.6E-05	2.3E+11	3.0E+06	0.09
3C 47	C	3.3E-05	3.9E+11	2.1E+06	0.10
3C 47	D	3.3E-05	3.7E+11	2.1E+06	0.08
3C 47	E1	2.2E-05	1.7E+11	3.7E+06	0.02
3C 47	E2	>1.6E-05	>9.2E+10	<5.6E+06	>0.02
3C 47	F	4.4E-05	6.8E+11	1.4E+06	0.02
3C 68.1	C	3.1E-04	3.5E+13	5.8E+04	5.0
3C 68.1	D	5.4E-05	1.1E+12	7.6E+05	0.16
3C 68.1	F1	1.6E-04	9.4E+12	1.6E+05	0.85
3C 68.1	F2	8.0E-05	2.3E+12	4.3E+05	0.31
3C175	D	1.0E-04	3.6E+12	3.6E+05	0.95
3C175	E	5.5E-05	1.1E+12	8.6E+05	0.35
3C175	F	4.9E-05	8.7E+11	1.0E+06	0.29
3C175	I	6.1E-05	1.3E+12	7.5E+05	0.21
3C175	J	6.3E-05	1.4E+12	7.1E+05	0.16
3C175	K	6.2E-05	1.4E+12	7.3E+05	0.10
3C175	L	1.6E-04	8.9E+12	1.8E+05	0.16
3C204	E	1.1E-04	4.4E+12	2.8E+05	0.58
3C204	F	3.2E-04	3.8E+13	5.7E+04	1.9
3C204	G	>1.5E-04	>8.5E+12	<1.7E+05	>0.47
3C204	H	1.7E-04	1.0E+13	1.5E+05	0.35
3C204	I	>1.8E-04	>1.2E+13	<1.3E+05	>0.18
3C208	D	1.8E-04	1.1E+13	1.4E+05	0.28
3C208	E	1.1E-04	4.5E+12	2.8E+05	0.09
3C208	F	3.1E-04	3.4E+13	6.1E+04	0.18
3C215	D	2.5E-04	2.2E+13	1.0E+05	0.37
3C215	E	6.2E-05	1.4E+12	8.3E+05	0.08
3C215	F	9.3E-05	3.1E+12	4.5E+05	0.20
3C249.1	E	1.9E-04	1.2E+13	1.7E+05	0.06
3C249.1	I	1.2E-04	5.5E+12	3.0E+05	0.16
3C249.1	J	1.4E-04	7.3E+12	2.5E+05	0.22
3C263	D	1.2E-04	5.5E+12	2.7E+05	0.09
3C263	E	9.0E-05	2.9E+12	4.3E+05	0.13
3C263	F	1.2E-04	5.2E+12	2.8E+05	0.31
3C263	G	7.9E-05	2.3E+12	5.3E+05	0.23
3C263	H	8.5E-05	2.6E+12	4.7E+05	0.32
3C263	J	1.5E-04	7.7E+12	2.1E+05	0.93
3C334	D	4.4E-05	6.9E+11	1.3E+06	0.18
3C334	E2	3.8E-04	5.1E+13	5.3E+04	0.01
3C334	F	6.0E-05	1.3E+12	8.2E+05	0.02
3C334	G1	>1.0E-04	>3.6E+12	<3.8E+05	>0.08
3C334	G2	1.3E-04	6.4E+12	2.5E+05	0.14
3C334	H	4.8E-05	8.2E+11	1.1E+06	0.04
3C334	I	5.1E-05	9.2E+11	1.0E+06	0.07
3C334	J	5.1E-05	9.3E+11	1.0E+06	0.10
3C334	K1	4.0E-05	5.6E+11	1.5E+06	0.08
3C334	K2	5.5E-05	1.1E+12	9.3E+05	0.15
3C334	M	6.8E-05	1.6E+12	6.9E+05	0.24
3C334	N1	5.2E-05	9.8E+11	1.0E+06	0.17
3C334	N2	7.3E-05	1.9E+12	6.1E+05	0.30
3C336	C	3.4E-04	4.2E+13	5.5E+04	1.5
3C336	D	1.2E-04	5.5E+12	2.5E+05	0.27
3C336	E	1.2E-04	4.9E+12	2.7E+05	0.16
3C336	F	1.5E-04	7.7E+12	1.9E+05	0.12
3C336	G	1.0E-04	3.7E+12	3.3E+05	0.04
3C336	I	1.2E-04	5.0E+12	2.7E+05	0.71
3C336	J	1.3E-04	6.5E+12	2.2E+05	0.95
3C351	C	>4.0E-05	>5.7E+11	<1.6E+06	>0.004
3C351	E	4.1E-04	6.2E+13	4.9E+04	0.08
3C351	F	1.0E-04	3.6E+12	4.1E+05	0.03
3C351	G	6.9E-05	1.7E+12	7.1E+05	0.03
3C432	D1	>1.0E-04	>3.6E+12	<2.7E+05	>0.10
3C432	D2	>5.3E-05	>1.0E+12	<6.4E+05	>0.06

Assumptions made when computing TABLE 10:

Elliptic cylindrical emitting volume, fully filled
Major, minor axes = LAS, SAS from Table 8
Depth = SAS from Table 8
Spectral index = 0.6
Luminosity integrated from 10 MHz to 100 GHz in quasar frar
Equal energies in ions and electrons
Electrons move with random pitch angles
Electrons in constant field throughout lifetime
H_0=100h km s^{-1} Mpc^{-1}, q_0=0.5

5.3 The Hot Spots

Table 12(a) lists the parameters of single-component Gaussian models fitted to the hot spots. Because not all the hot spot structures are well represented by Gaussian models, these parameters are only rough guides to the total flux densities, angular sizes, and orientations of the hot spots. Some hot spots contain compact substructure that was not well represented by fitting a single component to all the emission that contributed to our classification of the region. Table 12(b) lists parameters for these more compact substructures, which carry the designation 1 after the alphabetic knot code.

TABLE 11. Polarization of knots in jets and counterjet candidates.

Source	Knot ID	Θ (")	p	χ (°)	$\Delta\chi_{ck}$ (°)	$\Delta\chi_{jet}$ (°)	$\Delta\chi_{k}$ (°)
3C 9	C	1.03	<0.21				
3C 9	E	0.99	0.25	74	82	79	84
3C 9	F	2.78	0.16	6	36	52	19
3C 9	G	3.57	0.30	41	78	88	88
3C 9	H	5.42	0.29	23	62	70	57
3C 9	I	6.47	0.09	41	82	77	88
3C 9	J	7.26	0.10	-16	30	83	52
3C 47	F	3.06	0.29	-65	86	84	72
3C 47	E1	7.96	<0.14				
3C 47	E2	9.23	0.16	-69	80	81	81
3C 47	D	15.57	<0.14				
3C 47	C	19.31	0.19	-56	87	89	90
3C 47	B	23.73	0.14	-40	72	77	77
3C 68.1	F2	9.63	<0.10				
3C 68.1	F1	9.35	0.05	68	71		56
3C 68.1	D	8.68	0.09	86	89	90	85
3C 68.1	C	20.75	0.49	-10	2	90	67
3C175	L	2.22	0.21	-40	83	83	82
3C175	K	5.21	0.31	-40	83	83	83
3C175	J	8.46	<0.20				
3C175	I	11.92	<0.14				
3C175	F	21.72	<0.10				
3C175	E	22.68	0.19	36	17	7	1
3C175	D	25.23	0.29	47	4	10	15
3C204	I	1.63	0.25	0	87	86	87
3C204	H	3.79	<0.10				
3C204	G	5.83	0.19	-64	20	19	19
3C204	F	7.85	0.19	1	86	85	83
3C204	E	11.64	0.32	58	39	53	60
3C208	F	0.77	0.40	19	58	62	56
3C208	E	1.72	0.20	-11	88	82	84
3C208	D	2.72	0.46	-16	81	78	82
3C215	D	3.60	0.20	80	2	30	37
3C215	E	5.84	0.17	48	50	75	45
3C215	F	8.25	0.11	66	37	54	65
3C249.1	E	1.01	0.11	-30	50	47	36
3C249.1	I	5.19	0.25	-24	57	71	75
3C249.1	J	5.97	0.05	-6	78	86	90
3C263	D	1.90	0.27	27	82	81	85
3C263	E	4.42	<0.11				
3C263	F	6.95	0.20	14	85	84	85
3C263	G	9.35	0.15	36	73	72	73
3C263	H	11.81	<0.08				
3C263	J	15.38	0.18	26	84	78	76
3C334	D	19.73	<0.14				
3C334	F	1.30	0.48	55	88	89	87
3C334	G1	2.39	0.39	44	76	83	88
3C334	G2	2.87	0.30	68	75	71	77
3C334	H	3.76	0.21	73	69	65	54
3C334	I	6.29	0.43	64	78	77	82
3C334	J	8.26	0.29	61	80	81	83
3C334	K1	10.00	0.21	58	83	84	78
3C334	K2	11.63	0.31	56	86	83	81
3C334	M	13.70	0.27	41	80	86	90
3C334	N1	13.96	0.19	31	72	89	76
3C334	N2	15.17	0.28	1	43	71	90
3C336	J	15.22	0.39	41	15		58
3C336	I	13.69	0.20	-72	86		62
3C336	G	0.97	<0.13				
3C336	F	1.72	0.13	-57	78	83	83
3C336	E	3.12	0.19	-50	73	75	83
3C336	D	4.91	0.23	-65	90	80	86
3C336	C	6.03	0.20	-11	38	39	73
3C351	C	0.61	<0.17				
3C351	E	0.40	0.13	-31	84	89	90
3C351	F	1.21	0.31	-53	67	72	77
3C351	G	1.85	0.11	-38	88	74	86
3C432	D1	2.02	<0.10				
3C432	D2	2.79	<0.40				

Notes to TABLE 11

Θ: angular distance between peak of knot and central feature
(knots are listed in order of increasing Θ along the jets,
and of decreasing Θ along the counterjet candidates)
p: fractional polarization (or 2σ upper limit) at position of peak
χ: apparent position angle of the $\mathbf{E}$ vector at the peak
$\Delta\chi_{ck}$: angle between $\mathbf{E}$ vector and line from peak to central feature
$\Delta\chi_{jet}$: angle between $\mathbf{E}$ vector and local tangent to jet
$\Delta\chi_{k}$: angle between $\mathbf{E}$ vector and major axis of knot

TABLE 12. Parameters of hot spots and hot spot candidates.

(a) Single-Component Fits

Source	Knot ID	Θ (")	$S_{\rm int}$ (mJy)	LAS (")	SAS (")	ψ (°)	$\psi_{\rm ch}$ (°)	$\Delta\psi_{\rm ch}$ (°)
3C 9	A	5.17	47.3	0.62	0.36	72	144	72
3C 9	K	7.85	15.2	0.90	0.28	168	124	44
3C 47	A	38.20	268.	1.01	0.63	122	33	89
3C 68.1	B	21.72	362.	0.79	0.22	51	170	61
3C175	C	28.31	63.5	0.57	0.35	32	50	18
3C175	O	21.04	152.	0.51	0.38	77	62	15
3C204	D	12.99	61.4	0.25	0.21	16	99	83
3C204	L	18.29	42.2	0.25	0.22	20	95	75
3C208	B	4.98	27.7	0.24	0.21	7	76	69
3C208	J	6.46	203.	0.26	0.21	110	78	32
3C215	G	10.19	7.3	0.45	0.30	43	106	63
3C249.1	A	15.63	188.	1.37	0.98	94	100	6
3C249.1	K	7.67	86.3	0.39	0.26	1	92	89
3C263	B	27.76	20.8	0.34	0.29	23	111	88
3C263	K	16.25	528.	0.30	0.26	165	112	53
3C334	O	17.68	19.7	0.76	0.29	71	132	61
3C336	B	7.65	95.1	0.39	0.29	118	25	87
3C336	K	15.27	254.	1.03	0.61	53	37	16
3C351	J	25.18	201.	0.22	0.18	178	46	48
3C432	B	5.23	5.7	0.26	0.23	16	135	61
3C432	H	7.62	105.	0.31	0.16	146	135	11

(b) Most Compact Component

Source	Knot ID	Θ (")	$S_{\rm int}$ (mJy)	LAS (")	SAS (")	ψ (°)	$\psi_{\rm ch}$ (°)	$\Delta\psi_{\rm ch}$ (°)
3C 9	K1	7.96	5.6	0.33	0.22	19	125	74
3C 47	A1	38.25	239.	0.79	0.62	107	33	74
3C 68.1	B1	21.61	128.	0.23	0.13	15	170	25
3C175	C1	28.19	33.9	0.36	0.25	128	51	77
3C175	O1	21.11	88.0	0.34	0.26	20	63	43
3C334	O1	17.69	9.6	0.50	0.30	89	132	43
3C432	H1	7.65	96.6	0.23	0.19	148	135	13

(c) Rejected Candidates

Source	Knot ID	Θ (")	$S_{\rm int}$ (mJy)	LAS (")	SAS (")	ψ (°)	$\psi_{\rm ch}$ (°)	$\Delta\psi_{\rm ch}$ (°)
3C 47	H	31.19	166.	4.76	1.87	139	38	79
3C 68.1	H	26.64	2.7	1.28	0.76	67	176	71
3C215	A	21.90	23.4	2.49	2.23	50	149	81
3C334	C	26.72	3.3	0.55	0.27	91	133	42
3C351	A	36.58	6.0	1.19	0.70	119	30	89

Despite the model-fitting uncertainties, Table 12 contains some notable trends:

(a) *All* five lobes that contain *no* hot spots by our criteria (3C 47 N, 3C 68.1 S, 3C 215 N, 3C 334 NW and 3C 351 SW) are on the counterjetted side of the source. (In all five, the most promising candidate [Table 12(c)] had a surface brightness <25 mJy per sq arcsec, whereas the features that met our criteria all have brightnesses >50 mJy per sq arcsec.) The five sources without hot spots (by our criteria) in their counterjetted lobes are also the five largest sources in the sample by angular extent, and among the seven largest by projected linear extent. (The mean projected linear size for the five sources without counterjetted hot spots is $226\pm26h^{-1}$ kpc, while that for the eight with counterjetted hot spots is $127\pm62h^{-1}$ kpc.) This apparent trend for the more extended sources to lack counterjetted hot spots may be real, for there is no comparably clear connection between the presence of counterjetted hot spots and the linear resolution of our images (as might be expected if the effect is produced solely by differing relative resolutions for sources of different sizes).

(b) In nine sources the hot spot candidates differ in area by more than 25%. In all nine, the jetted hot spot is the more compact. Only in 3C 175 and 3C 334 is the smaller hot spot candidate (by area) in the counterjetted lobe; in both sources, the hot spots differ in area by less than 2%. In 3C 175, the jetted hot spot is smaller than its counterjetted counterpart on the minor axis, but not on the major axis. In 3C 334, the feature in the counterjet lobe (C) does not qualify as a hot spot because of low brightness contrast, and might be a knot in the counterjet. We conclude that there is a strong trend for the jetted hot spot to be the more compact when there is a significant size asymmetry.

(c) The ratio of the compactness of the jetted to that of the counterjetted hot spots also depends on the apparent power of the central feature (linear correlation coefficient $r=0.83$ for all 13 sources). The extrema of this trend are defined by the sources with the three least powerful central features (3C 68.1, 3C 215, and 3C 351), which have the smallest ratios of hot spot areas (jetted/counterjetted), while the four with the most powerful central features (3C 204, 3C 208, 3C 263, and 3C 334) have similar-sized hot spots or candidates on both sides. There is no similarly clear dependence of hot spot compactness ratios directly with red shift.

(d) In this sample, any systematic asymmetries in the integrated flux density between the hot spot candidates in the jetted and counterjetted lobes are much weaker than those described above for hot spot compactness. The asymmetry in the hot spot surface brightnesses is also correspondingly weaker.

(e) Hot spots that are fed by jets are more likely to be deeply recessed into their lobes than are those on the counterjet side (Fig. 44). We measure hot spot recession by the ratio R of the angular distance Θ from the central feature to the peak of the hot spot (Table 12) to the largest angular extent of the lobe (Table 15, Sec. 5.4 below). No hot spot on the counterjet side has $R<0.82$, but 7 of the 13 jetted hot spots have $R<0.73$. The two most deeply recessed jetted hot spots are in 3C 215 and 3C 249.1, which have the lowest lobe powers (and redshifts) in our sample.

There are no sample-wide trends involving hot spot collimation (as defined by the angle subtended by the hot spot at

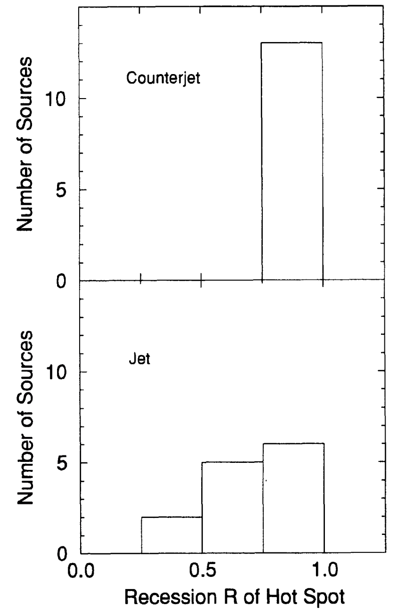

FIG. 44. Distributions of hot spot recession parameter R in jetted and counterjetted lobes. R is the ratio between the angular distance from the central feature to the hot spot and the largest angular extent of the lobe.

TABLE 13. Derived parameters of hot spots and hot spot candidates.

Source	Knot ID	B_{eq} (Gauss) $h^{2/7}$	p_{min} (m^{-3} K) $h^{4/7}$	t_{syn} (yr) $h^{-3/7}$	ξ $h^{-4/7}$
3C 9	A	4.8E-04	8.4E+13	2.6E+04	2.7
3C 9	K1	4.1E-04	6.2E+13	3.3E+04	3.3
3C 47	A1	2.0E-04	1.4E+13	1.4E+05	2.9
3C 47	H	5.7E-05	1.2E+12	9.2E+05	0.36
3C 68.1	B1	9.9E-04	3.6E+14	1.0E+04	30.
3C 68.1	H	7.4E-05	2.0E+12	4.9E+05	0.77
3C175	C1	3.0E-04	3.3E+13	6.8E+04	5.5
3C175	O1	4.0E-04	5.6E+13	4.6E+04	6.1
3C204	D	5.5E-04	1.1E+14	2.5E+04	7.2
3C204	L	4.8E-04	8.4E+13	3.1E+04	8.3
3C208	B	4.5E-04	7.1E+13	3.5E+04	2.0
3C208	J	7.8E-04	2.2E+14	1.5E+04	5.9
3C215	A	3.5E-05	4.4E+11	1.9E+06	0.12
3C215	G	1.3E-04	6.0E+12	2.7E+05	0.40
3C249.1	A	1.1E-04	4.7E+12	3.4E+05	0.42
3C249.1	K	2.8E-04	2.8E+13	9.0E+04	0.78
3C263	B	2.3E-04	1.8E+13	1.1E+05	3.2
3C263	K	6.3E-04	1.4E+14	2.4E+04	8.7
3C334	C	1.1E-04	4.6E+12	3.2E+05	1.0
3C334	O1	1.5E-04	8.0E+12	2.1E+05	1.0
3C336	B	4.1E-04	6.0E+13	4.2E+04	2.5
3C336	K	2.7E-04	2.6E+13	7.9E+04	2.7
3C351	A	5.6E-05	1.1E+12	9.8E+05	0.38
3C351	J	5.4E-04	1.0E+14	3.3E+04	7.7
3C432	B	3.9E-04	5.5E+13	3.7E+04	1.9
3C432	H1	1.0E-03	3.7E+14	8.8E+03	12.

Assumptions made when computing TABLE 13:

Elliptic cylindrical emitting volume, fully filled
Major, minor axes = LAS, SAS from Table 12
Depth = SAS from Table 12
Spectral index = 0.8
Luminosity integrated from 10 MHz to 100 GHz in quasar frame
Equal energies in ions and electrons
Electrons move with random pitch angles
Electrons in constant field throughout lifetime
$H_0=100h$ km s^{-1} Mpc^{-1}, $q_0=0.5$

the central feature). The flux density ratio between the jetted and counterjetted hot spots is larger when the jetted hot spot is well collimated ($r=-0.76$, see Table 22), but the significance of this trend depends strongly on just two sources, 3C 68.1 and 3C 351, with unusually large flux density ratios between their hot spots.

We discuss trends involving hot spot prominence in Sec. 5.5.

Table 13 lists derived physical properties for the hot spots, assuming that their spectral indices are $\alpha_{hs}=0.8$, but otherwise with the same assumptions as in Table 10. The "reacceleration indicator" $\xi=t_c/t_{syn}$ is generally higher for the hot spots than for the jet knots (Table 10), because the hot spots tend to be both brighter and further from the central features. Note, however, that we find values of $\xi>1$ in both jetted *and* counterjetted hot spots (3C 175, 3C 204, 3C 208, see Sec. 7).

TABLE 14. Polarization of hot spots.

Source	Knot ID	Θ (")	p	χ (°)	$\Delta\chi_{ch}$ (°)	$\Delta\chi_{jet}$ (°)	$\Delta\chi_h$ (°)
3C 9	A	5.17	0.02	24	60		48
3C 9	K	7.85	0.37	72	52	12	84
3C 47	A	38.20	0.23	27	6	1	85
3C 68.1	B	21.72	0.17	88	82	71	37
3C175	C	28.31	0.17	-67	63	53	81
3C175	O	21.04	0.16	-30	88		73
3C204	D	12.99	0.29	-38	43	16	54
3C204	L	18.29	0.15	61	34		41
3C208	B	4.98	0.03	-48	56	88	55
3C208	J	6.46	0.18	-16	86		54
3C215	G	10.19	0.27	-63	11	13	74
3C249.1	A	15.63	0.03	44	56		50
3C249.1	K	7.67	0.08	-23	65	79	24
3C263	B	27.76	0.13	-44	25		67
3C263	K	16.25	0.04	-51	17	7	36
3C334	O	17.68	0.14	-18	30	46	89
3C336	B	7.65	0.13	-6	31	16	56
3C336	K	15.27	0.02	-17	54		70
3C351	J	25.18	0.20	62	16	29	64
3C432	B	5.23	0.30	29	74		13
3C432	H	7.62	0.02	-47	2	4	13

Notes to TABLE 14

Θ: angular distance between peak of hot spot and central feature
p: fractional polarization (or 2σ upper limit) at position of peak
χ: apparent position angle of the **E** vector at the peak
$\Delta\chi_{ch}$: angle between **E** vector and line from peak to central feature
$\Delta\chi_{jet}$: angle between **E** vector and tangent to jet before hot spot (for jetted hot spots only)
$\Delta\chi_h$: angle between **E** vector and major axis of hot spot

TABLE 15. Integrated properties of lobes.

	Jetted Side		Unjetted Side	
Source	Integrated Flux Density (mJy)	Largest Extent (")	Integrated Flux Density (mJy)	Largest Extent (")
3C 9	45	8.5	110	5.8
3C 47	690	42	402	35
3C 68.1	612	24	45	30
3C175	259	31	367	21
3C204	159	18.0	122	18.2
3C208	90	7.5	400	6.5
3C215	175	32	199	27
3C249.1	234	29	454	18
3C263	739	17	191	33
3C334	177	29	276	32
3C336	205	11.5	523	16.3
3C351	1046	37	72	38
3C432	156	8.2	202	6.4

* excluding jets and counterjet candidates

Table 14 lists the polarization properties at the peaks of the hot spots. There are no strong trends involving the degrees of polarization, or the E-vector orientations, of the hot spots on the jetted and counterjetted sides. The lack of trends among these quantities in our sample may be influenced by the strictness of our compactness criterion for hot spots, as the internal polarization distributions of most structures that meet it are poorly resolved.

5.4 The Lobes

Table 15 lists the integrated flux densities of the jetted and counterjetted lobes in each source. These estimates do not include the flux densities of the embedded jets or counterjet candidates, if any. They were obtained by summing pixel intensities and normalizing by the CLEAN beam area using the TVSTAT facility in AIPS, then subtracting the integrated contributions from the jets and counterjet candidates as appropriate. Table 15 also shows the distances from the central feature to the furthest point that can reliably be said to include lobe emission, to measure the "largest extent" of the lobe.

The jetted lobe is not systematically stronger or weaker than the counterjetted lobe, nor does it extend systematically further or less far from the quasar. (The jetted lobe is weaker than the counterjetted lobe in 8 of the 13 and extends further from the central feature than does the counterjetted lobe in 7 of the 13.) The *ratio* of flux densities between the jetted and counterjetted lobes correlates significantly with several parameters, however. The ratio for the extended emission alone increases with the projected linear size of the source ($r=0.74$). The ratio including the hot spots correlates less well with linear size ($r=0.66$), but anticorrelates significantly ($r=-0.75$) with the angle subtended by the jetted hot spot at the central feature, the latter trend depending strongly on the data for 3C 68.1 and 3C 351.

The detectability of the counterjet candidates does not depend systematically on the ratio of the integrated lobe flux densities. For example, the two most convincing counterjet candidates, in 3C 68.1 and 3C 215, are found in the sources with the largest and smallest lobe-to-lobe intensity ratios, respectively. Counterjet detectability also does not seem to depend systematically on the ratio of the extents of the lobes. For example, the sources with the largest ratios of jetted lobe to counterjetted lobe extents include two (3C 9 and 3C 249.1) with counterjet candidates and one (3C 175) without.

We have looked for lobe properties that correlate with jet sidedness, as tests of models for jet asymmetry. For example, in the Doppler favoritism model of jet one-sidedness, the extended lobe emission, which is likely to be unbeamed, should reflect the underlying symmetry of the power supply from the nucleus. Conversely, a real asymmetry in the power supply might manifest itself as an asymmetry in the content of the lobes.

We have attempted to quantify the morphological characteristics of the lobes of these quasars using two measures of lobe inhomogeneity. As we are interested primarily in the lobe emission, we used the AIPS task BLANK to prepare two sets of edited images, the first with the (potentially beamed) jet emission excised, and the second with both the jet and the hot spots removed. The putative counterjet emission was not removed from either of these sets of edited images. The edited images of each lobe were then analyzed for inhomogeneity using two independent methods.

The first method employed the Sobel edge enhancement filter (see, e.g., Pratt 1978), as implemented in the AIPS 3×3 filtering task NINER. The Sobel filter computes a quantity proportional to the intensity gradient

$$\sqrt{\left(\frac{\partial I}{\partial \alpha}\right)^2+\left(\frac{\partial I}{\partial \delta}\right)^2}$$

as a function of position on the image. By summing the values in the Sobel-filtered image over the region containing the lobe, and normalizing by the integrated lobe flux density, we obtain a measure of integrated lobe inhomogeneity that depends only on the lobe structure (not on the intensity). Because the output of the Sobel filter is everywhere positive, this measure of the integrated inhomogeneity increases with the area over which the integration is performed, even if some of the area contains only noise. We therefore also used BLANK to excise all regions of the image with signal-to-rms noise ratios <3 before applying this filter.

The second method uses structure functions, as implemented in the AIPS task STFUN. The structure function $S(l_x,l_y)$ of an image is given by the expression

$$S(l_x,l_y)=\frac{\sum_{x=x_{\min}}^{x=x_{\max}}\sum_{y=y_{\min}}^{y=y_{\max}}[I(x,y)-I(x+l_x,y+l_y)]^2}{(x_{\max}-x_{\min})(y_{\max}-y_{\min})},$$

where l_x and l_y are pixel lags, $I(x,y)$ is the image intensity as a function of position, and $x_{\min}$, $x_{\max}$, $y_{\min}$, $y_{\max}$ are the pixel extrema of the input image. By computing $S(l_x,l_y)$ over a range of 25 pixels in l_x and l_y, we constructed a two-dimensional structure function for each lobe consisting of 51×51 elements, with the origin blanked. This function measures the degree of inhomogeneity in the original image up to scale sizes corresponding to about $2\farcs5$. The inhomogeneity measure was derived by computing the mean value of the structure function, and normalizing by the square of the integrated lobe flux density. The resulting quantity resembles the measure derived from the Sobel filter in that it depends only on the structure of the lobe, but differs from the Sobel-filter measure in that it takes moderate-scale inhomogeneities into account as well as those that contribute to local brightness gradients.

Table 16 shows the results of this analysis, as logarithmic ratios of the inhomogeneity measures for the jetted to the counterjetted lobes. The estimators agree over which lobe is the more inhomogeneous when either estimator is outside the range 0.0±0.2. We conclude that our two methods for estimating lobe inhomogeneity agree well with each other. If the hot spots are not removed, there is a tendency, significant at the 2.5σ level, for the jetted lobe to be the more inhomogeneous. If the hot spots are removed, a small effect remains, but only at the 1σ level. These inhomogeneity measures reinforce our conclusion in Sec. 5.3 that the more compact hot spots preferentially appear in the jetted lobes. They further show that *these hot spots represent the main difference in inhomogeneity between the two lobes*. Note that this includes the contributions to the inhomogeneity from any less compact features (ridges, filaments, or other fine structure) in either lobe.

The evidence for counterjets improves as the lobes depart from collinearity and symmetry. For example, apart from 3C 68.1, the stronger counterjet candidates (3C 9, 3C 215, 3C 334, and 3C 351) are in sources whose jetted and counterjetted lobes are displaced to opposite sides of the jet–counterjet axis (S symmetry). Such displacements of most of the lobe emission from the jet–counterjet axis could be seen as evidence for a long-term perturbation of the symmetry axis of the underlying beam, independent of the evidence for perturbations (wiggling) of the jets themselves. The sources with the least evidence for counterjet emission (3C 175, 3C 204, 3C 208, 3C 263, and 3C 336) show much less morphological evidence of perturbation of the beams. For 3C 249.1, which displays only weak evidence for a counterjet if one excludes the emission "rings" in the west lobe, there is some morphological distortion (to C symmetry). These results are supported by considering the alignments between the peaks of the hot spots (or hot spot candidates) and the central features. The mean hot spot alignment angle $(\psi_{\mathrm{ch,jetside}}-\psi_{\mathrm{ch,cjetside}})$ for the seven sources with counterjet candidates is $15\fdg1$, while that for the six without counterjet candidates is $4\fdg0$.

The above relations between lobe morphology and counterjet detectability reinforce the conclusions drawn in Sec. 5.2.2 from comparing counterjet detections directly with jet bending parameters.

TABLE 16. Inhomogeneity measures of lobes.

	Hot Spots Included		Hot Spots Removed	
Source	logJ - logCJ Sobel method	logJ - logCJ Struct funct	logJ - logCJ Sobel method	logJ - logCJ Struct funct
3C 9	0.00	+0.11	-0.18	+0.14
3C 47	+0.26	+1.05	+0.04	+0.53
3C 68.1	+0.59	+1.69	+0.31	+0.94
3C175	-0.14	-0.48	-0.04	-0.09
3C204	+0.04	+0.05	+0.05	-0.18
3C208	-0.19	-0.12	-0.17	-0.39
3C215	+0.12	+0.33	+0.06	+0.03
3C249.1	+0.31	+0.31	+0.06	-0.04
3C263	+0.46	+0.98	+0.11	+0.22
3C334	+0.15	+0.13	0.00	-0.59
3C336	+0.20	+1.11	+0.07	+0.85
3C351	+0.70	+1.63	+0.59	+1.60
3C432	+0.19	+0.36	-0.19	-0.58
Mean	+0.20±0.08	+0.55±0.19	+0.05±0.06	+0.19±0.19

The polarimetry of the extended lobe emission shows a recurrent pattern—low polarization at the center of the lobes, higher polarization at their edges. The implied magnetic field orientations (assuming the Faraday rotation corrections to be small for 4.9 GHz) are that **B** prefers to be parallel to the lobe boundaries. This pattern resembles that predicted by models in which the magnetic field is well ordered on the outer boundaries of the lobes and is stretched parallel to their major extensions. Clarke *et al.* (1989) and Matthews & Scheuer (1990) showed that such polarization patterns are expected in models in which the magnetic fields in the lobes arise from passive expansion of the fields convected out by the jets (so that radial field components are suppressed). Superposed on these general patterns are features such as highly polarized filaments and rings whose magnetic field directions tend to be parallel to the intensity ridge lines.

5.5 Prominence Parameters and Their Correlations

When trying to discriminate among alternative radio source models, it is useful to ask whether the luminosity of a particular type of compact emission (e.g., central feature, jet, hot spot) scales with the integrated power of the more extended emission. For example, in relativistic twin-beam models the apparent luminosity of some compact features depends on the orientation of the source relative to us, while that of the most extended features should not. This section examines relationships between features in terms of their *prominence*, defined as the ratio of their integrated flux density to that of appropriately selected lobe emission.

5.5.1 Choice of prominence parameters

For this work, we normalize prominence measures by the *extended* flux density of one or both lobes, i.e., by the integrated flux density of the lobe(s) minus that of any hot spots or hot spot candidates. This normalization is especially appropriate when evaluating relativistic twin-beam models, as it refers the prominence of all features to those that are most likely to be unbeamed and thus independent of orientation.

A further subtlety involves how to partition the flux densities in the central features and jets for prominence analysis. It is interesting to separate the flux density of milliarcsecond-scale structure where possible, because only on such small (typically parsec) scales is there widespread evidence for highly relativistic flow speeds in powerful sources. Whether such speeds persist to much larger (many-kiloparsec) scales is indeed a key hypothesis to be tested.

We do not, however, have 5 GHz VLBI data to show directly what fractions of Table 5's 4.9 GHz VLA "central feature" flux densities emanate from milliarcsecond scales. We therefore use VLBI data at 8.4 or 10.7 GHz, where available (Hough 1986; Hough *et al.* 1992; Vermeulen *et al.* 1993; Zensus *et al.* 1987; Hough unpublished), to estimate this contribution. These estimates are somewhat uncertain because we have only limited data on the central feature spectra and variability—we therefore simply assume a spectral index of zero, and invariant flux density. When no VLBI data are available, we assume that the milliarcsecond-scale fraction of our VLA central feature flux density matches the average (~75%) for the sources whose VLBI properties are known. The effect of these assumptions on the derived central feature prominence is never dramatic.

In contrast, the derived jet prominence sometimes increases significantly if the intermediate-scale flux density deducted from the VLA central feature is added to that of the extended jet. Without imaging on scales from ~0.01 to 0.4 arcsec, we cannot determine unambiguously where to place this intermediate-scale flux density. We therefore estimate the jet prominence both with and without it in what follows. (We do not consider assigning this flux density to the counterjet, since whenever a VLBI jet has been imaged it points toward the VLA jet. It therefore seems reasonable to assume that the intermediate-scale emission is also mainly on the jet side.) Table 17 lists the flux densities of the central features and jets for the case in which the intermediate-scale flux density is assigned to the jets.

TABLE 17. Flux densities of central features and jets with intermediate-scale emission assigned to jets.

Source	Central Feature (mJy)	Whole Jet (mJy)	Straight Jet (mJy)
3C 9	3.7	332.2	2.38
3C 47	73.6	23.0	6.2
3C 68.1	0.8	116.3	2.4
3C175	14.1	34.4	11.8
3C204	18.8	15.5	13.2
3C208	35.7	41.3	25.0
3C215	13.1	30.4	6.3
3C249.1	50.0	73.0	34.4
3C263	141.0	43.0	23.5
3C334	95.2	67.8	54.3
3C336	15.3	71.6	9.5
3C351	5.2	15.6	11.0
3C432	5.6	6.4	2.47

Table 18 lists the luminosities and Table 19 the prominence ratios for the central features, jets, hot spots, and extended lobe emission in this sample, subject to the alternative normalizations and flux-density assignments discussed above. Table 20 lists linear correlation coefficients r between the logarithms of the prominence ratios and other parameters of the sources that we discuss in detail below.

5.5.2 Jets, counterjets, and central features

Figure 45(a) shows a positive correlation between the prominence of the straightest segments of the jets (as defined in Sec. 5.2) and of the central features. The extrema are represented by 3C 263 and 3C 334 (central features and straight jets both prominent) and by 3C 68.1 and 3C 351 (central features and straight jets both inconspicuous). This correlation is strong ($r=0.83$ for the logarithms of the prominence ratios) when both flux densities are normalized by the extended flux density of the jetted lobe, as in Fig. 45(a). It is weaker ($r=0.65$) if the prominence measures are normalized by the corresponding flux density of the counterjetted lobe, as in Fig. 45(b). (The difference between the correlation strengths with these two normalizations is mainly due to 3C 68.1 and 3C 351, both of which have large ratios of flux density between their jetted and counterjetted lobes).

TABLE 18. Luminosities of radio features.

Source	Pcf,A	Pcf,B	Pj,A	Pj,B	Pcj	Pjh	Pcjh	Px
	Logarithmic Luminosities at 5 GHz emitted, P (h^{-2} W Hz^{-1})							
3C 9	25.06	24.94	27.18	27.18	24.21	25.93	26.43	26.81
3C 47	25.08	25.08	24.66	24.66	<23.93	25.76	25.55	26.18
3C 68.1	24.07	23.93	26.30	26.30	24.63	26.86	24.74	26.84
3C175	25.04	24.82	25.22	25.36	<23.33	25.67	26.05	26.53
3C204	25.38	25.22	25.01	25.33	<23.42	26.00	25.83	26.52
3C208	25.65	25.50	25.56	25.76	<24.85	25.65	26.51	26.68
3C215	24.40	24.30	24.70	24.75	23.90	24.17	24.67	25.87
3C249.1	24.81	24.66	24.74	24.89	23.03	24.99	25.33	25.69
3C263	25.73	25.69	25.10	25.30	<23.50	26.43	25.03	26.34
3C334	25.47	25.40	25.25	25.37	24.05	24.87	24.09	26.25
3C336	25.12	25.00	25.80	25.84	24.50	26.02	26.45	26.68
3C351	23.91	23.82	24.33	24.37	22.44	25.51	23.99	26.20
3C432	25.17	25.04	25.21	25.36	<23.64	26.67	25.41	27.13

Notes to TABLE 18:

(a) Parameter codes signify the following:

(i) Feature identification

cf = central feature, j = jet, cj = counterjet,
jh = jet hot spot, cjh = counterjet hot spot,
x = extended lobe emission.

(ii) Intermediate-scale flux density assignment

A = assigned to central feature (as in Tables 5 and 6),
B = assigned to jet (as in Table 17).

(b) Spectral indices assumed for corrections to rest frame:

(i) central features, 0.0
(ii) jets and counterjets, 0.6
(iii) hot spots, 0.8
(iv) extended lobe emission, 1.0.

These results do not depend heavily on whether the intermediate-scale emission is assigned to the central feature or to the jet, but the correlation is indeed tightest when only the milliarcsecond-scale flux density is used for the central feature, and the intermediate-scale flux density is assigned to the jet, as shown in Fig. 45. For example, assigning the intermediate-scale flux density to the central feature reduces the linear correlation coefficient in Fig. 45(a) to $r=0.76$, and in Fig. 45(b) to $r=0.57$. To simplify what follows, we henceforth emphasize results with the intermediate-scale flux density assigned to the jet.

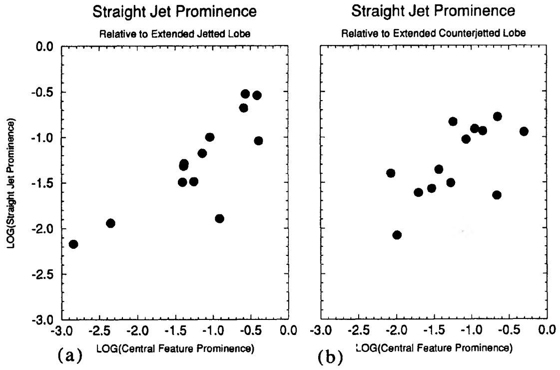

FIG. 45. The prominence of the straight segment of the jets plotted against the prominence of the central features. The left panel (a) shows the strong ($r=0.83$) correlation when both prominence measures are normalized by the extended flux density of the jetted lobe. The right panel (b) shows the weaker ($r=0.65$) correlation when both are normalized by the extended flux density of the counterjetted lobe.

The central feature and jet prominence data will exhibit some "false correlation" because both quantities are normalized by the same extended flux density and the range of normalizing flux densities is similar to the range of the numerators. This and our use of logarithmic quantities imply that the significance of these correlations cannot be inferred from the normal distribution. We therefore ran 90 000 trials wherein the central feature and jet flux densities in 13-source samples were fully randomized up to their observed maxima and were normalized by extended lobe flux densities randomized within the observed range. We then computed correlation coefficients for the 90 000 sets of random log-prominence data. The false correlation coefficient was below $r=0.83$ in 98% of the trials. This should underestimate the significance level of the true correlation, because the observed extended emission flux densities are less evenly distributed between their minima and maxima than those in the random trials. We infer that there is a better than 98% probability that the 13 quasars exhibit a real correlation between central feature prominence and straight jet prominence.

This conclusion is supported by four other lines of argument. First, all other apparent prominence–prominence correlations in this sample were significantly weaker. Second, direct correlation of the central feature and straight jet flux densities, without normalization to prominences, yields a correlation coefficient of $r=0.63$, which is also significant at the 98% level under the normal statistical assumptions. Third, all other direct correlations between the flux densities of the central features, jets, counterjets, hot spots, and lobes in this sample are significantly weaker than that between the central feature and the straight jet. Fourth, we estimated the slope of the relationship and its error using method (b) of York (1966) to allow for the presence of errors in both sets of prominence data, using the observed mean error ratio of 1.7:1 between the jet and central feature prominences. The result, 0.63 ± 0.12, is significantly below the unit slope that would be expected if the relationship was an artifact produced entirely by the normalization.

Our results therefore suggest that the prominence of the milliarcsecond-scale features and of the *straighter* large-scale jet emission are physically related. There is no separation of points in this correlation by the fraction of the total jet that is included in the straight segment, or by the projected length (in kiloparsecs) of the straight segment. There is also no correlation ($r=0.20$) between jet prominence and central feature prominence (normalized by the extended flux density of the jetted lobe) if we use the integrated flux density of the jet, or ($r=0.06$) that of its "bent" portion alone (the integrated jet less the straight segment). Note, however, that some of these jet flux densities are subject to large uncertainties from complicated background subtractions, and these uncertainties could degrade the correlation.

Pure relativistic beaming models for the jet/counterjet asymmetries predict that the prominence of the counterjets should *anti*correlate with that of the jets and of the central features. Our data show no sign of such anticorrelations.

Figure 46(a) shows that the prominence of the counterjet candidates is uncorrelated with that of the *straight* jet segments, normalizing both by the flux density of the total extended emission. To account for the upper limits in the counterjet candidate prominences, we estimate the correlation coefficients that involve them using the Spearman method in the ASURV survival analysis package (Isobe *et al.* 1986; LaValley *et al.* 1992). This analysis gives $r=0.01$ for the data shown in Fig. 46(a). Furthermore, if there is any relationship between the prominence of the counterjet candidates and that of the *bent* jet segments [Fig. 46(b)], it is a weak *positive* correlation with $r=0.62$ from the Spearman method (in 3C 9, 3C 68.1, 3C 215, and 3C 336, both the counterjet candidate and the bent jet segment are prominent, but in 3C 175, 3C 204, 3C 351, and 3C 432 both are relatively inconspicuous). These results are not materially changed if each jet's prominence is normalized by its own lobe's extended flux density, rather than by the common total, as above.

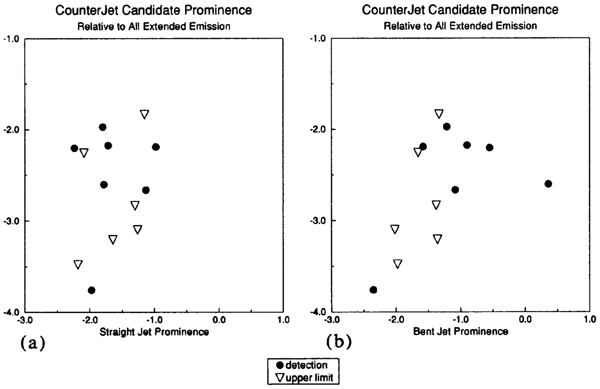

FIG. 46. The prominence of the counterjet candidates plotted against the prominence of the straight jet segments (a—left panel) and the bent jet segments (b—right panel). In both diagrams, the prominence measures are normalized by the total extended flux density of both lobes and the triangles are upper limits.

The counterjet candidate and central feature prominences are also uncorrelated ($r=-0.01$ from the Spearman analysis in ASURV).

The interpretation of these results is complicated by the tendency to false positive correlation in prominence–prominence data, but our data contain no direct evidence *for* the hypothesis that counterjet candidate prominence is dominated by Doppler boosting/hiding.

5.5.3 Prominence of features and jet bending

We now examine correlations between the prominence of radio features and the six measures of apparent jet deflection presented in Table 7.

The strongest such relationships in our sample are anticorrelations between the prominence of the jetted hot spot and the centrally referenced measures of jet deflection (Fig. 47). The extremes are represented by 3C 9, 3C 215, and 3C 334 (bent jets with weak terminal hot spots), and 3C 263 (straight jet and a prominent hot spot), but the trend involves the entire sample, not just these outliers. The anticorrelation is significant at the 1% level or better ($|r|>0.68$ for a 13-source sample) for all three centrally referenced deflection angles [$r(\eta_{1c})=-0.68$, $r(\eta_{2c})=-0.77$, $r(\eta_{3c})=-0.83$]. The formal correlation coefficients are much smaller for the corresponding locally referenced deflection angles [$r(\eta_{1l})=-0.37$, $r(\eta_{2l})=-0.28$, $r(\eta_{3l})=-0.07$] but are markedly diminished by 3C 68.1, whose largest local deflection occurs in the complex region near the hot spot and is therefore sensitive to interpretation.

We conclude that the prominence of the jetted hot spots generally decreases with the bending of the jet, particularly as referenced to the central feature, and particularly when a large deflection occurs abruptly (thus producing a large value of η_{3c}).

There is also evidence for a relationship (Table 21) between jet bending and counterjet *hot spot* detection. The eight quasars with detected counterjet hot spots have jets that bend less than those in the five whose counterjet hot spot candidates fail to meet our criteria. Once again, the centrally referenced deflection angles display this relationship better than the locally referenced ones.

The strengths of these anticorrelations for the hot spot prominence contrast with the situation for the prominence of the central features and of the straight jet segments. The central feature prominence is completely uncorrelated with the centrally referenced bend angles and shows only a weak dependence on the locally referenced measures η_{2l} and η_{3l}.

The prominence of the straight jet emission is uncorrelated with any of the deflection measures.

The prominence of the integrated jet emission correlates weakly with the centrally referenced deflection measures ($r=0.51$ for the best case—η_{1c}) and slightly better with the locally referenced measures ($r=0.68$ for the best case—η_{1l}). As the straight jet segments show no sign of such a correlation, we might infer that this weak relationship, if any, is contributed by the bent jet segments. This cannot be shown directly from this sample, however. The prominence of the bent jet segments correlates weakly with the centrally referenced deflection measures ($r=0.47$ for the best case—η_{1c}) and slightly better with the locally referenced measures ($r=0.58$ for the best case—η_{1l}), both formally weaker than the trends for the whole jets. This apparent inconsistency probably stems from the small sample size, which makes significance estimates unstable to discrepant data from individual sources. Unlike the anticorrelation for the hot spot prominence, which involves the whole sample, the weak positive correlation of jet prominence with the locally referenced bend angles arises primarily from two sources—3C 9 and 3C 68.1.

The dependence of the counterjet prominence on jet deflection is still harder to assess as we have only high upper limits to the prominence for both 3C 47 and 3C 208. There appears to be only a weak dependence of counterjet candidate prominence (as opposed to detection) on jet bending, itself heavily influenced by the favorable data for 3C 68.1 and 3C 215. Improved upper limits for the sources without counterjet candidates, especially 3C 47 and 3C 208, could strengthen the evidence for such dependence.

To summarize, the evidence for relationships between feature prominence and jet bending is stronger for the features farther from the quasar nuclei. The inner, straight jet segments exhibit no hints of such relationships. For the outer jets and counterjets, the putative relationships are positive correlations, as yet poorly established. For the hot spots, they are negative correlations, much better established.

5.5.4 Prominence correlations that are absent

We looked for correlations of central feature, straight jet, bent jet, integrated jet, counterjet, and both jetted and counterjetted hot spot prominence with several physical parameters (Table 20). In all cases involving ratios of jet-to-counterjet side parameters, we evaluated correlation coefficients for the logarithms of the quantities. No significant correlations (at the 0.5% level or better—$|r|>0.73$ for a 13-source sample) were found with (1) largest projected linear size, (2) lobe flux density ratio (with or without the hot spots), (3) jet spreading rate, (4) jetted hot spot collimation, (5) hot spot flux density ratio, (6) hot spot compactness ratio, (7) hot spot surface brightness ratio, (8) arm length ratio (the ratio of the length of the jetted side to the counterjetted side, using either the angular distance from the central feature to

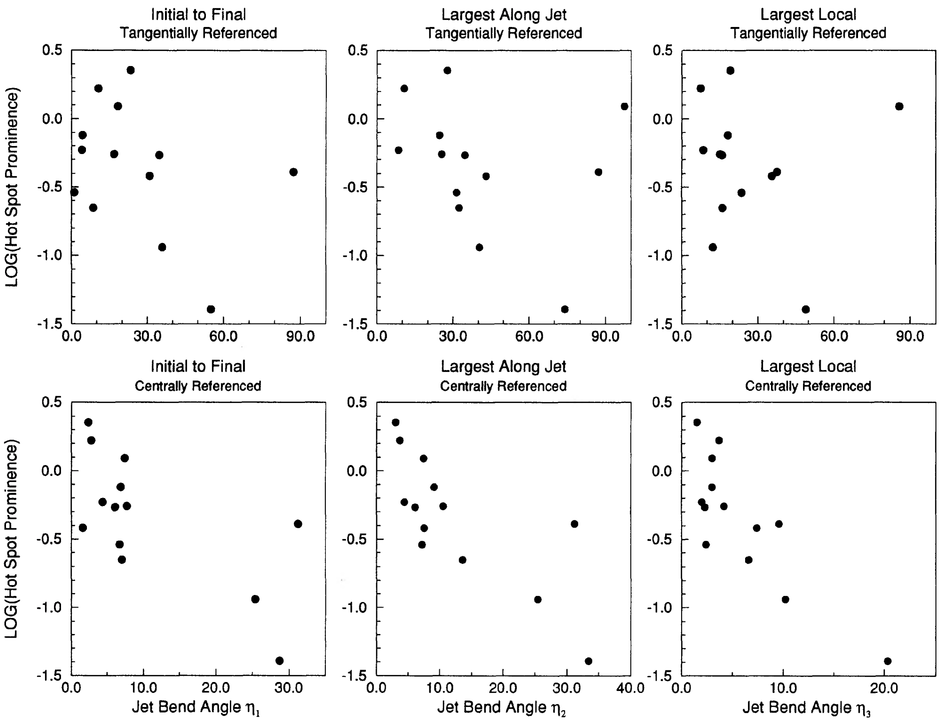

FIG. 47. The relationships between hot spot prominence measures, and six measures of jet bending, showing the tendency for hot spots to be less prominent when the jets are more bent. The upper row plots the prominence against measures of jet bending based on changes in the angles of the tangents to polynomials fitted to the jet paths: the change from the initial to the final segments of the jet, the largest difference in angle between any two tangents along the jet, and the largest difference in angle between tangents at adjacent jet knots. The lower row plots the prominence against similar bending measures referred to the central radio features instead of the local tangents. Note that the angular scales on the deflection axes are not all the same.

TABLE 19. Prominence parameters of radio features.

Logarithmic Prominence Ratios at 5 GHz emitted, F

Source	Fcf,A,jx	Fcf,B,jx	Fcf,A,cjx	Fcf,B,cjx	Fjst,A,jx	Fjst,B,jx
3C 9	-1.263	-1.385	-1.586	-1.708	-1.594	-1.289
3C 47	-0.912	-0.912	-0.660	-0.660	-1.894	-1.894
3C 68.1	-2.706	-2.845	-1.940	-2.078	-2.218	-2.169
3C175	-1.169	-1.389	-1.209	-1.431	-2.010	-1.318
3C204	-0.884	-1.040	-0.797	-0.953	-1.412	-0.999
3C208	-0.411	-0.566	-0.911	-1.066	-0.938	-0.526
3C215	-1.160	-1.257	-1.180	-1.278	-1.822	-1.485
3C249.1	-0.437	-0.588	-0.691	-0.844	-1.123	-0.680
3C263	-0.345	-0.391	-0.251	-0.298	-1.536	-1.045
3C334	-0.342	-0.409	-0.583	-0.649	-0.687	-0.540
3C336	-1.017	-1.141	-1.405	-1.530	-1.564	-1.177
3C351	-2.251	-2.348	-1.144	-1.241	-2.008	-1.940
3C432	-1.280	-1.407	-1.865	-1.992	-2.215	-1.494

Source	Fjst,A,cjx	Fjst,B,cjx	Fjst,A,x	Fjst,B,x	Fjbt,jx	Fjbt,x
3C 9	-1.917	-1.607	-2.086	-1.776	0.853	0.361
3C 47	-1.643	-1.642	-2.087	-2.087	-1.462	-1.655
3C 68.1	-1.446	-1.410	-2.285	-2.245	-0.481	-0.549
3C175	-2.052	-1.360	-2.333	-1.641	-1.036	-1.358
3C204	-1.324	-0.911	-1.670	-1.257	-1.758	-2.017
3C208	-1.437	-1.026	-1.556	-1.145	-0.712	-1.331
3C215	-1.842	-1.513	-2.134	-1.804	-0.902	-1.213
3C249.1	-1.379	-0.944	-1.571	-1.136	-0.630	-1.078
3C263	-1.442	-0.952	-1.792	-1.302	-1.121	-1.378
3C334	-0.927	-0.780	-1.125	-0.978	-1.142	-1.580
3C336	-1.953	-1.589	-2.102	-1.738	-0.362	-0.899
3C351	-0.902	-0.845	-2.041	-1.985	-2.319	-2.351
3C432	-2.800	-2.100	-2.900	-2.201	-1.292	-1.978

Source	Fj,A,jx	Fj,B,jx	Fcj,x	Fcj,cjx	Fjh,jx	Fcjh,cjx
3C 9	0.854	0.856	-2.601	-2.433	-0.388	-0.218
3C 47	-1.325	-1.325	<-2.257	<-1.812	-0.228	-0.186
3C 68.1	-0.473	-0.472	-2.204	-1.365	0.091	-1.263
3C175	-0.993	-0.854	<-3.207	<-2.927	-0.539	-0.201
3C204	-1.250	-0.929	<-3.100	<-2.753	-0.266	-0.342
3C208	-0.509	-0.308	<-1.836	<-1.717	-0.417	-0.052
3C215	-0.854	-0.801	-1.972	-1.681	-1.392	-0.905
3C249.1	-0.510	-0.353	-2.664	-2.473	-0.258	-0.176
3C263	-0.979	-0.777	<-2.835	<-2.485	0.355	-0.955
3C334	-0.557	-0.441	-2.192	-1.995	-0.940	-1.958
3C336	-0.336	-0.300	-2.174	-2.025	-0.120	-0.082
3C351	-1.836	-1.788	-3.759	-2.619	-0.651	-1.073
3C432	-1.243	-1.080	<-3.479	<-3.379	0.224	-1.624

Notes to TABLE 19

(a) Parameter codes signify the following:

(i) Feature identification
cf=central feature, j=jet, jst=straight jet, jbt=bent jet,
cj=counterjet, jh=jet hot spot, cjh=counterjet hot spot.

(ii) Intermediate-scale flux density assignment.
A=assigned to central feature (as in Tables 5 and 6),
B=assigned to jet (as in Table 17).

(iii) Extended emission used for normalization
jx=jet lobe, cjx=counterjet lobe, x=sum of both lobes.

(b) Spectral indices assumed for corrections to rest frame:

(i) Central features, 0.0
(ii) jets and counterjets, 0.6
(iii) hot spots, 0.8
(iv) extended lobe emission, 1.0.

the hot spot or the largest angular extent on each side), or (9) any of our measures of the difference in inhomogeneity between the jetted and counterjetted lobes.

We find no significant correlations between central feature prominence and (1) the ratio of flux densities of the jet and counterjet candidates for their straight segments ($r=0.52$), or (2) the flux density ratio *per unit length* over their entire paths ($r=0.25$). No correlations are apparent between jetted lobe hot spot prominence and central feature prominence ($r=-0.05$), straight jet prominence ($r=-0.13$), or bent jet prominence ($r=0.08$).

5.6 Other Correlations

We might expect correlations among physical parameters other than the prominence measures, arising from orientation alone, from combined orientation and relativistic beaming, or from (possibly differential) interactions between the beams

TABLE 20. Linear correlation coefficients, *r*, between prominence measures and other physical parameters.

Prominence Measure	η_{1c}	η_{2c}	η_{3c}	η_{1l}	η_{21}	η_{31}	LLS	Spr	Col_{jh}	Q_{lob}
Fcf,B,jx	0.02	0.00	0.03	0.12	-0.48	-0.59	-0.23	-0.56	0.45	-0.66
Fjst,B,jx	0.09	0.10	0.09	0.23	-0.22	-0.38	-0.44	-0.33	0.50	-0.71
Fjbt,jx	0.47	0.41	0.19	0.58	0.57	0.43	-0.53	-0.40	0.55	-0.48
Fj,B,jx	0.51	0.45	0.20	0.68	0.55	0.33	-0.59	-0.37	0.54	-0.55
Fjh,jx	-0.68	-0.77	-0.83	-0.37	-0.28	-0.07	-0.22	-0.21	-0.12	0.21
Fcj,x	0.31	0.31	0.38	0.29	0.38	0.43	-0.05	-0.41	0.47	-0.38
Fcjh,cjx	-0.20	-0.17	-0.22	0.01	-0.10	-0.07	-0.24	-0.45	0.54	-0.41

Prominence Measure	Q_x	Q_{hs}	$Qcom_{hs}$	QTb_{hs}	Qar_{hs}	Qar_x	Sob_{hs}	Str_{hs}	Sob_{no}	Str_{no}
Fcf,B,jx	-0.68	-0.50	0.53	-0.59	-0.22	-0.01	-0.49	-0.55	-0.58	-0.65
Fjst,B,jx	-0.69	-0.52	0.64	-0.70	-0.31	0.04	-0.56	-0.67	-0.53	-0.69
Fjbt,jx	-0.48	-0.41	0.01	-0.46	0.17	0.18	-0.34	-0.22	-0.51	-0.16
Fj,B,jx	-0.54	-0.44	0.20	-0.58	0.09	0.14	-0.43	-0.35	-0.55	-0.30
Fjh,jx	-0.04	0.42	0.24	0.18	0.26	-0.36	0.28	0.32	-0.07	0.10
Fcj,x	-0.30	-0.40	-0.20	-0.27	-0.33	-0.11	-0.29	-0.05	-0.29	-0.16
Fcjh,cjx	-0.20	-0.73	-0.02	-0.56	0.03	0.30	-0.43	-0.24	-0.23	0.11

F - prominence measure for

cf : central feature
jst : straight jet segment
jbt : bent jet segment
j : total jet
jh : jetted hot spot
cj : counterjet
cjh : counterjetted hot spot
B : all >mas scale cf emission assigned to jet

- normalized by

jx : extended lobe emission on jetted side
cjx : extended lobe emission on counterjetted side

η - deflection measure (Sec 5.2.2)
LLS - largest linear size (h^{-1} kpc)
Spr - mean jet spreading rate
Col - collimation (angle subtended at cf) of hot spot
Q - logarithm of integrated flux density ratio (jet/cj sides)
lob : total lobe emission
x : extended lobe emission
hs : hot spots or candidates
Qcom - logarithm of area ratio for most compact hot spot components
QTb - logarithm of surface brightness ratio for most compact hot spot components
Qar - logarithm of arm length ratio of lobes (jet/cj sides)
x : based on furthest extent
hs : based on hot spots
Sob - Sobel inhomogeneity ratio
Str - Structure function inhomogeneity ratio
hs : hot spots included
no : hot spots excluded

and the surrounding medium. For example, projected linear size might anticorrelate with apparent jet bending angle either purely geometrically (because of differing orientations of the source axes to the lines of sight) or because stronger interactions produce larger beam deflections and smaller source sizes.

We looked for correlations among the following parameters and found none that is significant at the 0.5% level or better ($|r|>0.73$ for a 13-source sample): (1) apparent jet deflection angle, (2) largest projected linear size, (3) lobe flux density ratio, (4) jet spreading rate, (5) jetted hot spot collimation, (6) hot spot flux density ratio, (7) hot spot compactness ratio, (8) hot spot surface brightness ratio, (9) arm length ratio, and (10) the lobe inhomogeneity measures. Table 22 lists the results only for the strongest correlation found between any two parameter types.

Excluding the (likely trivial) correlations between parameters that both involve the intensities of the hot spots (e.g., the total lobe intensity ratio versus the hot spot brightness ratio), Table 22 suggests only three correlations significant at the 0.5% level or better that are not mentioned above. (1) Larger extended flux density ratios between the lobes are correlated with larger inhomogeneity differences between them (e.g., Qx vs the Sobel measure with hot spots removed has $r=0.91$); (2) hot spot surface brightness ratio correlates with lobe inhomogeneity (e.g., QTbhs vs the Sobel measure with hot spots removed has $r=0.79$); and (3) extended flux density ratio correlates with hot spot brightness ratio ($r=0.77$). All three correlations are strongly influenced by two sources, 3C 68.1 and 3C 351, whose lobe flux densities and hot spot surface brightnesses are exceptionally asymmetric. They do not appear to be properties extending through the rest of our sample. They suggest, however, that in the most extreme cases some "extra" power in the brighter lobe is concentrated into ridges and filaments rather than in a broad emission plateau. Note that in both sources that contribute strongly to this trend, the "extra" power is in the jetted lobe, though the inner parts of the jets, and the central features, are notably inconspicuous.

6. DISCUSSION

6.1 Counterjet Detection

As detailed in Secs. *4.4* and *5.2.1*, we detect no *unambiguous* counterjets in any source. We do, however, find counterjet *candidates* in seven. The properties of the counterjet candidates correlate with several other attributes of the sample. Section *5.2.2* showed that the detectability of these candidates is increased by jet bending. This connection is reinforced by more detailed morphological evidence. Most

TABLE 21. Mean jet deflection angles and counterjet hot spot detection.

		Referred to Central Feature			Referred to Polynomial Tangent		
Mean of	Was A CounterJet Hot Spot Detected?	η_{1c} (°)	η_{2c} (°)	η_{3c} (°)	η_{11} (°)	η_{21} (°)	η_{31} (°)
8	Yes	8.2	9.8	4.3	26.2	35.6	21.5
5	No	14.6	16.8	8.4	24.5	50.6	34.2

(but not all) of the counterjet candidate emission is opposite parts of the main jets that are strongly curved, or rapidly changing in brightness, or both. Counterjet candidates are especially hard to find opposite long ($>15h^{-1}$ kpc), straight segments of the jets (3C 47, 3C 175, 3C 204, 3C 263, 3C 334, 3C 336). In 3C 215, 3C 334, and 3C 336, the counterjet candidate is brighter in the outer part of the source, beyond the distance at which the main jet shows a large local deflection. (In all three sources, the main jet also brightens in a region roughly opposite the counterjet candidate.) Many of the better counterjet candidates are also in sources whose lobes are significantly displaced to *opposite sides* of the jet–counterjet axis (S symmetry) and whose hot spots are misaligned (Sec. *5.4*).

The counterjet candidates are therefore most conspicuous in parts of sources where the beams appear to change direction. The beams may appear to deflect either because they interact strongly with their environment or because the orientation of the central engine has changed over time. In either case, *flow velocities are unlikely to be constant in either magnitude or direction where most jet/counterjet intensity ratios can be measured from our data.* If kiloparsec-scale flow velocities are often relativistic in Fanaroff–Riley Type II sources, counterjets may be detectable only after unfavorable beaming factors are removed on the receding side by perturbing the flows. This clearly complicates, and may prevent, the use of global jet/counterjet intensity ratios for tests of "unified schemes" that assume unique values of the Lorentz factor in each beam.

6.2 Jet/Counterjet Ratios

As discussed in Sec. *5.2.1*, estimates of integrated counterjet powers are complicated by problems both of counterjet recognition (e.g., confusion by filaments in the lobes) and of correcting faint features for a spatially variable lobe background. Jet/counterjet ratio measurement is even harder, *because the counterjet candidates are not faint replicas of the main jets.* We therefore face the extra ambiguity of deciding which segments of the jets and counterjets to compare when deriving the ratio.

The ratio of peak intensities is easily found but is probably not useful: knot-to-knot brightness differences may tell us more about local disturbances in the flows than about global parameters.

The integrated flux density ratios (or limits to them) are hard to assess if no counterjet is detected. If the jet is curved, the trajectory of the invisible counterjet is less certain, and we must resort to (poorly justified) assumptions of morphological symmetry when deciding which regions to compare. Even if the jet is relatively straight, the analysis is still complicated if the jet does not fill the path from the central feature to the hot spot. If the flow and pattern speeds in the jets can be comparable to the velocity of light, the appropriate exponent of the Doppler factor in the flux boosting expression for randomized magnetic fields and particle motions may differ from the value of $2+\alpha_j$ (where α_j is the jet spectral index, defined via $S\propto\nu^{-\alpha}$) that is appropriate for a smooth jet that ends at a hot spot. Consider, for example, the "born-again" relativistic jet (Bridle *et al.* 1986, 1989; Clarke *et al.* 1992). If a single, isolated piece of jet is present on both sides, an exponent of $3+\alpha_j$ is appropriate, but if multiple jet segments are present, the appropriate value of the exponent becomes unclear. Note also that exponents outside the range from $2+\alpha_j$ to $3+\alpha_j$ may be appropriate if the jets and counterjets contain well ordered magnetic fields (Begelman 1993).

We integrate both the jet and counterjet sides over the entire distance from central feature to hot spot in Table 6(a), and over a region with the same extent as the straight jet segment in Table 6(b). The uncertainties outlined above mean that the jet/counterjet ratios from Table 6 should be interpreted cautiously, even in the simplest of beaming models. The appropriate exponent in the flux boosting expression depends not only on the morphologies of the jet and counterjet, *but also on the source model and history used to explain them.*

The absolute powers of the counterjet candidates in these Fanaroff–Riley Type II sources are similar to, or even exceed, the jet and lobe powers of most Fanaroff–Riley Type I (plume-like) sources (except in the most optically luminous

TABLE 22. Linear correlation coefficients, r, for correlation tests among various physical parameters.

Parameter Pair	r	Parameter Pair	r	Parameter Pair	r
η11, LLS	-0.40	Qx, Spr	0.62	Coljh, Qcomhs	-0.05
η31, Qx	0.32	Qlob, Coljh	-0.75	Coljh, QTbhs	-0.55
η3c, Spr	0.15	Qlob, Qhs	0.84	Coljh, Qarhs	-0.30
η3c, Coljh	0.30	Qx, Qhs	0.61	Coljh, Sobno	-0.49
η3c, Qhs	-0.32	Qx, Qcomhs	-0.56	Qhs, Qcomhs	-0.16
η31, Qcomhs	-0.44	Qlob, QTbhs	0.89	Qhs, QTbhs	0.84
η11, QTbhs	-0.36	Qx, QTbhs	0.77	Qhs, Qarx	-0.51
η3c, Qarhs	-0.27	Qlob, Qarx	-0.44	Qhs, Sobhs	0.80
η11, Sobno	-0.35	Qlob, Sobhs	0.86	Qhs, Sobno	0.58
LLS, Qx	0.74	Qx, Sobno	0.91	Qcomhs, QTbhs	-0.63
LLS, Spr	0.21	Spr, Coljh	-0.42	Qcomhs, Qarhs	0.30
LLS, Coljh	-0.67	Spr, Qhs	0.51	Qcomhs, Strno	-0.66
LLS, Qhs	0.43	Spr, Qcomhs	-0.23	QTbhs, Qarx	-0.38
LLS, Qcomhs	-0.43	Spr, QTbhs	0.54	QTbhs, Sobhs	0.94
LLS, QTbhs	0.59	Spr, Qarx	-0.15	QTbhs, Sobno	0.79
LLS, Qarx	-0.27	Spr, Sobno	0.70	Qarx, Strhs	-0.55
LLS, Sobno	0.67	Coljh, Qhs	- .76		

galaxies, plume-like structure is uncommon in sources with 5 GHz total powers above $P^5_{\rm tot}=10^{24.5}\,h^{-2}$ W Hz^{-1}, e.g., Owen 1993). If these counterjet candidates are indeed the brightest parts of counterjets (i.e., they are not merely confusing lobe features), this rules out any possibility that the main jets in these sources are Doppler-boosted beams with low intrinsic radio powers (similar to those in Type I sources). In this sense, our observed counterjet powers add to the evidence that the beams that form edge-brightened lobes containing hot spots are *intrinsically* more radio-luminous than those that form plumes.

It will be difficult for VLA data to refine the intensity ratio measurements given in Table 6, even with longer observations. High sensitivity and dynamic range will be frustrated by confusion with lobe fine structure, and by problems of counterjet recognition similar to those described here. VLA full-synthesis observations at 8.4 GHz may, however, enjoy a slight advantage over our data if the spectra of the jets are flatter than those of confusing fine structure.

6.3 Jet Properties

The detailed evolution of the spreading rates (Sec. *5.2.4*) suggests that, in several of these quasars as in many powerful radio galaxies, the jets initially expand rapidly and then recollimate. The strong tendency for the closest knot to the central feature also to be the brightest (until the region near the terminal hot spot—Sec. *5.2.5*) suggests that we detect jets on these scales in, or shortly after, a regime of strong interactions with the ambient medium, i.e., that jet brightening and recollimation are closely connected. This is consistent with models of jet propagation in which strong shocks are driven into the jets as they are recollimated.

Most jet knots align well with the jet direction (Sec. *5.2.3*), and the magnetic field tends to be parallel to the jet in these knots (Sec. *5.2.7*). The most extreme knot and field misalignments tend to occur at the most severe bends in the jets, which are often just prior to the hot spot and at places where the jet brightens substantially. These extreme cases may also be governed by interactions with the surrounding medium.

We therefore have several lines of evidence, from the jets themselves, that their properties are modified significantly as they travel outwards.

In contrast, Sec. *5.5.2* showed a link between the prominence of the inner, straight segments of the jets and that of the smallest-scale emission—the central milliarcsecond-scale features. Two aspects of the jet prominence data reinforce the idea that ongoing interactions modify the initial (parsec-scale) properties of the jets as they propagate to many-kiloparsec scales. First, the slope of the relation between straight jet and central feature prominence, 0.63 ± 0.12, is significantly less than that of 1.3 expected in *constant-velocity* relativistic-jet models (implying some deceleration, see Sec. *7.1*). Second, the prominence relationship is absent for the bent jet segments (though it could be diminished there by observational uncertainties alone).

Section *5.5.3* also showed how apparent jet bending interacts with jet prominence. The prominence of the inner, straight jet segments is uncorrelated with jet bending. But bending weakly affects the prominence of the outer, more bent, jet segments, and clearly interacts with our ability to find counterjet candidates (the brightest of which are in the outer parts of the sources, beyond major bends in the beam paths). The prominence of these counterjet candidates is uncorrelated with that of the central features or straight jets, but may be weakly correlated with that of the bent jet segments (Sec. *5.5.2*).

The jet prominence data thus reinforce the evidence from the jets' intrinsic properties that jet parameters change with distance from the central object via interactions with the surrounding medium, and that these interactions help to determine counterjet prominence.

6.4 Hot Spots

Our new images link the properties of jets and of hot spots in several distinct, and at first sight contradictory, ways.

There are systematic differences in compactness and in placement between the hot spots in the jetted and counterjetted lobes (Sec. *5.3*). The only lobes that lack hot spots by our new definition are on the counterjetted side. More generally, whenever there is a >25% difference in compactness between the hot spots or hot spot candidates, the jetted hot spot is always more compact than the counterjetted. Jetted hot spots are also more likely to be deeply recessed from the lobe edges. Section *5.4* showed that the properties of the jetted hot spots account for the most significant differences in inhomogeneity between the jetted and unjetted lobes. The hot spots, but possibly not other structures in the lobes, therefore seem to retain some memory of whatever initiates the jet/counterjet sidedness asymmetry.

Section *5.5.3* showed that the jetted hot spot is less prominent when the jet bends through a greater angle, particularly when the bend in the jet is abrupt. The counterjetted hot spots also tend to be ill defined when the jet is more bent. Both trends imply that bending the jets reduces their ability to form compact structures in the lobes. A second process that is closely connected to jet bending therefore appears to compete with whatever couples hot spot properties to the initial jet/counterjet asymmetries.

Note that we also find that increased jet bending enhances the chance of detecting a counterjet candidate (Sec. *5.2.2*), but decreases the chance that the counterjet feeds a compact hot spot (Sec. *5.5.3*). These relationships are imperfect, but suggest some anticorrelation of jet and hot spot properties on the *counterjetted* side. Counterjetted hot spots are also less well defined in larger sources (Sec. *5.5.3*).

Laing (1989), using data with higher resolution but poorer signal-to-noise ratio than ours, found that 26 of 30 powerful sources (including 9 in common with this study) had the *brighter* hot spot on the same side as a jet or a line of compact knots. He also noted the tendency of bright, compact hot spots to be located away from the extreme ends of their lobes. Comparing our data with Laing's, it is unclear whether surface brightness or compactness correlates better with jet side, but we firmly support his broader conclusion that the properties of hot spots depend on whether they are fed by the jet or the counterjet. Models that attribute differences in jet prominence primarily to differences in relativistic beaming should therefore address whether some properties of the hot spot emission are affected by beaming. Section *7.1* discusses this further.

6.5 Summary of Empirical Results

6.5.1 Detection rates

Jets and central features were detected in all 13 quasars in our augmented sample, whereas counterjet *candidates* were found only in 7 sources. Hot spots meeting our compactness criteria were detected in every jetted lobe, but in only eight of the counterjetted lobes.

6.5.2 Links between the central feature and larger scales

The good correlations between the sidedness of the milliarcsecond-scale extended features and of the large-scale jets, and between the prominence of the central features and of the *inner, straighter* segments of the jets imply that whatever determines the sidedness and prominence of the parsec-scale features also influences the sidedness and prominence of kiloparsec-scale jet emission.

Although the prominence of the bent jet segments is uncorrelated with the central feature prominence, these segments *are* generally brighter than the counterjet candidates at comparable distances from the quasars. Some connection with the initial asymmetry therefore persists beyond the straight jet segments. This conclusion is reinforced by the fact that jetted and counterjetted hot spots show systematic differences in their compactness and their recession into the lobes. Evidently, some of this initial influence persists even to the ends of the jets.

The lack of clear jet-related differences between any properties of the more extended lobe emission suggests that this influence, whatever its nature, does not extend much beyond the hot spots, however.

6.5.3 Evidence that large-scale interactions modify jet properties

In contrast to the above, we found a poor correlation between the prominence of the central features and of the more crooked segments of the jets, a lack of counterjet candidates opposite long straight jet segments, a presence of such candidates when both the jets and the lobes are distorted, a weak correlation between counterjet candidate prominence and the prominence of the outer, more bent jet segments, and anticorrelations between jetted hot spot prominence and counterjet hot spot detection with all three centrally referenced measures of jet bending. These all imply that another phenomenon, closely coupled to jet bending, eventually supplants the initial conditions to determine the prominence of some features far from the central region.

We might therefore expect to find some correlation between prominence and deflection for the bent parts of the jets, on the general grounds that the more severe the perturbation, the more internal energy will ultimately be converted to synchrotron radiation. Table 20 shows that these correlations are weak for our sample as a whole (the highest value of r being 0.58 for η_{1l}). We note, however, that the main bends in eight of the jets occur in their outer parts and the jet brightens substantially near these bends in seven of them (3C 68.1, 3C 175, 3C 204, 3C 208, 3C 263, 3C 334, and 3C 336).

7. CONSEQUENCES FOR MODELS OF RADIO SOURCES

Sections 5 and 6 identified several trends in our data that bring new constraints to the issue of what determines the asymmetries and prominence of jets and hot spots in radio-loud quasars. The most important of these are the results showing that the prominence of the central features, jets, and hot spots relative to the more extended lobe emission are systematically connected to one another and to some attributes of the source morphologies.

We now discuss some consequences of these results for the three specific views of the energy transport process described in Sec. 1.

7.1 Bulk Relativistic Flow

In this model, the observed jet/counterjet asymmetries stem mainly from differential Doppler boosting of emission from intrinsically symmetrical, relativistically moving beams. The bulk velocity of the flow through the emitting region produces the asymmetry between the jets and dominates the apparent prominence of the central features and of some portion, perhaps all, of the length of both jets.

For this model, our most significant results are (a) that the large-scale jets are on the same side of the most compact milliarcsecond-scale radio feature as the more extended small-scale emission in all six cases where this inner sidedness is known, (b) that the prominence of the central features and the prominence of the straight parts of the jets are correlated, and (c) that the slope of the prominence relationship (0.63±0.12) is less than expected if the straight jet segments and the central features contain flows with the same distribution of Lorentz factors and orientations. If the dispersion of *intrinsic* source properties in this sample is not too large, relativistic jet models would require such a correlation, with a slope that depends on the relative Lorentz factors of the flows through the central feature and through the jet. At any given inclination θ to the line of sight, the slope expected from an ensemble of *intrinsically similar* jets and central features with effective spectral indices α_j, α_c, velocities $\beta_j c, \beta_c c$, and Lorentz factors γ_j, γ_c for the logarithmic relationship plotted in Fig. 45 can be shown to be

$$\frac{n+\alpha_j}{n+\alpha_c}\frac{\beta_j}{\beta_c}\left(\frac{1-\beta_c \cos \theta}{1-\beta_j \cos \theta}\right),$$

where n is in the range $2<n<3$ (depending on the geometry of the jet) if the emission is isotropic in the rest frame of the flow.

Consider the case with $n=2$, $\alpha_c=0$, $\alpha_j=0.6$. Then if the Lorentz factor is the same in the milliarcsecond-scale central features and in the large-scale jets, the slope of the log prominence relationship should be 1.3. The lower observed slope of 0.63±0.12 implies that $\gamma_j<\gamma_c$ under a wide range of assumptions *if the observed dispersion in prominence is dominated by the effects of relativistic beaming* rather than by intrinsic differences from source to source. For example, if $\gamma_c=5$ in all the milliarcsecond-scale central features, and if the jets are randomly oriented between about 20° and 70° to the line of sight (a range that is compatible with the observed range of straight jet and central feature prominences), then the observed slope would correspond to $\gamma_j=1.6\pm0.2$ in the large-scale jets. The estimate of γ_j from this argument depends weakly on the assumed range of orientations (e.g., it would be 2.0 ± 0.3 for the range from 10° to 60°), but values $\gamma_j\leqslant2$ result from most models in which extended quasars are $>10°$ from both the line of sight and the plane of the sky.

Our data therefore suggest that the flow in the detected jets decelerates between the parsec and kiloparsec scales, but the small size of our sample makes the result somewhat fragile. Specifically, *the strength of the correlation and the low value of the slope depend strongly on 3C 68.1 and 3C 351.* (Without these two sources, the correlation coefficient decreases from $r=0.83$ to $r=0.67$ and the slope estimate changes from 0.63 ± 0.12 to 0.87 ± 0.29). The result also depends to a lesser extent on the assignment of the intermediate-scale flux density to the jet rather than to the central feature (as discussed in Sec. 5.5.2): assigning the intermediate-scale flux density to the central feature reduces the correlation coefficient to $r=0.76$, but also reduces the estimated slope to 0.52 ± 0.12.

It is also interesting that the correlation shows no sorting of sources by the fraction of the jet that has been classified as straight or by the length of the straight portion (in kiloparsecs). This could mean that there is little change in the velocity field of these jets over their straight segments, no matter how long they are. The lack of correlation between the prominence of the central feature and of the more bent jet segments may indicate, on this model, that beaming into any of a wide range of orientations in the outer, bent portions of these kiloparsec-scale jets decouples their apparent emission from that of the inner, and presumably straighter, parsec-scale jets.

The distribution of "straight segment" jet to counterjet flux density ratios, if interpreted as measurements rather than limits, is also consistent with $\gamma_j\sim2$ if these quasars are randomly oriented between ~20° and ~70° to the line of sight. This would require the sample to be oriented somewhat closer to the sky plane on average than Barthel (1989) proposed for all quasars. The sample may be biased away from the line of sight by our choice of extended lobe-dominated quasars for imaging. Note, however, that if the sources for which we find only lower limits to the jet/counterjet ratios in fact have ratios of order 5 times our limits, the orientation distribution could resemble that proposed by Barthel.

The idea that γ_j decreases to a value $\leqslant2$ on many-kiloparsec scales from a higher value in the central features is not new (e.g., Owen & Puschell 1984; Bridle & Perley 1984). The earlier estimates of γ_j on large scales were, however, based on the rates of jet detection in complete samples of quasars taken to be *randomly* oriented relative to us. Our estimate differs from these in that (a) it refers only to the initial straight jet segments and (b) it does not assume random orientation of the quasar sample. As our jet detection rate of 100% conflicts with the assumptions made in the earlier analyses, our apparent agreement with their results may be coincidental.

The correlations between largest projected linear size and central feature prominence or straight jet prominence, which might be expected on the simplest relativistic-beam models, are either weak or absent (Table 20). Projected linear size may be a particularly poor orientation indicator in this sample, however. As well as having the usual problems posed by a range of intrinsic linear sizes, our sample may avoid the line of sight (as described above) and also the plane of the sky (by excluding radio galaxies). Such an atypically small range of orientations relative to the observer would mean that the absence of size-prominence correlations should not be construed as evidence against the relativistic-beam model.

For sources oriented near the line of sight, the apparent jet bending could be an inclination indicator, because true jet bending can be amplified by projection. For the reasons described above, this sample is unlikely *ab initio* to be one in which large apparent bend angles are a symptom of small inclinations to the line of sight. If they were, then in relativistic-jet models we might expect to find positive correlations between jet bending and the prominence of the central features and straight jets, and an anticorrelation between jet bending and counterjet prominence. These expectations all conflict with our data, but we found several correlations that can be understood if the apparent bend angles measure *intrinsic* jet bending. We therefore see no reason to suppose that apparent jet bending is an inclination indicator in this sample.

The lack of correlation between the prominence of the counterjet candidates and that of the central features or of the straight jet segments shows that, even if Doppler boosting dominates the prominence of the straight jet emission, the prominence of the counterjet candidates is differently determined—either by interactions with the surrounding medium, or by beaming based on different velocity and angular distributions, or both. The *positive* correlation of counterjet detection with jet bending reinforces this result but cannot directly distinguish interaction-induced emissivity enhancements from changes in counterjet beaming produced by combinations of slowing, disordering, or redirecting the counterjet flow. For a relativistic-jet model, the fact that the bent jet segments are generally brighter than counterjet candidates in the outer parts of the same sources implies that some beaming remains at large distances, even if the flows have been disordered and redirected sufficiently to remove the correlation of their prominence with that of the central features.

Like the models described in Sec. *7.2* below, the relativistic-jet model assumes that energy is supplied continuously and equally to both sides of the sources. It is therefore consistent with features on the counterjetted side that require recent energy supply (e.g., hot spots O in 3C 175, L in 3C 204, and J in 3C 208, whose inferred synchrotron lifetimes are shorter than the light travel time to them—Table 13).

To explain the tendency for the more compact hot spot to be on the jetted side, models in which relativistic beaming governs jet prominence must consider the possibility that relativistic effects also modify the appearance of the hot spots (Laing 1989). On this view, Doppler favoritism might be the mechanism by which the hot spots "remember" the small-scale asymmetry. This cannot be achieved within the simplest model of a hot spot as a strong perpendicular shock marking the disruption of an axisymmetric jet (Blandford & Rees 1974). There are good reasons to suppose that the average advance speed of the lobe is $<0.3c$, so if the flow is axisymmetric, then the post-shock flow is inevitably subsonic and beaming effects are minor (Wilson & Scheuer 1983). Laing (1989) pointed out that a nonaxisymmetric flow model (in which the shocks are oblique) is crucially different because it allows the post-shock flow to remain supersonic, and (given high obliquity) possibly relativistic so that beaming can remain significant. The observation that jetted hot spots are set back from the leading edge of the lobe is consistent with this idea, as it allows for the possibility of outflow from the hot spot that still has a significant forward velocity [compare the 3D hydrodynamic simulations by Williams & Gull (1985), Cox *et al.* (1991), and Norman & Balsara (1993)]. In this picture, the jetted hot spots are identified with the flow immediately beyond the shock, but those in the counterjetted lobes are identified with downstream material which has slowed down and/or changed direction. Consequences for particle acceleration mechanisms in relativistic oblique shocks were explored by Begelman & Kirk (1990).

Our discovery of a clear anticorrelation between hot spot prominence and jet *bending* challenges the simplest form of this interpretation, however. It argues for a picture in which bending a jet robs it of its ability to generate prominent hot spots, i.e., in which the history of the jet governs the prominence of the hot spot. How could sources with very bent jets preserve a flow into the hot spot that is fast enough for post-shock Doppler beaming to be significant, even with highly oblique shocks? If the Lorentz factor γ_j in the *straight* part of the jet is indeed only ~2, as suggested by our central feature and jet prominence data, *and the jets are homogeneous*, it is unlikely that post-bend, post-shock Lorentz factors could stay high enough to modify the appearance of the hot spots significantly.

7.1.1 An inhomogeneous relativistic jet

This problem may be soluble if the jets are not homogeneous, but contain material flowing with a range of velocities, e.g., an ultrarelativistic "spine" surrounded by a slower-moving sheath (a sheared boundary layer) as suggested by Laing (1993). If the fraction of the material flowing at velocity v between βc and $(\beta+d\beta)c$ is $f(\beta)\,d\beta$, then our estimate of the characteristic Lorentz factor $\bar{\gamma}_j$ is a weighted average satisfying

$$[\bar{\gamma}_j(1-\bar{\beta}_j\cos\theta_j)]^{-(2+\alpha_j)} = \int_0^1 f(\beta)[\gamma(1-\beta\cos\theta_j)]^{-(2+\alpha_j)}\,d\beta.$$

At angles $\theta_j > 20°$ to the line of sight, we would preferentially see emission from the *slower* parts of the jet. Our estimate of $\bar{\gamma}_j$ from this sample would therefore be biased toward the values in the sheath, where the results of interactions with the surroundings should be most apparent. The connection between the initial sidedness asymmetry of the jets and the hot spot compactness asymmetry would be understandable if interactions increase the fraction of slow-moving material in the jet but allow some of the flow near the center of the jet to remain ultrarelativistic, i.e., if interactions skew $f(\beta)$ while retaining most of its upper range in β. The central part of the decollimating flow through the jetted hot spot, being derived from the spine of the jet, could acquire a favorable beaming factor, producing a bright, compact hot spot. The corresponding parts of the flow on the counterjetted side would, however, have an unfavorable beaming factor and thus be relatively suppressed. The emission from the counterjetted hot spots would therefore be dominated by slower-moving material derived from the flow in the sheath.

One aspect of the hot spot compactness asymmetry may be hard to incorporate in such models, however. Section 5.3 showed that the compactness asymmetry of the hot spots correlates with the apparent power of the central feature, in the sense that the asymmetry is smaller when the central feature is more powerful. If relativistic flow is important at the hot spots, we might instead expect the apparent compactness asymmetry between the hot spots to *increase* when the central feature is more *prominent*. In this sample, not only is the correlation of hot spot asymmetry with central feature prominence weaker than that directly with central feature power, but the sign of the correlation opposes that expected for intrinsically small redirection angles at the hot spots.

We infer that the additional complexity inherent in inhomogeneous-jet models may allow them to accommodate some, but perhaps not all, correlations between distant and small-scale features in our sample. We emphasize that this is not the only reason for considering such models, however. They are more realistic than a model in which $f(\beta)$ is taken to be a δ function at any distance along the jet, because a confined jet that contains knots and bends must develop some dispersion in β, and the lowest values of β would occur in the boundary layer under a wide range of circumstances. A high-resolution search for center-darkening in the inter-knot regions of these jets could test whether they have the proposed spine–sheath structure with higher Lorentz factors in the spine.

7.2 Asymmetric Dissipation

Models of this type can be divided into two main classes: those in which the asymmetries are imposed by large-scale gradients in the environments of the quasars, and those in which the asymmetries originate on parsec scales.

7.2.1 Large-scale environmental asymmetries

Although our data show that jet properties are indeed modified by interactions with the environment as the jets propagate, all models of this class encounter the difficulty that an environmental asymmetry which generates a dissipation asymmetry is unlikely to manifest itself over several orders of magnitude in scale size. Plausible forms of this asymmetry would be, for example, an asymmetric density

1994AJ....108..766B

profile in the galaxy induced by a tidal interaction or an external wind, or an offset between the location of the central engine and the center of mass of the galaxy.

Source models in which jet brightness is governed by dissipation could readily accommodate the weak jet–counterjet prominence correlation. In particular, if jet bending enhances dissipation to synchrotron radiation, then the emission of the bent jet segments and the counterjets might both be governed by dissipation. A large-scale asymmetry in this process could leave a positive correlation between jet and counterjet prominence, and explain the deficit of counterjet candidates opposite long, straight jet segments. Note that two of the counterjet candidates (3C 9, 3C 351) are detected as single knots, both of which are opposite the innermost knots in straight segments of jets with pronounced brightness variations. These could be explained as cases in which both the jet and counterjet are brightened locally by "pressure adjustment" shocks relatively near the quasar. Three candidates (3C 215, 3C 334, and 3C 336) are more distant, bent features opposite the brightest, most severely bent portions of the main jets, consistent with both the jet and the counterjet being brightened by bend-induced dissipation. Only one case, 3C 249.1, produced an inner, elongated counterjet candidate, again opposite a particularly bright segment of the jet. (It would be interesting to determine the curvature of these jet and counterjet segments in 3C 249.1 at higher resolution). Models in which interactions dominate the appearance of all counterjets should therefore explore mechanisms that can account both for weak features in "straight" counterjets and for brighter features in bent counterjets.

Models that ascribe the intensity asymmetry between the kiloparsec-scale jets and counterjets entirely to large-scale environmental asymmetries must, however, be asked to explain why the prominence and sidedness of the parsec-scale central features correlate with those of the straight jet segments. This implies a strong coupling of the mechanisms for the asymmetries on the two scales. Our data support the idea that interactions with the large-scale environment indeed modify jet properties significantly. Models that attempt to ascribe the observed asymmetries entirely to *asymmetries* in these interactions must, however, seek to explain this coupling to parsec scales.

7.2.2 *Asymmetries initiated on parsec scales*

The above objection can be circumvented if the asymmetry begins on parsec scales (e.g., as an asymmetry in the content of relativistic particles and/or magnetic fields in the beams, or of their kinematics) and its effects propagate outwards. It would then not be surprising to find a relationship between the prominence of the inner jet segments and of the central features, though different assumptions about the nature of the asymmetries could predict different forms for the relationship. (If the initial asymmetry was entirely in the density of relativistic particles, an approximate proportionality between central feature and jet prominence might be expected, but an asymmetry in field strength or field configuration would produce a more complicated dependence of prominence on distance down the jet as the fields evolve.)

Dissipative models can clearly accommodate the relationships among jet bending, hot spot prominence, and counterjet detection. Like the relativistic-jet model, asymmetric dissipation allows for hot spots on the counterjetted side whose inferred synchrotron lifetimes are shorter than the light travel time to them (see Table 13). Asymmetrically dissipative jets are also likely to generate dissimilar hot spots, as often observed [though it is not clear why the more dissipative (brighter) jet should preferentially form the more *compact* hot spot]. A model in which asymmetric dissipation is the *only* intrinsic asymmetry may have problems explaining the trend for the jetted hot spot to be more deeply recessed into its lobe.

7.3 *Intrinsic Power Asymmetries/Flip-flop*

This describes the hypothesis that the beam on the jetted side, at the time we observe it, supplies more power to its lobe than is available on the counterjetted side. To accommodate the predominantly double-lobed appearance of the general radio source population (and the detailed symmetry of some individual sources), the ratio of power supplied to the two sides must vary with time, with a long-term average of unity.

This model trivially accounts for the differences between the jetted and counterjetted hot spots. The former are being actively resupplied with particles and compressed by an arriving flow, while the latter are not. Counterjets, being intrinsically less powerful on this model, might be expected to generate less compact hot spots (as we observed in 11 of 13 cases). The need for the "born-again" jet to reexcavate a channel into its lobe can explain why recessed hot spots are more prevalent in the lobe with the brighter jet. A further difference that could be explained by this model is the trend for hot spots that are associated with strong secondary fine structure to be on the jetted side (Lonsdale 1989): the ongoing collimated flows needed to support such "multiple hot spots" would then occur only on the currently active side of the source. (Note that although our sample as a whole does not show significant additional inhomogeneity in the jetted lobe once the compact hot spots are excluded, both sources with strong secondary fine structure—3C 68.1 and 3C 351—have such structure only in the jetted lobe).

The connections between counterjet detection and jet bending, and between the prominence of the straight jets and central features, might be explicable in this model if the power asymmetry between the two sides is connected to the directional stability of jets. A mechanism in which the power asymmetry increased when the jet direction is steady might produce such correlations within a flip-flop model.

We cannot use our data to test whether the lobe powers correlate with the powers of the jets that feed them, as they might in some forms of the flip-flop model. Although the lobe power and the integrated jet powers in this sample are indeed correlated with $r=0.70$, this correlation coefficient would be exceeded 61% of the time because of the common dependence of both powers on the redshift, even if the lobe and jet properties were intrinsically unrelated. The flux density ratios between the jetted and counterjetted lobes and between the jets and the counterjet candidates are free of this bias, however. These ratios would be correlated in some forms of the flip-flop model, but in our sample their logarithms are uncorrelated ($r = -0.20$). If the lobe power is dominated by the time-integrated energy supply in a flip-flop model, this lack of correlation requires that the time scale for variations in the jet/counterjet power ratio is short compared to the lobe generation/decay time scales. (This constraint would also avoid large ratios of arm length between the lobes.)

The flip-flop model conflicts with the presence of bright, compact hot spots with short synchrotron lifetimes in lobes in which we find no counterjet candidates, such as 3C 175O, 3C 204L, and 3C 208J. As described earlier, this result suggests that beams are present on the counterjetted side of these sources. Thus, we cannot be dealing with a flip-flop model in its strictest form, but with a two-beam model with a variable, but finite, power asymmetry.

Several other lines of evidence have recently been developed that make the strict flip-flop interpretation interpretation of one-sided jets unattractive. Optical synchrotron emission on the counterjet side in M87 (Stiavelli *et al.* 1992; Sparks *et al.* 1992), and emission line splitting on the counterjet side in 3C 120 (Axon *et al.* 1989) also provide circumstantial evidence for ongoing flow without detectable counterjets.

8. CONCLUSIONS

8.1 Summary of Consequences for Models

Section 6 summarized the empirical correlations among central feature, jet, counterjet candidate and lobe properties that are provided by our new images. Section 7 showed that, when confronted with these detailed constraints, the *simplest* forms of all three types of model that we introduced in Sec. 1 are inadequate. Where, then, do our results lead models of energy transport in powerful sources?

We find a correlation between the *prominence* of the milliarcsecond-scale central features and of the straight jet segments that reinforces the correlation in *sidedness* between these features. Given the ample evidence for relativistic bulk motion in quasar nuclei, we believe that the most attractive explanation of these correlations is that the flows through the central features and the jets are both relativistic. A strength of the twin-relativistic-beam model is that it offers a single coherent explanation of such trends in kiloparsec-scale jet sidedness and prominence for extended sources as well as of the apparent superluminal motions, rapid variability, and low self-Compton x-ray luminosities of sources with prominent parsec-scale features. The *slope* of the prominence correlation implies a departure from the simplest, constant-velocity form of the model, however: we suggest that the flows in the central features are highly relativistic ($\bar{\gamma}_c \sim 5$) while those in the larger-scale jets are mildly relativistic ($\bar{\gamma}_j \sim 2$).

Although none of the sources displayed an unambiguous, continuous counterjet satisfying all of our criteria for jethood, the counterjet *candidates* found in seven sources exhibited systematic properties connected with jet bending. The prominence of these candidates is not anticorrelated with that of the straight jet segments (as expected from relativistic beaming alone), but instead appears to be enhanced significantly by jet bending. No counterjet candidates were found opposite long, straight segments of jets. Our data also suggest that jets bend more readily further from the quasars, and that this bending, particularly when abrupt, decreases their ability to form compact hot spots. In this sense, a "tired jet" model, in which the *average* jet velocity (and presumably Mach number) decreases on many-kiloparsec scales, is compatible with many of our results, whether or not the large-scale flow has a component with a bulk relativistic velocity.

In the presence of such effects, the twin-relativistic-beam model must be modified to unify our results on the prominence and asymmetries of the hot spots with those on the prominence and sidedness of the kiloparsec-scale jets and of the parsec-scale features. The required modification is physically plausible: allowing velocity structure across the jets at all distances from the nucleus, plus deceleration of their outer layers as they interact with their surroundings. The viability of the modified model depends on whether the velocity structure can evolve appropriately while the jet bends. Unfortunately, the model contains many free parameters, so it is hard to test quantitatively without higher-resolution observations of the internal structures of the jets.

The asymmetric-dissipation and intrinsic-asymmetry models also require parameters that cannot presently be quantified and thus make them hard to test in detail. Nevertheless, some simple forms of these models appear to be ruled out by trends in our data.

The strong correlations between the sidedness and prominence of the jets on parsec and kiloparsec scales rule out models that ascribe asymmetries in the large-scale emission *entirely* to large-scale asymmetries in dissipation. These correlations instead require that any intrinsic asymmetries originate on the smallest scales. Asymmetric dissipation models in their purest form also have difficulties with the jet-related asymmetry in hot spot recession.

The simplest form of intrinsic power asymmetry, the pure flip-flop, cannot be reconciled with our evidence for compact hot spots with short synchrotron lifetimes in counterjetted lobes.

It seems likely that the correct explanation of the relationships shown by our data lies in blends of these models. The degree to which Doppler favoritism influences asymmetries in the sources appears to decrease with distance from the quasar. If asymmetric dissipation is also important, it must originate on small scales near the nucleus and also modify the flow parameters enough to influence the morphology of the lobes as well as their brightness. If the jets have intrinsic asymmetries, their power ratio at any given time is evidently not infinite. Other properties (e.g., their mean velocity and collimation), may also be asymmetric, and thus contribute to the observed correlations of asymmetries among hot spots, counterjet candidates, jets, and central features. To remain viable, all models may therefore need to introduce further free parameters that compromise their ability to make unique predictions. Further work may therefore have to aim more at establishing which broad classes of model can generate the effects that dominate at various distances from the quasar, rather than at testing any simple model's detailed predictions.

8.2 Further Observations and Other Samples

Because our data imply that interactions and bending of the flows influence jet and counterjet visibility, images with enough sensitivity and resolution to dissect out the straightest jet segments will be the best arenas for testing relativistic-jet models of kiloparsec-scale asymmetries. A sample containing many sources with *straight* jets and counterjets could test whether Doppler favoritism dominates the appearance of the inner, straight segments on both sides.

Our data suggest a new way to estimate $\bar{\gamma}_j$ on kiloparsec scales from the relation between straight jet and central feature prominences. If this approach can be used convincingly in larger samples, it will allow new tests of the self-consistency of relativistic-beam models. If Fanaroff–Riley Type II quasars are indeed drawn from the same population as Fanaroff–Riley Type II radio galaxies but are oriented systematically closer to our line of sight (Bridle & Perley 1984; Barthel 1989), then the radio galaxies should have less prominent straight jet segments, and much less prominent central features, than those in this sample. (If the counterjet prominence is determined solely by relativistic beaming, the radio galaxies would also have more prominent counterjets, and thus smaller jet/counterjet ratios, than in Table 6. Note, however, that this test should be confined to the regions opposite the straightest segments of the jets, and may give misleading results if attempted with whole-jet and whole-counterjet data.) It will be important to explore whether the same inferred $\bar{\gamma}_j$ value is consistent with the statistics of all powerful sources that "unified" models seek to relate in this manner, and whether a distribution around this value is consistent with intrinsic jet symmetry in such sources.

Recent results from two other source samples bear on the problems discussed here.

Bridle (1995b) has compiled prominence data for the *detected* jets and central features in a sample of 89 Fanaroff–Riley Type II radio galaxies and quasars with unambiguous double-lobed structures. These data illustrate that many quasar jets are indeed more prominent than any radio galaxy jets at similar lobe powers. For example, 39 sources in this sample have $z<1$ and lobe powers $P^{1.5}_{\rm lobe}>10^{26}h^{-2}$ W Hz^{-1} in their rest frames. The geometric mean of the jet prominence (relative to the total lobe emission at 1.5 GHz and in the rest frame of the source) for the 25 quasars is 4.3 times greater than that for the 14 radio galaxies. For the same two subsamples, the geometric mean of the central feature prominence is 42 times greater in the quasars than in the radio galaxies. These results are *qualitatively* consistent with the idea that relativistic beaming affects the prominence of the kiloparsec-scale jets, but less than it affects that of the central features (e.g., because $\bar{\gamma}_j$ decreases on kiloparsec scales). It is desirable to check them (a) in complete samples, (b) taking account of nondetections of jets, and (c) separating straight and bent segments of the jets.

Fernini *et al.* (1993) used the VLA with sensitivity and resolution comparable to ours in order to image five 3CR radio galaxies similar to these quasars in power and angular size. They detected a jet in only one such galaxy, and found no counterjet candidates. Even allowing for the small sample sizes, their results contrast strongly with our detection of jets in all 13 quasars and of 7 counterjet candidates. It will be important to check whether both these differences in detection rate persist in larger, uniformly observed samples of Fanaroff–Riley Type II radio galaxies and quasars. As it stands, the difference in *jet* detection rate between the samples is consistent with unifying the two source classes using the precepts of the relativistic-beam model. The difference in *counterjet candidate* detection rate between them is not, however. Rather, it may be still further evidence that something other than relativistic beaming helps to determine the prominence of the counterjet candidates.

Most of the data calibration and image processing was done at the NRAO in Charlottesville and at the University of New Mexico. We thank our colleagues at both centers for their forbearance on the many occasions when this work consumed most of the available CPU cycles and disk space on their computers. We are also indebted to the NRAO AIPS group for their software for VLA data reduction and image analysis, and to Harvey Liszt for his interactive DRAWSPEC one-dimensional analysis system. We also thank Richard Barvainis for the use of his VLA C configuration data for 3C 249.1 and 3C 351. Much of the image processing was done while D. H. H. held an NRC-NASA Resident Research Associateship at the Jet Propulsion Laboratory, under contract with the National Aeronautics and Space Administration. D. H. H. thanks the University of Manchester for granting time on their Alliant computer to analyze some of the images, the Max-Planck-Institute für Radioastronomie for travel support to do so, and the Research Corporation for support during part of this work. Radio astronomy at the Haystack Observatory of the Northeast Radio Observatory Corporation (NEROC) is supported by a grant from the NSF. This work was also partially supported by NSF Grants AST-8611511 and AST-9012353 to J. O. B.

We thank Peter Scheuer, John Wardle, John Dreher, and Ian Browne for stimulating discussions, comments, and advice throughout the planning and execution of this project.

REFERENCES

Argue, A. N., & Kenworthy, C. M. 1972, MNRAS, 160, 197

Axon, D. J., Unger, S. W., Pedlar, A., Meurs, E. J. A., Whittle, D. M., & Ward, M. J. 1989, Nature, 341, 631

Baars, J. W. M., Genzel, R., Pauliny-Toth, I. I. K., & Witzel, A. 1977, A&A, 61, 99

Barthel, P. D. 1989, ApJ, 336, 606

Begelman, M. C. 1993, Jets in Extragalactic Radio Sources, edited by H.-J. Röser and K. Meisenheimer (Springer, Berlin), p. 145

Begelman, M. C., & Kirk, J. G. 1990, ApJ, 353, 66

Bentley, M., Haves, P., Spencer, R. E., & Stannard, D. 1975, MNRAS, 173, 93P

Blandford, R. D., & Königl, A. 1979, ApJ, 232, 34

Blandford, R. D., & Rees, M. J. 1974, MNRAS, 169, 395

Boroson, T. A., & Oke, J. B. 1984, ApJ, 281, 535

Bremer, M. N., Crawford, C. S., Fabian, A. C., & Johnstone, R. M. 1992, MNRAS, 254, 614

Bridle, A. H. 1984, AJ, 89, 979

Bridle, A. H. 1986, Can. J. Phys. 64, 353

Bridle, A. H. 1995a, in preparation

Bridle, A. H. 1995b, in preparation

Bridle, A. H., Baum, S. A., Fomalont, E. B., Fanti, R., Parma, P., & Ekers, R. D. 1991, A&A, 245, 371

Bridle, A. H., Fomalont, E. B., Byrd, G. G., & Valtonen, M. J. 1989, AJ, 97, 674

Bridle, A. H., & Perley, R. A. 1984, ARA&A, 22, 319

Bridle, A. H., Perley, R. A., & Henriksen, R. N. 1986, AJ, 92, 534

Browne, I. W. A. 1987, Superluminal Radio Sources, edited by J. A. Zensus and T. J. Pearson (Cambridge University, Cambridge), p. 129

Burch, S. F. 1979, MNRAS, 186, 293

Burns, J. O., Basart, J. P., DeYoung, D. S., & Ghiglia, D. C. 1984, ApJ, 283, 515

Cawthorne, T. V., Scheuer, P. A. G., Morison, I., & Muxlow, T. W. B. 1986, MNRAS, 219, 883

Clark, B. G. 1980, A&A, 89, 377

Clarke, D. A., Bridle, A. H., Burns, J. O., Perley, R. A., & Norman, M. L. 1992, ApJ, 385, 173

Clarke, D. A., Norman, M. L., & Burns, J. O. 1989, ApJ, 342, 700

Clements, E. D. 1983, MNRAS, 203, 861

Condon, J. J. 1984, ApJ, 287, 461

Cornwell, T. J., & Evans, K. F. 1985, A&A, 143, 77

Cox, C. I., Gull, S. F., & Scheuer, P. A. G. 1991, MNRAS, 252, 558

Dreher, J. W., & Feigelson, E. D. 1984, Nature, 308, 43

Fanaroff, B. L., & Riley, J. M. 1974, MNRAS, 167, 31P

Fanti, R., Lari, C., Parma, P., Bridle, A. H., Ekers, R. D., & Fomalont, E. B. 1982, A&A, 110, 169

Feigelson, E. D., Isobe, T., & Kembhavi, A. 1984, AJ, 89, 1464

Fernini, I., Burns, J. O., Bridle, A. H., & Perley, R. A. 1993, AJ, 105, 1690

Fernini, I., Leahy, J. P., Burns, J. O., & Basart, J. P. 1991, ApJ, 381, 63

Gregory, P. C., & Condon, J. J. 1991, ApJS, 75, 1011

Hardee, P. E., & Norman, M. L. 1989, ApJ, 342, 680

Hewitt, A., & Burbidge, G. 1987, ApJS, 63, 1

Hine, R. G., & Scheuer, P. A. G. 1980, MNRAS, 193, 285

Hintzen, P., Romanishin, W., & Valdes, F. 1991, ApJ, 366, 7

Hintzen, P., Ulvestad, J., & Owen, F. 1983, AJ, 88, 709

Hough, D. H. (unpublished)

Hough, D. H. 1986, Ph.D. dissertation, California Institute of Technology

Hough, D. H., Readhead, A. C. S., Wood Jr., D. A., & Feldmeier, J. J. 1992, ApJ, 393, 81

Hough, D. H., Zensus, J. A., Vermeulen, R. C., Readhead, A. C. S., Porcas, R. W., & Rius, A. 1993, Sub-arcsecond Radio Astronomy, edited by R. J. Davis and R. S. Booth (Cambridge University, Cambridge), p. 195

Hough, D. H., Vermeulen, R. C., & Readhead, A. C. S. 19xx, private communication

Icke, V. 1983, ApJ, 265, 648

Isobe, T., Feigelson, E. D., & Nelson, P. I. 1986, ApJ, 306, 490

Jenkins, C. J., Pooley, G. G., & Riley, J. M. 1977, MRAS, 84, 61

Killeen, N. E. B., Bicknell, G. V., & Ekers, R. D. 1986, ApJ, 302, 306

Kronberg, P. P., Clarke, J. N., & van den Bergh, S. 1980, AJ, 85, 973

Kronberg, P. P., Dyer, C. C., Burbidge, E. M., & Junkkarinen, V. T. 1991, ApJ, 367, L1

Laing, R. A. 1981, MNRAS, 195, 261

Laing, R. A. 1989, Hot Spots in Extragalactic Radio Sources, edited by K. Meisenheimer and H.-J. Röser (Springer, Berlin), p. 27

Laing, R. A. 1993, Astrophysical Jets, edited by D. Burgarella, M. Livio, and C. P. O'Dea (Cambridge University, Cambridge), p. 95

Laing, R. A., Riley, J. M., & Longair, M. S. 1983, MNRAS, 204, 151

LaValley, M., Isobe, T., & Feigelson, E. D. 1992, BAAS, 24, 839

Leahy, J. P., & Fernini, I. 1989, VLA Scientific Memorandum No. 161 (NRAO, Socorro)

Leahy, J. P., Muxlow, T. W. B., & Stephens, P. W. 1989, MNRAS, 239, 401

Lonsdale, C. J. 1989, Hot Spots in Extragalactic Radio Sources, edited by K. Meisenheimer and H.-J. Röser (Springer, Berlin), p. 45

Lonsdale, C. J., & Morison, I. 1983, MNRAS, 203, 833

Matthews, A. P., & Scheuer, P. A. G. 1990, MNRAS, 242, 623

Menon, T. K. 1976, ApJ, 204, 717

Miley, G. K., & Hartsuijker, A. P. 1978, A&AS, 34, 129

Morganti, R., Fanti, C., Fanti, R., Parma, P., & de Ruiter, H. R. 1987, A&A, 183, 203

Norman, M. L., & Balsara, D. 1993, Jets in Extragalactic Radio Sources, edited by H.-J. Röser and K. Meisenheimer (Springer, Berlin), p. 229

Owen, F. N. 1993, Jets in Extragalactic Radio Sources, edited by H.-J. Röser and K. Meisenheimer (Springer, Berlin), p. 273

Owen, F. N., Porcas, R. W., & Neff, S. G. 1978, AJ, 83, 1009

Owen, F. N., & Puschell, J. J. 1984, AJ, 89, 932

Pacholczyk, A. G. 1970, Radio Astrophysics (Freeman, San Francisco), p. 171

Perley, R. A. 1989, Hot Spots in Extragalactic Radio Sources, edited by K. Meisenheimer and H.-J. Röser (Springer, Berlin), p. 1

Perley, R. A., Bridle, A. H., & Willis, A. G. 1984, ApJS, 54, 291

Perley, R. A., Bridle, A. H., Willis, A. G., & Fomalont, E. B. 1980, AJ, 85, 499

Pooley, G. G., & Henbest, S. N. 1974, MNRAS, 169, 477

Pratt, W. K. 1978, Digital Image Processing (Wiley, New York), p. 487

Rees, M. J. 1978, MNRAS, 184, 61P

Richstone, D. O., & Oke, J. B. 1977, ApJ, 213, 8

Riley, J. M., & Pooley, G. G. 1975, MRAS, 80, 105

Rudnick, L. 1982, in I.A.U. Symposium 97, Extragalactic Radio Sources, edited by D. S. Heeschen and C. M. Wade (Reidel, Dordrecht), p. 47

Rudnick, L., & Edgar, B. K. 1984, ApJ, 279, 74

Sandage, A. R., & Wyndham, J. D. 1965, ApJ, 141, 328

Sanders, R. H. 1983, ApJ, 266, 73

Scheuer, P. A. G., & Readhead, A. C. S. 1979, Nature 277, 182

Schilizzi, R. T., Kapahi, V. K., & Neff, S. G. 1982, JA&A, 3, 173

Schwab, F. R. 1980, ProcSPIE, 231, 18

Schwab, F. R. 1984, AJ, 89, 1076

Smarr, L. L., Norman, M. L., & Winkler, K.-H. A. 1984, Physica, 12D, 83

Sparks, W. M., Fraix-Burnet, D., Macchetto, F., & Owen, F. N. 1992, Nature, 355, 804

Stiavelli, M., Biretta, J., Moller, P., & Zeilinger, W. W. 1992, Nature, 355, 802

Swarup, G., Saikia, D. J., Beltrametti, M., Sinha, R. P., & Salter, C. J. 1986, MNRAS, 220, 1

Swarup, G., Sinha, R. P., & Hilldrup, K. 1984, MNRAS, 208, 813

Swarup, G., Sinha, R. P., & Saikia, D. J. 1982, MNRAS, 201, 393

Tytler, D., & Fan, X.-M. 1992, ApJS, 79, 1

Vermeulen, R. C., Bernstein, R. A., Hough, D. H., & Readhead, A. C. S. 1993, ApJ, 417, 541

Vinokur, M. 1965, Ann d'Ap, 28, 412

Wardle, J. F. C., & Kronberg, P. P. 1974, ApJ, 249, 255

Wardle, J. F. C., & Potash, R. I. 1982, in IAU Symposium 97, Extragalactic Radio Sources, edited by D. S. Heeschen and C. M. Wade (Reidel, Dordrecht), p. 129

Williams, A. G., & Gull, S. F. 1985, Nature, 313, 34

Willis, A. G., Strom, R. G., Bridle, A. H., & Fomalont, E. B. 1981, A&A, 95, 250

Wilson, M. J., & Scheuer, P. A. G. 1983, MNRAS, 205, 449

Yee, H. K. C., Filippenko, A. V., & Tang, D. 1993, AJ, 105, 7

York, D. 1966, Can. J. Phys., 44, 1079

Zensus, J. A., Hough, D. H., & Porcas, R. W. 1987, Nature, 325, 36